

Numerical Study on Air Movement in Sewer Systems

by

Yu Qian

A thesis submitted in partial fulfillment of the requirements for the degree of

Doctor of Philosophy

in

Water Resources Engineering

Department of Civil and Environmental Engineering

University of Alberta

© Yu Qian, 2018

Abstract

Uncontrolled air movement in sewer systems can lead to odor issues (i.e. H₂S releasing), geysers, flooding, manhole cover blowup and public safety and health concerns, etc. However, the movement of the air flow in sewer systems has not been understood well, especially on the fundamentals of the transportation of air in sanitary systems and the mechanisms of geyser events and its mitigation methods in storm systems. This research is conducted in order to address the sewer odor issues and geyser events in sanitary and storm sewer system. This research is to focus on developing numerical models to predict the pressure distribution and potential odor hotspot in sanitary systems, and to investigate and assess potential geyser mitigation methods in storm sewer systems.

A literature review was comprehensively conducted on the air movement in sewer systems. The knowledge gaps between the current understandings on this topic and practical applications were identified. The gaps are: 1, the drag coefficient between the wastewater and air in sewer pipes were missing; 2, the models and its application on air movement in sewer networks and 3, the generation and mitigation of geysers in storm sewer systems. Experimental and numerical models were then built to study the air movement in a single sewer pipe. In the numerical model, a drag coefficient was proposed to predict the air flow driven by the combined effect of the water drag and the pressure gradient. Both the results show that the existence of a hydraulic jump would substantially increase the air intake if the downstream of the hydraulic jump was open channel flow. The proposed model has been applied to a prototype sewer network in Edmonton, Alberta, Canada. A conceptual mathematical model was proposed to estimate the pressure distribution as well as the air flow rate in the prototype sewer pipe network.

For the geyser events in storm sewer systems, a numerical model was built to study the mechanisms of geyser formation and to assess the potential geyser mitigation methods. The results show that the releasing of the entrapped air pocket can trigger geysers based on different initial flow conditions. All proposed geyser mitigation methods mitigate geyser events in terms of the amount of water flowing out of the manhole. For the implementation of orifice plates on top of the riser, a water-hammer like pressure was observed acting on the orifice plate and its peak pressure can reach up to 7.5 times of the pressure in the pipe. An analytical model by rigid column theory was also built to predict the movement of water slug, the pressure variation, and the water-hammer like pressure when the orifice plate was installed at the top of the riser. The power law relationship between the water-hammer like pressure and the relevant parameters were studied and analyzed.

This thesis extends the knowledge in three aspects: (1) the air movement in a single sewer pipe with high water flow velocity, and with the existence of a hydraulic jump; (2) the air movement in sewer networks with dropshafts and a pump station; and (3) the mechanism, and ways of mitigating geyser event in a storm sewer system.

Preface

This thesis is an original work by Yu Qian. It is presented in a paper format and consists of seven chapters.

Chapter 1 is a general introduction on the background and the objectives of this research.

Chapter 2 is the literature review with special focuses on the fundamentals of the air movement in sewer systems.

Chapter 3 to 6 are the main contents of this thesis.

Chapter 3 was published as: Qian, Y., Zhu, D. Z., Zhang, W., Rajaratnam, N., Edwini-Bonsu, S., and Steffler, P. (2017). “Air Movement Induced by Water Flow with a Hydraulic Jump in Changing Slope Pipes.” *ASCE Journal of Hydraulic Engineering*, 143(4): 10.1061/(ASCE)HY.1943-7900.0001252.

Chapter 4 was published as: Qian, Y., Zhu, D. Z., and Edwini-Bonsu, S. (2018). “Air Flow Modelling in a Prototype Sanitary Sewer System.” *ASCE Journal of Environmental Engineering*, 144(3): 10.1061/(ASCE)EE.1943-7870.0001342.

Chapter 5 is currently being prepared as a journal manuscript.

Chapter 6 is currently being prepared as a journal manuscript.

Chapter 7 is a conclusion chapter. The implications of the results and the suggestions for future research on this topic are discussed.

The author also contributed the following publications:

Guo, S., Qian, Y., Zhu, D. Z., Zhang, W., and Edwini-Bonsu, S. (2018). “Effects of Drop Structures and Pump Station on Sewer Air Pressure and Hydrogen Sulfide: Field Investigation.” *Journal of Environmental Engineering, ASCE*, 144(3): 10.1061/(ASCE)EE.1943-7870.0001336.

Qian, Y., Guo, S., Zhu, D. Z., and Edwini-Bonsu, S. (2017). “Field Monitoring of Sewer Airspace Pressurization due to Dropshafts and a Pump Station.” *Proceedings of 14th IWA/IAHR International Conference on Urban Drainage*, Prague, Czech Republic, 10 – 15 September, 2017.

Qian, Y., Zhu, D. Z., Rajaratnam, N. (2015). “Numerical Study on Air Movement in Steep Sewer Pipes.” *IAHR World Congress Proceedings*, 36th Congress, The Hague, Netherland, 28 June – 3 July, 2015

I was responsible for the experimental design, data collection and analysis as well as the manuscript composition. Dr. W. Zhang, Dr. N. Rajaratnam, and Dr. P. Steffler assisted with the experimental design and contributed to manuscript edits of the chapter 3. Dr. S. Edwini-Bonsu assisted with the experimental design and contributed to manuscript edits of the chapter 3, 4, 5, and 6. Dr. W. Shao, and Dr. F. Zhou assisted in the experimental design of chapter 5. Lujia Liu provided assistance in the laboratory experiment of chapter 6. Dr. D. Zhu was the supervisory author and was directly involved with the concept formation and the manuscript composition.

To:

my wife Dr. Lihui Du

my daughter Claire C. Qian

my father Laodong Qian, and

my mother Juan Han

Thanks for your endless support and encouragement.

Acknowledgements

To begin with, I would like to express my sincere gratitude to my supervisor, Dr. David Z. Zhu, for his guidance, valuable advice, encouragement and inspiring discussions in all these years of my PhD journey. His patient, knowledgeable, and insight guidance brings me to a new level on the understanding of water resources engineering. From him I have learnt what research is and how to think scientifically. I would also like to thank him for providing me opportunities to attend conferences, work as a teaching assistant and a research assistant. I would also like to thank Dr. N. Rajaratnam for his valuable guidance on my research.

I want to secondly acknowledge the China Scholarship Council (CSC) Scholarship and the Alberta Innovation Technology Futures Scholarship for the financial support during my PhD study. The funding from the Department of Civil and Environmental Engineering and from my supervisor Dr. Zhu are also highly appreciated. The research conducted during my PhD study is funded by the City of Edmonton, Epcor, and the Natural Sciences and Engineering Research Council of Canada (NSERC). Their financial supports are sincerely acknowledged.

I would like to specially thank my PhD committee members of my PhD candidacy and final exams: Dr. Stephen Edwini-Bonsu (Epcor), Dr. N. Rajaratnam, Dr. Amy Y. She, Dr. Tong Yu, Dr. Ian Buchanan, Dr. Jose G. Vasconcelos, and Dr. David Z. Zhu. I am also thankful to Dr. Peter Steffler and Dr. Carlos Lange for their supports and advices on my numerical model. I also want to appreciate Dr. Fayi Zhou (Epcor) for his suggestions on the geyser study, and Dr. William W. Zhang for coordinating all the projects between the University of Alberta and Epcor. Thank Perry Fedun for his technical supports in the laboratory setups and the computational system. Thank Dr.

Shuai Guo and all crew members for the fieldworks conducted in 2016. Thank all group members and my friends for being with me during these years. It is very nice to meet you.

Finally, my greatest appreciation goes to my wife Dr. Lihui Du, my father Laodong Qian, my mother Juan Han, and my daughter Claire C. Qian. Their endless and unconditional support and love make all this happens. I cannot make this without them.

Table of Contents

Abstract.....	ii
Preface.....	iv
Acknowledgements	vii
List of Tables	xi
List of Figures.....	xii
1. General Introduction.....	1
1.1. Research background	1
1.2. Thesis outline	3
References	5
2. Literature Review	10
2.1. Introduction	10
2.2. Air movement in single sewer pipes	11
2.3. Air movement in pipe networks	15
2.4. Modeling on extreme flow conditions in sewers	18
2.5. Previous investigations in geysers.....	21
2.6. Knowledge gaps	25
References	27
3. Air Movement Induced by Water Flow with a Hydraulic Jump in Changing Slope Pipes	42
3.1. Introduction	42
3.2. Experimental design.....	44
3.3. Numerical methods	47
3.4. Results and discussions	49
3.5. Conclusions	57
List of symbols	59
References	61
4. Air Flow Modelling in a Prototype Sanitary Sewer System	80
4.1. Introduction	80
4.2. Methodologies	83

4.3. Results and discussions	91
4.4. Conclusions	97
List of symbols	99
References	100
5. Numerical Study on the Mechanism and Mitigation of Storm Geysers	115
5.1. Introduction	115
5.2. Numerical methods	118
5.3. Results and discussions	122
5.4. Geyser mitigation methods.....	132
5.5. Conclusions	139
List of symbols	142
References	143
6. Analytical Model on Geyser Mitigation Using Orifice Plates on Riser Top	164
6.1. Introduction	164
6.2. Methodologies	166
6.3. Results and discussions	172
6.4. Conclusion.....	176
List of symbols	178
References	179
7. General Conclusions and Recommendations.....	193
Bibliography	196

List of Tables

Table 3-1 Summary of experiments. (A: angle $\theta = 30^\circ$; B: $\theta = 10^\circ$)	67
Table 3-2 Numerical experiment list for straight pipe model and results.	68
Table 4-1 Comparison of K values from conventional and simplified method.	105
Table 5-1 List of experiments.	147
Table 5-2 Summary of different geyser mitigation methods based on CFD model.	148
Table 5-3 Summary of the performance of orifice plates based on CFD model.	149
Table 6-1 List of numerical simulation arrangement.	182

List of Figures

Figure 1-1 Photo of the air flowing out of the manhole due to high pressure.	7
Figure 1-2 Conceptual drawing of an idealized sewer system.....	8
Figure 1-3 Images of geysers events happened worldwide. (a) Geysers event at Petro-Canada Station, Edmonton, in 2016 (Youtube, 2018a); (b) Geysers event at Nofrills, Edmonton (Courtesy by Epcor) (c) Geysers event at Minneapolis in 1997 (Wright et al., 2011); (d) Geysers event at Montreal in 2011 (Youtube, 2018b).	9
Figure 2-1 Idealized air velocity contour due to the drag of wastewater. (Pescod and Price, 1982)	35
Figure 2-2 Schematic of the control volume for air flow calculation in a sewer pipe.	36
Figure 2-3 Schematic of the control volume for calculating air movement in a dropshaft. (Ma et al., 2016)	37
Figure 2-4 Schematic of the control volume for air pocket transportation in a pipe. (Li and McCorquodale, 1999)	38
Figure 2-5 Sample pressure head during a series of geysers events. (Wright et al., 2011).....	39
Figure 2-6 Schematic of the mechanism of geysers events. (Wright et al., 2011).....	40
Figure 2-7 Schematic of the control volume on calculating the transient in a rapid filling pipe. (Zhou et al., 2002).....	41
Figure 3-1 Schematic of experimental apparatus showing sloping and horizontal pipes.....	67
Figure 3-2 Geometry and boundary conditions of numerical models. (a): straight pipe model; (b): hydraulic jump model.	68
Figure 3-3 Comparison of simulated air velocity profiles at pipe center plane with Pescod and Price (1982).....	69
Figure 3-4 Plot of the air and water velocity ratio with filling ratio for Exp. C0 and C1.....	70
Figure 3-5 Typical pressure distribution in straight pipe model for $D = 60$ cm, $Q_w = 40$ L/s, $p_{exit} = 0$ Pa, $L = 10$ m.	71
Figure 3-6 Typical velocity contour at pipe location of $x = 5$ m showing reversed air flow at top; $D = 0.60$ m, $Q_w = 20$ L/s, $p_{exit} = 5$ Pa.	72
Figure 3-7 Comparison between measured and simulated water surfaces for $Q_w = 9.88$ L/s, $\theta = 10^\circ$. (a) Photo of water surface in sloping pipe; (b) Measured and simulated water surface.	73

Figure 3-8 Plot of additional momentum source induced by the hydraulic jump. (a) Change of air flow rate with different M_s values for $Q_w = 13.58$ L/s; (b) Different M_s values versus Q_w	74
Figure 3-9 Comparison of measured and simulated air velocity profiles at centre plane. $Q_w = 9.88$ L/s, $\theta = 10^\circ$, water level 20 cm in the downstream pipe, $M_s = 0.0015$ kg m/s ² . (a) 1 m upstream of the pipe joint, (b) 0.5 m upstream of the pipe joint, and (c) 1 m downstream of the pipe joint. ...	76
Figure 3-10 Simulated air pressure distribution for B1. $Q_w = 9.88$ L/s, $\theta = 10^\circ$, $M_s = 0.0015$ kg m/s ²	77
Figure 3-11 Simulated air velocity contour at different locations. (a) 1 m upstream of the pipe joint, (b) 0.5 m upstream of the pipe joint, (c) 1 m downstream of the pipe joint. Looking from downstream. $Q_w = 9.88$ L/s, $\theta = 10^\circ$, $M_s = 0.0015$ kg m/s ²	78
Figure 3-12 Plot of air flow rate in hydraulic jump model. (a) air flow rate versus water flow rate, and (b) ratio of air/water flow rate β versus Froude number at the toe of jump or in supercritical flow (for case B4).	79
Figure 4-1 Schematic drawing of the sewer system. Drawing not to scale.	104
Figure 4-2 Schematic of an idealized lateral connection.	105
Figure 4-3 Plots of leakage coefficient. (a) Pipe numbers with head loss coefficient and the zone of influence; (b) Calculated K with different pipe number and head loss coefficient.	106
Figure 4-4 Measured and estimated pressure at T8 and its lateral connections. (a) Schematic of T8 and its lateral connection; (b) Measured pressure distribution at T8 to T8-L7; (c) Measured and predicted pressure distribution from T8 to T8-L7; (d) Comparison of air flow rate through T8 lateral from measurement and prediction.	108
Figure 4-5 Comparison of simulated data and measured data.	109
Figure 4-6 Plot of measured pressure at fieldwork. (a) Measured pressure between T2 and T5; (b) Measured pressure for T7 and T8.	110
Figure 4-7 Pressure distribution along trunk lines. (a) Pressure distribution when T7 and T8 are pressurized (Case 1); (b) Pressure distribution when T7 and T8 are not pressurized (Case 2). ...	111
Figure 4-8 Estimated air flow rate from measured pressure data in the trunk line.	112
Figure 4-9 Plot of measured and predicted pressure change before and after the drop structure at T1-L1.	113
Figure 4-10 Plot of magnitude of forces in sewer pipes. Data plotted is the pipe between manholes in horizontal axis. (a) Case 1; (b) Case 2.	114

Figure 5-1 Geyser event on 27 th July 2016 at intersection of 30 Ave. and Gateway Blvd., Edmonton, AB, Canada. (Youtube, 2018).....	149
Figure 5-2 Geometry of the numerical model. (a) Schematic of the physical model (Drawing not to scale); (b) Schematic of the geometry and boundary conditions of the numerical model.	150
Figure 5-3 Additional information of the numerical model. (a) Mesh refinement and inflation layer; (b) Model with water recirculation chamber (WRC) connected to the riser; (c) Model with benching (with five openings on its top wall) in the chamber.....	151
Figure 5-4 Simulated geyser event triggered by a surge front while downstream pipe is almost full pipe flow. (a) simulated and measured pressure at PG1; (b) simulated volume fraction of water.	153
Figure 5-5 Plot of detailed flow conditions for geyser triggered by a surge front while downstream pipe is almost full pipe flow. (a) Simulated water flow rate and area-averaged pressure at 0.01 m upstream and downstream of the chamber; (b) Simulated air velocity and pressure area-averaged across the top of the riser.	154
Figure 5-6 Simulated geyser event triggered by an entrapped air pocket with water existing in the riser. (a) simulated and measured pressure at PG1; (b) simulated volume fraction of water.	156
Figure 5-7 Plot of detailed flow conditions for geyser triggered by an entrapped air pocket with water existing in the riser. (a) Simulated water flow rate and area-averaged pressure at 0.01 m upstream and downstream of the chamber; (b) Simulated air velocity and pressure area-averaged across the top of the riser.	157
Figure 5-8 Simulated volume fractions of water for different mitigation methods on geyser triggered by a surge front while the downstream pipe is almost full pipe flow. (a) Water recirculation chamber; (b) Benching with openings; (c) Orifice plate ($d_o/D_r=0.5$).....	159
Figure 5-9 Simulated pressures at PG1 for geyser mitigating methods with geyser triggered by a surge front while downstream pipe is almost full pipe flow.....	160
Figure 5-10 Simulated pressure variations for Run C1 to C4. (a) Simulated pressures at PG1; (b) Simulated pressures on the orifice plate installed inside the riser and 0.76 m above the top of the chamber.....	161
Figure 5-11 Simulated water surfaces (solid symbols) and air/water interfaces (void symbols).	162

Figure 5-12 Simulated volume fractions of water for geyser heights. (a) Run C1, at $t = 3.4$ s, ruler length = 0.3 m; (b) Run C2, at $t = 3.45$ s, ruler length = 0.3 m; (c) Run C3, at $t = 2.15$ s, ruler length = 0.3 m; (d) Run C4, at $t = 1.15$ s, ruler length = 0.4 m.163

Figure 6-1 Geyser events in Edmonton at different locations. Youtube (2018). (Youtube, 2018)183

Figure 6-2 Schematic of the control volumes for theoretical calculation.184

Figure 6-3 Comparison between theoretical calculated and physical measurement. Flow rate increase from 20 – 40 L/s, initial water slug length 0.3 m. (a) Measured and calculated free surface and interface, OP: $d = 0.5D_r$; (b) Measured and calculated pressure, OP: $d = 0.5D_r$; (c) Measured and calculated free surface and interface, OP: $d = 0.1D_r$; (d) Measured and calculated pressure, OP: $d = 0.1D_r$; (e) Model validation with Chan et al. (2018).187

Figure 6-4 Theoretical calculated peak pressure and the orifice size for PVC pipes Run A, (a): With different driving pressure at $(Y_1 - Y_0)/L = 0.39$; (b) With different initial water slug length at $H_0 = 1$ m.188

Figure 6-5 Theoretical calculated peak pressure and the orifice size for PVC pipes Run C and D, $H_0 = 1$ m, $(Y_1 - Y_0)/L = 0.3$. (a) With different riser diameter, $L = 1.22$ m; (b) With different riser height, $D_r = 0.055$ m.189

Figure 6-6 Theoretical calculated maximum peak pressure for Run A, C, and D.190

Figure 6-7 Theoretical calculated maximum peak pressure for Run E.191

Figure 6-8 Theoretical calculated orifice size when the maximum peak pressure occurs.192

1. General Introduction

1.1. Research background

Uncontrolled air movement in sewer systems can cause a variety of issues. The current design guidelines for sanitary and storm sewers only consider the conveying capacity for the liquid phase with less attentions on the air flow (Edwini-Bonsu and Steffler, 2004). As a result, many municipalities are facing problems such as odor issues in sanitary sewer systems, and geyser issues in storm sewer systems. These issues can lead to public health and safety concerns, or even system failure.

In Edmonton, Alberta, Canada there were over 7000 sewer odor complaints filed from 2009 to 2016 with a peak of 1271 complaints in 2011 (Edmonton Journal, 2017). The Edmonton's sanitary system comprises about 3000 km of pipes, over 800 drop structures, and over 25,000 manholes (City of Edmonton, 2018). Drop structures which deliver wastewater from one level to another are believed as the major contributor to the sewer odor issue, because they pressurize the headspace in the downstream pipes, and eventually lead to the release of sewer air (Zhang et al., 2016). Figure 1-1 is a photograph taken during a fieldwork in the winter of 2016 in Edmonton at around -20 °C. It can be seen that the sewer air shot out of the manhole as mists due to the pressurization resulted by the nearby drop structures.

Current studies mainly focus on the air movement in specific sewer structures such as drop structures (Ma et al., 2016, Zhang et al., 2016), and sewer pipes (Edwini-Bonsu and Steffler, 2004). However, in a prototype sewer system, the combined effects of individual structures on air flow need to be considered as well. As presented in the Figure 1-2, with the headspace being pressurized

in the trunk by the drop structures, the air is leaked from the lateral pipes via openings. The lateral connections with a higher air leakage flow would be the potential hotspots for odor issue. Currently, there are no tools or models that practically predict the air movement in sewer systems especially with drop structures. Therefore, it is important to understand how the air is transported in sewer pipes and how the air is moving in a prototype sewer network with the existence of drop structures.

In storm sewer systems, many municipalities are facing geyser issues as shown in Figure 1-3. The sudden increased water level in the sewer tunnels induced by heavy storm events and the releasing of the trapped air in the system via manhole shafts may push the air/water mixture out of the manhole and cause geyser events (Wright et al., 2011). The geyser events can lead to the blow-off of manhole covers. The flying manhole covers and the manholes without covers can induce potential risk of public safety. News were reported on accidents related to the flying or missing manhole covers: a driver was killed by a flying manhole cover in Boston in 2016 (CBS NEWS, 2016); a pedestrian fell into manhole due to a manhole blown off in Edmonton in 2018 (CBC NEWS, 2018).

Previous researches conducted on the mechanisms of geyser events were mostly on idealized laboratory scale models without referring to prototype systems (Cong et al, 2017). There are also limited studies on the geyser mitigation methods. Simple geyser mitigation methods were only qualitatively proposed (Lewis, 2011). The numerical model developed for the geyser events are mostly 1D models, which mostly focus on the pressure transient without detailed analysis on the air/water interaction (Zhou et al., 2002). To propose feasible geyser mitigation methods to

municipalities, it is therefore necessary to systematically study the mechanism and the potential ways to mitigate the storm geysers based on the prototype storm sewer system.

1.2. Thesis outline

This thesis is composed of four topics to address the issues discussed above. Each study is presented in a separate chapter. Following is the brief introduction of each chapter.

Chapter 2 is a comprehensive literature review on air movement in sewer systems. The literature on air movement in a single pipe is firstly reviewed followed by the air movement in sewer networks. The literature on the geyser events in storm sewer systems is also reviewed. This chapter provides a general foundation for the air movement in sewer systems. The gaps between the studies from the previous literature and the engineering applications on specific sewer designs is identified.

The first study presented in the chapter 3 is “**Air Movement Induced by Water Flow with a Hydraulic Jump in Changing Slope Pipes**”. In this study, air flows in both straight pipe and pipes with varied slopes are studied. The combined effects of the water drag and the pressure gradient along the pipe are analyzed numerically. Then a general method for estimating the air flow rate in a sewer pipe is proposed. The objectives of this study are to understand the interaction of air and water in a single sewer pipe under different flow conditions and to build the fundamentals for the analysis of the air flow in prototype sewer networks.

The second study presented in chapter 4 is “**Air Flow Modelling in a Prototype Sanitary Sewer System**”. In this study, the results of the first study are applied to study a prototype sewer network,

and a steady-state model is developed for simulating the air pressure and the air movement in a prototype sewer pipe network with 2 drop structures and a pump station. The objective of this study is to develop a general model to predict the pressure distribution in the studied sewer network for locating potential sewer odor hotspot.

The third study presented in the chapter 5 is “**Numerical Study on the Mechanism and Mitigation of Storm Geysers**”. In this study, a 3D computational fluid dynamic transient model is built. Two distinctive geyser patterns are tested and analyzed: a surge wave front with almost full pipe flow downstream; and the release of an entrapped air pocket with water initially existing in the riser. Potential mitigation methods are proposed and assessed numerically using the CFD model. The objectives of this study are to understand the detailed air/water interaction during a geyser event and to propose feasible geyser mitigation methods.

The fourth study presented in the chapter 6 is “**Analytical Model on the Geyser Event in Storm Sewer Systems**”. In this study, an analytical model is developed to predict the pressure variation in sewer systems during geyser events when the orifice plate is installed at the top of the riser. The water-hammer like pressure induced by the impingement of the water slug on the orifice plate is analyzed. The objective of this study is to obtain the relationship between orifice opening sizes and the water-hammer like pressure as well as other relevant parameters such as the riser diameter, riser height, pipe materials, etc.

Chapter 7 provides some general conclusions. Recommendations on the direction of further studies are also proposed.

References

CBC NEWS (2018). “Pedestrian falls into manhole after downtown Edmonton explosion.” Online. [<http://www.cbc.ca/news/canada/edmonton/downtown-explosion-manhole-cover-1.4480694>, Accessed 30-Apr.-2018]

CBS NEWS (2016). “Boston driver killed by flying manhole cover identified.” Online. [<https://www.cbsnews.com/news/flying-manhole-cover-kills-driver-in-boston/>, Accessed 20-Apr.-2018].

City of Edmonton (2018). “Sewer Facts and Statistics.” Online. [https://www.edmonton.ca/city_government/utilities/sewer-facts-and-statistics.aspx, Accessed 27-Mar.-2018].

Cong, J., Chan, S. N., and Lee, J. H. W. (2017). “Geyser formation by release of entrapped air from horizontal pipe into vertical shaft.” *Journal of Hydraulic Engineering*, 10.1061/(ASCE)HY.1943-7900.0001332.

Edmonton Journal (2017). “City plans sewer-odour strategy after thousands of complaints.” Online. [<http://edmontonjournal.com/news/local-news/city-plans-sewer-odour-strategy-after-thousands-of-complaints>, Accessed 01-May-2018]

Edwini-Bonsu, S., and Steffler, P. M. (2004). “Air flow in sanitary sewer conduits due to wastewater drag: a computational fluid dynamic approach.” *Journal of Environmental Engineering and Science*, 3(5): 331-342.

Lewis, J. M. (2011). “A physical investigation of air/water interactions leading to geyser events in rapid filling pipelines.” *PhD thesis*, University of Michigan, Ann Arbor, Michigan.

Ma, Y., Zhu, D. Z., and Rajaratnam, N. (2016). “Air entrainment in a tall plunging dropshaft.” *Journal of Hydraulic Engineering*, 10.1061/(ASCE)HY.1943-7900.0001181, 04016038.

Wright, S. J., Lewis, J. W., and Vasconcelos, J. G. (2011). "Physical processes resulting in geysers in rapidly filling storm-water tunnels." *Journal of Irrigation and Drainage Engineering*, 137(3): 192-202.

Youtube (2016). "Edmonton's Old Faithful." Online. [https://www.youtube.com/watch?v=pvGfmwYvXtg, Accessed 25-Feb.-2018]

Youtube (2013). "Exploding Storm Sewer Lifts Car in Montreal" Online. [https://www.youtube.com/watch?v=a1VulahjR68&t=8s, Accessed 20-Apr.-2018]

Zhang, W. M., Zhu, D. Z., Rajaratnam, N., Edwini-Bonsu, S., Fiala, J., and Pelz, W. (2016). "Use of air circulation pipes in deep dropshafts for reducing air induction into sanitary sewers." *Journal of Environmental Engineering*, 142(4): 04015092. 10.1061/(ASCE)EE.1943-7870.0001046.

Zhou, F., Hicks, F. E., and Steffler, P. M. (2002). "Transient flow in a rapidly filling horizontal pipe containing trapped air." *Journal of Hydraulic Engineering*, 128(6): 625-634.



Figure 1-1 Photo of the air flowing out of the manhole due to a high pressure in the sewer system.

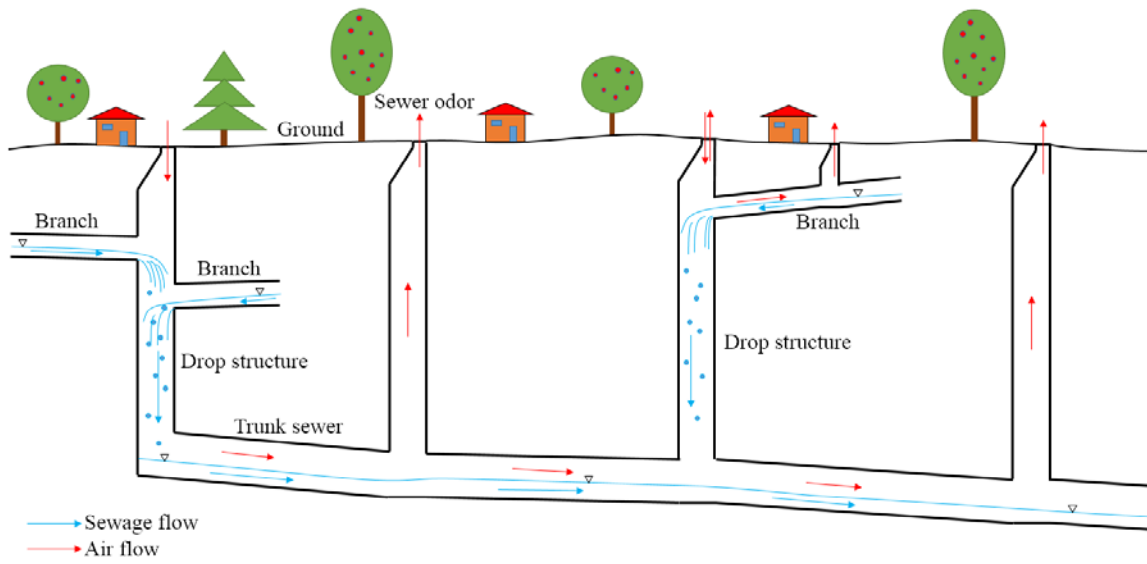


Figure 1-2 Conceptual drawing of an idealized sewer system.



Figure 1-3 Images of geyser events happened worldwide. (a) Geyser event at Petro-Canada Station, Edmonton, in 2016 (Youtube, 2016); (b) Geyser event at Nofrills, Edmonton (Courtesy by Epcor) (c) Geyser event at Minneapolis in 1997 (Wright et al., 2011); (d) Geyser event at Montreal in 2011 (Youtube, 2013).

2. Literature Review

2.1. Introduction

In sanitary sewer systems, under anaerobic condition, hydrogen sulfide (H_2S) can be produced in the biofilms at the pipe wall and sediments. H_2S is the main cause of sewer pipe corrosion and is responsible for odor issues (U.S. EPA, 1985). In storm sewer systems, the rapid filling of water in the sewer pipes can lead to flow transients in the system (Zhou et al., 2002). The uncontrolled air flow in the storm sewer systems may cause geyser event, manhole cover blow-up etc. Therefore, understanding the air movement in sewer systems is important for mitigating the odor and geyser issues in sanitary and storm sewer system respectively.

The earliest study on the air movement in sewer systems started in 1940s when Kalinske and Robertson (1943) experimentally studied the air entrainment due to hydraulic jumps. Later studies verified their results and improved the understanding of air entrainment induced by a hydraulic jump (Escarameia, 2007; Mortensen et al., 2011). Pescod and Price (1982) proposed the major factors affecting the air flow in sewer pipes. The effects of wastewater drag and pressure difference on air flows in sewer pipes were studied by Edwini-Bonsu and Steffler (2004, 2006a). The air movement in sewer networks was studied by Edwini-Bonsu and Steffler (2006b) when they modelled the air flow in a sewer network using a system dynamic model. For geyser event in storm sewer systems, Hamam and McCorquodale (1982) developed one dimensional model to simulate the transient pressure change during a geyser event. The later numerical models were mostly developed based on their studies.

This chapter provides a comprehensive literature review on the air movement in sewer systems. The air movement in a single sewer pipe is firstly reviewed including field measurements, laboratory experiments, and theoretical models followed with the literature review on the air movement in sewer networks. The next part of this chapter is on geyser events in storm sewer system. Previous experimental studies, theoretical and numerical models, and field measurements on geyser events were reviewed. The development of numerical model is also reviewed, and finally, the knowledge gaps between the current understanding on this topic and the practical engineering needs are identified.

2.2. Air movement in single sewer pipes

The air movement in a single sewer pipe is the foundation of the air movements in sewer systems. Pescod and Price (1982) experimentally studied the air flow in a sewer pipe under a variety of conditions. An idealized air velocity contour was proposed and shown in Figure 2-1. Factors that control the air flow in sewer pipe include: drag of wastewater, pressure difference, wind across stack, temperature, barometric pressure, and fluctuation of water level. The air velocity profile at pipe center plane was measured. However, there are no quantitative analysis on the relationship between air flow and water flow. Lowe (2016) discussed factors affecting air flow and modelling approaches, and summarized the factors as: wastewater drag, air pressure, dropshafts, buoyancy effects, CSO storage tunnels, and siphons. However, there were no quantitative discussions on these factors. U.S. EPA (1994) provided models to estimate the air demand in sewer systems. Different scenarios were considered in the report including the air flow in sewer pipe and air flow via manhole pickholes due to wastewater drag, wind pressure, and density differences. Olson et al.

(1997) theoretically studied the effects of liquid drag in industrial sewer drains using energy concepts.

Edwini-Bonsu and Steffler (2004) numerically studied the air flow in a sewer pipe due to the drag of wastewater. A two-dimensional model was built to solve the air velocity contour induced by the drag of wastewater. The Reynolds-Averaged-Navier-Stokes equations with the continuity equation were solved numerically. Relationship between air flow and water flow was proposed as:

$$\frac{V_a}{U_w} = 1.028 \frac{C}{(L+C)} \quad (2-1)$$

$$\frac{V_a}{U_{wc}} = 0.8560 \frac{C}{(L+C)} \quad (2-2)$$

where V_a is the bulk average velocity of air, U_w is the average water surface velocity, U_{wc} is the water surface velocity at channel center, C is the width of air-water interface, and L is the perimeter of the unwetted headspace. Equation 2-1 is for laminar flow and equation 2-2 is for turbulent flow.

Later, Edwini-Bonsu and Steffler (2006a) updated their older model (Edwini-Bonsu and Steffler, 2004) by including the effect of pressure differences on the air flow. It was found that for laminar flow, the effects of wastewater drag and pressure difference followed a simple additive rule and can be written as:

$$\frac{V_a}{U_w} = 1.028 \left[\frac{C}{(L+C)} \right] + \alpha \left\{ 0.088 \left[\frac{C}{(L+C)} \right]^2 + 0.0079 \left[\frac{C}{(L+C)} \right] + 0.0313 \right\} \quad (2-3)$$

where $\alpha = \frac{(-dp/dx)b^2}{(\rho_a \nu U_w)}$, p is pressure, ρ_a is air density, ν is the kinematic viscosity, b is the width of the flow. Nevertheless, for turbulent flow, the additive rule did not apply. A set of charts was proposed to estimate the combined effect of wastewater drag and pressure difference. This study provided a way to estimate the air flow in a single sewer pipe. However, the range of calculation

was limited by the range of the chart. For flow condition out of the range of the chart, the estimation cannot be proceeded.

The air flow in a conduit is also important in dam outlet works. U.S. ACE (1980) analyzed field measurement and proposed the empirical equation for estimating the air flow demand that can be written as:

$$\frac{Q_a}{Q_w} = 0.03(F - 1)^{1.06} \quad (2-4)$$

where Q_a is the flow rate of air, Q_w is the flow rate of water, F is the Froude number of water flow, $F = V_w/(gh)^{0.5}$, in which V_w is the water velocity and h is the depth of the flow.

Larchar (2011), Tullis and Larchar (2011), Wright (2013), and Wright and Tullis (2014) studied the air demand in low-level outlet works. They measured the air demand under different flow scenarios. The ratio of air and water flow rates was found to be a function of the filling ratio and had a maximum value of about 1.0. Volkart and Speerli (1994) measured the air demand in a high head dam and found that the airflow rate reached up to 50 times the water flow rate as the high-speed water became spray. Speerli and Hager (2000) observed the airflow in conduits and observed countercurrent air movement. However, the effect of pressure generated on airflow in the conduit was not assessed.

For water flow with a hydraulic jump in pipes, Kalinske and Robertson (1943) experimentally measured the air entrainment induced by a hydraulic jump and proposed an empirical equation:

$$\frac{Q_a}{Q_w} = 0.0066(F - 1)^{1.4} \quad (2-5)$$

Escarameia (2007) studied the air removal effect of a hydraulic jump in a pipe and updated Eq. 2-5 based on experimental measurements as:

$$\frac{Q_a}{Q_w} = 0.0025(F - 1)^{1.8} \quad (2-6)$$

Mortensen et al. (2011) suggested that the relationship between air and water flow induced by a hydraulic jump was a linear function:

$$\frac{Q_a}{Q_w} = (2.340F - 5.248)/100 \quad (2-7)$$

It is notable that equations 2-5, 2-6, and 2-7 yield similar Q_a/Q_w values for the same Froude number upstream of the jump. The Q_a/Q_w values are 0.143, 0.130, and 0.181 respectively for Froude number of 10. Therefore, there is no fundamental difference among these studies. These studies mainly focused on the transportation of air through a hydraulic jump in the form of bubbles which meant that the downstream of the hydraulic jump was full pipe flow. For the hydraulic jump with downstream open channel flow condition, the air transported may be different.

Figure 2-2 is a schematic of a control volume for air flow analysis in a sewer pipe. For a given air flow without momentum change, the force exerting on it should be balanced. The force due to the pressure gradient and the friction force can be calculated directly. However, the drag coefficient between the water surface and the air in a pipe with the existence of pressure gradient is still unclear. Therefore, it is necessary to study the movement of air in pipes with combined effect of the water drag and pressure gradient.

2.3. Air movement in pipe networks

The air movement in pipe networks did not receive much attentions until 2000s. Edwini-Bonsu and Steffler (2006b) modelled the air flow in a sewer network using system dynamic approach.

The pressure change due to dropshafts were modelled as a quadratic equation:

$$\Delta p = \gamma Q_w^2 + \alpha Q_w + \beta \quad (2-8)$$

where Δp is the pressure change due to dropshafts γ , α , and β are parameters to determine the characteristic function. In their study, these parameters were chosen based on assumptions and were not fully validated. Further studies was recommended on the effect of dropshafts on downstream headspace pressurization.

Parker and Ryan (2001) measured the air velocity in a prototype sewer system. Carbon Monoxide was used as a tracer to measure the velocity of air flowing in the headspace of sewer pipes. It was found that the measured air velocities varies from 3 to 30 m/min at different locations. Ward, Corsi et al. (2011) developed a model for estimating the air movement in a sewer trunk by solving momentum equations. The model was then validated by field measurement (Ward, Hamer et al., 2011). Wang et al. (2012) developed a full dynamic airflow model for gravity sewer networks. The model solved momentum equations and continuity equation using finite element method. The model was calibrated with field measurements. However, the effect of dropshafts has not been discussed in the above studies even though it is the key factor of the headspace pressurization in sewer systems. The above models may not be applicable to the sewer systems with dropshafts. Therefore, knowing the effect of dropshafts on the pressurization of the sewer headspace is essential to understand the air movement in sewer systems. It is also important to convert the outcome of the lab study on dropshafts into prototype applications.

For the studies on dropshafts, Anderson and Dahlin (1975) experimentally investigated the hydraulic operating characteristics for various flow conditions. Rajaratnam et al. (1997) did some of the earliest studies on dropshafts. Chanson (2007, 2009) did extensive studies on dropshafts. A model scale dropshaft with a height (H_s) of 0.98 and 2.9 m, a diameter (D_s) of 0.29 m was built and studied, and the relationship between the relative air flow rate (Q_a/Q_w) and the dimensionless water flow rate ($Q^* = Q_w/(gD_s^5)^{0.5}$) was proposed based on the experimental results. Camino et al. (2014) summarized the previous studies and found that the air flow in dropshafts did not follow the scale law. An empirical equation was proposed to estimate the relative air flow rate for a model scale dropshaft with a height of 6.30 m and a diameter of 0.20 m:

$$\frac{Q_a}{Q_w} = 0.5/\sqrt{Q^*} \quad (2-9)$$

The air flow was also found depending on the values of H_s/D_s . In general, dropshafts with large H_s/D_s results more air intake for a given Q^* .

Ma et al. (2016) experimentally studied the air entrainment in a dropshaft which was the same dimension as Camino et al. (2014). The experimental results show that the water would break from continuous flow into droplets when it was dropping along the dropshaft. The contact area between the air and the water increased dramatically. As a result, more air was dragged into the dropshaft by the droplets. The control volume in a dropshaft is shown in Figure 2-3, and a conceptual model was developed to predict the pressure change in the air space due to the air/water moment transfer:

$$\frac{dp}{dz} = \frac{3Q_w}{\pi D_s^2 d} C_d \rho_a V_t \left(1 - \frac{V_a}{V_t}\right)^2 \quad (2-10)$$

where d is the diameter of water drops, C_d is the drag coefficient of drops, $C_d = 0.4$, V_t is the terminal velocity of drops and $V_t = 6$ m/s in their study. Zhang et al. (2016) analyzed the field

measurement for a prototype dropshaft that was retrofitted with an air recirculation shaft. It was found that the air circulation systems were an effective way to depressurize a sewer system. However for sewer system with two dropshafts in series, it is recommended to retrofit the one with highest drop height.

For the air movement in prototype sewer network, Guo et al. (2018) measured the pressure and H₂S concentration change in a prototype sanitary sewer system. The system has a dropshaft at the very upstream and in the middle of the trunk. A pump station is located at the downstream of the trunk and air cannot move further downstream. It was found that the dropshaft located at the very upstream was responsible for the pressurization of the trunk sewer pipe. The pressure measured in the trunk had obvious diurnal change and agreed well with the diurnal change of the wastewater flow rate. For the manholes close to the pump station, the operation of pump station would induce a bursting pattern to the pressure change.

The studies above focus more on the air movements in specific sewer structures such as drop structures or simple sewer networks. The application of the effect of drop structures on sewer networks is based on assumptions without justifications. The air leakage via lateral pipes due to the pressurization of the trunk headspace is still unknown. Also, there is no model predicting the pressure distribution along a prototype sewer system with the existence of dropshafts. Therefore, it is necessary to develop a conceptual model to utilize the existence knowledge on predicting air movement in prototype sewer systems especially with drop structures and lateral connections.

2.4. Modeling on extreme flow conditions in sewers

The rapid change of stormwater flow rate can lead to transient pressure variations in sewer systems. The transient pressure can trigger water hammer pressure, system damage, etc. Li and McCorquodale (1999) improved the Rigid Column Model to allow the transport and subsequent release of the trapped air pocket. The governing equations and control volumes at each stages were discussed in detail. Figure 2-4 shows the control volume of the model, and governing equations can be written as:

$$\frac{dV_A}{dt} = \frac{g}{L_A} \left[H_I - \frac{V_A^2}{2g} - \frac{K_A V_A |V_A|}{2g} \right] - \frac{p_a + \gamma_w h_B A_B / 2A_p}{\rho_w L_A} + gS_0 - f_A \frac{V_A |V_A|}{8R_A} + \frac{V_A V_b}{L_A} + \frac{V_A |V_A|}{L_A} - \frac{V_A |V_A + V_b|}{L_A} - \frac{(V_A + V_b)(V_B - V_A)}{L_A} \quad (2-11)$$

$$\frac{dV_B}{dt} = gS_0 - f_B \frac{V_B |V_B|}{8R_B} + \frac{V_B A_p (V_A - V_C)}{A_B L_B} \quad (2-12)$$

$$\frac{dV_C}{dt} = -\frac{g}{L_C} \left[H_F - \frac{V_C^2}{2g} + \frac{K_C V_C |V_C|}{2g} \right] + \frac{p_a + \gamma_w h_B A_B / 2A_p}{\rho_w L_C} + gS_0 - f_C \frac{V_C |V_C|}{8R_C} - \frac{V_C V_b}{L_C} - \frac{V_C |V_C|}{L_C} + \frac{V_C |V_C + V_b|}{L_C} - \frac{(V_C + V_b)(V_C - V_B)}{L_C} \quad (2-13)$$

where the subscripts A , B , and C indicate the control volumes of A, B and C respectively, L is the length of water column, V_b is the velocity of the air bubble, p_a is the gauge pressure in the air bubble, h is the depth of water in the pipe, f is the steady-state pipe friction factor, A is the flow area of the pipe, S_0 is the slope of the pipe, H_I and H_F is the water depth at the upstream and downstream manhole respectively.

It was found that the model overestimated the range of pressure transients and underestimated the damping of the pressure transient, and the model was able to simulate the pressure transient with a relative difference of 20% compared with physical model. Future studies on the multiple bubbles,

the effect of turbulence, the surface instability and field measurement on pressure transient during a geyser event were recommended.

Zhou (2000), Zhou et al. (2002), and Zhou et al. (2004) experimentally studied the pressure transient when a water column impinged the horizontal pipe end with an orifice plate. The pressure peak related to the size of the orifice plate and could reach up to 15 times of the driving pressure when the orifice size was around 0.2 times of the pipe diameter. A mathematical model was proposed to predict the pressure change during geyser events, and the simulated results agreed well with the experimental data. The control volume of the model is shown in Figure 2-7. The governing equations of the model can be written as (Zhou et al. 2002)

$$\frac{dH^*}{dt} = -k \frac{H^*}{V_a} \frac{dV_a}{dt} - k \frac{H^*}{V_a} Q_a \quad (2-14)$$

$$Q_a = C_d A_0 \sqrt{2g \frac{\rho_w}{\rho_a} (H^* - H_b^*)} \quad (2-15)$$

$$H_2 = H_1 + \frac{a}{g} \left(V_1 + \frac{a}{B} - \sqrt{\left(\frac{a}{B}\right)^2 + 2V_1 \frac{a}{B} + \frac{2gH_1}{B}} \right) \quad (2-16)$$

where the asterisk denotes the absolute pressure head, H is the air pressure head, k is polytropic exponent, C_d is the discharge coefficient of the orifice and $C_d = 0.65$ (Zhou et al. 2002), a is the speed of the pressure wave when the water column reaches the orifice, B is a coefficient and $B = (A/A_0)^2 + K - 1$, A , A_0 are the area of the pipe and the orifice opening respectively, V_1 and H_1 are the velocity and pressure head at section 1-1 respectively.

The model compared well with experimental data especially the pressure oscillation behavior and the peak pressure. Further studies were recommended on the field measurement in real sewer systems with dropshafts, horizontal pipe with varied cross section area, etc.

For numerical models on predicting the pressure transient in sewer systems, Leon et al. (2006, 2009) developed a one-dimensional model for predicting the pressure transient in sewer systems by solving the continuity equation using finite volume Godunov-type schemes. The gravity flow with no surcharging condition was successfully modelled. Leon et al. (2010) updated the previous model and extended the objective to two phase transient flow. Two governing equations were solved. Apart from the continuity equation, the ideal gas law was involved to simulate the interaction between air and water:

With no air release:

$$\frac{dH}{dt} = -k \frac{H^*}{V} \frac{dV}{dt} \quad (2-17)$$

With air release:

$$\frac{dH}{dt} = -k \frac{H^*}{V} \frac{dV}{dt} + k \frac{H^*}{m} \frac{dm}{dt} \quad (2-18)$$

where m is the mass of the air pocket. Equation 2-18 is a combination of equations 2-14 and 2-15.

Bouso et al. (2013) summarized the previous studies on the geyser event with special focus on numerical methods. The previous numerical models can be summarized into two categories (Single-equation and Two-equation model) according to the number of equations. The Single-equation model solved the Saint-Venant equations. The solving methods for Single-equation model included Preissmann Slot Principle, which was firstly developed by Cunge and Wegner (1964), and Two-component Pressure Approach, which was proposed by Vasconcelos and Wright (2007, 2009). The Single-equation models were generally simple to apply, require less computing time and memory, and were reasonably accurate on calculating pressurized flow with lower pressure wave velocity or in the presence of sub-atmospheric flow (Vasconcelos and Marwell,

2011). The model also present adequate compression/expansion cycles of entrapped air pockets (Vaconcelos et al., 2015). However, the models solved only water phase, and the air phase integrating was limited. The models also needed approximations for simulating pressurized flows. Finally, the models generated unrealistic negative pressures but it could be addressed by adequate choice of numerical schemes (e.g., Vasconcelos et al., 2009; Malekpour and Karney, 2015).

The Two-equation model solved the continuity equation and the ideal gas law equation. The Interface Tracking Model was developed by Wiggert (1972), the Rigid Column-Based Model was introduced by Li and McCorquodale (1999), and the Finite-Volume Strategy model was proposed by Leon et al. (2010). The Two-equation models handled the changes in the acoustic wave speed due to a sub-atmospheric pressure and allowed better simulation of the low piezometric flows. The models also accommodated the effect of air. The air-water interfaces can be better modelled using the models, and using high acoustic wave speed would not cause stability issues in the models. Nevertheless, the Two-equation models needed more computing time and memory and were complex to implement. Bousso et al. (2014) and Bousso and Fuamba (2014) developed a rigid-column based numerical models to solve the transient of rapid pipe filling. The rigid-column approach had limitations in long pipes. A model with discretized water column and pressurized air pocket was recommended for further study.

2.5. Previous investigations in geysers

When experiencing heavy rain events, the storm sewer pipe can be filled up and change from open channel flow to full pipe flow. Air can be trapped at the crown of the sewer pipe when the

downstream pipe has limited capacity. The entrapped air has to be released somewhere. Water can be brought by the releasing air and therefore, a geyser event is formed.

Hamam and McCorquodale (1982) developed a Rigid Column Method for predicting the transient pressure change during a geyser event. The model treated the water as incompressible flow, the air pocket was stationary and the trapped air pocket underwent a pseudo-adiabatic expansion and compression process. The following recommendations were suggested for decreasing the risk of pressure transient in sewer (Hamam and McCorquodale, 1982): (a) over-sizing the sewer pipes; (b) providing adequate venting of the line; (c) provision of adequate standby power for pumped sewer systems; (d) improved design of interceptors and drop-pipes; (e) use of rectangular conduits for large sewers with high velocities; (f) regular maintenance of the system to avoid collection of debris that could clog outfall screens; (g) careful analysis and design of pumped inflows to the system; (h) good grade control and backfilling of the sewer; and (i) installation of air-jumpers at inverted siphons. Song et al. (1983), Guo and Song (1990, 1991) studied the surging in urban drainage systems. It was proposed that reducing the inflow and building a surge tank at the upstream end were able to prevent the transient problems.

Wright et al. (2008), Wright et al. (2011a, 2011b) and Lewis (2011) conducted a series of studies based on field measurements. A sample pressure change during a geyser event was measured and plotted in Figure 2-5. It can be seen that the pressure in the pipe increased continuously and exceeded the pipe crown. The pressure dropped abruptly at the onset of each geyser. However, the pressure head was not large to reach the ground level. It was pointed that for the sewer sections with relatively flat slope, the geometry change would produce a mildly submerged flow in the

flatter section while remain open channel flow in both upstream and downstream. The free surface change provided a potential air flow along the trunk and releasing from the manhole at the flatter area.

The mechanism of geyser events in storm sewer pipes was proposed and shown in Figure 2-6. According to the figure, the air was trapped at the crown of the pipe due to a variety of reasons such as the air transportation of hydraulic jump, rapid filling of sewer pipes, pipe slope change, etc. When the pressurized air pocket moved to a manhole, the air could be released. Water remaining in the manhole shaft was pushed upward by the air and if the water column reached the manhole cover, geyser event happened. Meanwhile when the air was pushing the air slug upward, the water in the riser flowed downward in the form of a thin film along the shaft wall. The high velocity of air flow in the manhole shaft sheared the water film flow along the shaft wall and formed geyser events.

Vasconcelos et al. (2006, 2015), Vasconcelos and Wright (2005, 2007, 2009, and 2011) conducted a series of researches on the geyser in storm sewer systems including experimental and numerical studies. Vasconcelos et al. (2006) numerically solved the Saint-Venant equations for open channel flows. The model was a one-equation one-dimensional two-component model assuming the elastic behavior of the pipe and the results compared well with the experimental data. Based on the study of Vasconcelos et al. (2006), Vasconcelos et al. (2015) proposed a model composing with the continuity equation and the ideal gas law. The model incorporated the effect of the air phase in the previous model. The location of the trapped air pocket can be estimated by the model. The physical experiment by Vasconcelos and Wright (2011) focused on the geyser induced by large air pocket

in pipe. A numerical model was developed to solve the air-water interaction in a horizontal pipe connected to a vertical pipe with a T-junction. It was pointed out that when the water column was pushed upwards, a Taylor bubble formed in the vertical riser and the water leaked downwards in the form of a thin film. The possible shear flow instabilities between the film and the air flow could not be assessed by the experiment. In the above studies, the riser was directly connected to the horizontal pipe. If the riser connected with the horizontal pipe with a chamber, the analysis above may not be applicable.

Shao (2013) developed a two-dimensional hydrodynamic model of two-phase flow for modelling the geyser phenomena in storm water system. The model numerically solved Navier-Stokes equations coupled with the ideal gas law and the volume of fluid equations. Choi et al. (2014) successfully modeled the geyser event using a three-dimensional model. Choi et al. (2016) proposed a one-dimensional model predicting the pressure variation in a vertical shaft partially filled with stagnant water. However, the model was validated with 3D numerical models and the validation with physical model is insufficient. Chan et al. (2018) developed a 3D CFD model to simulate the geyser process based on the physical study of Cong et al. (2017). Li and Zhu (2018) numerically modeled the effect of the air pocket on the water hammer pressure induced by the impingement of the water column to the pipe end with an orifice. Muller et al. (2017) developed a CFD approach on solving geyser events. It was found that the CFD model was able to simulate the air/water interaction during the releasing of air pocket. However, the CFD models did not simulate the actual geyser events where the water was ejected out of the riser.

Huang (2017) systematically studied the geyser event physically, analytically, and numerically. It was found that the installation of orifice plates can significantly reduce the pressure peak during a geyser event. The smaller the orifice size corresponded a more effective result on reducing the pressure oscillation. It was also found that the installation of orifice plates was more efficient than changing the size and height of ventilation shaft on mitigating the geyser events. Multiple ventilation shafts also had positive effect on reducing the pressure during geyser events. It was found that if the trapped air cannot be released via ventilation tower, it would be transported downstream. The pressure oscillation due to the deformation of air pocket is less than the geyser event but it can still cause geyser events further downstream.

Although geyser mitigation methods were proposed in previous studies, the detailed analysis was still missing, and the mechanism was mostly studied using idealized connection instead of the prototype connections. Therefore, it is important to analyze the mechanism of geyser events using prototype connections and assess the effectiveness of geyser mitigation methods quantitatively to address the geyser issues faced by municipalities.

2.6. Knowledge gaps

The air movement in a single sewer pipe due to the drag of wastewater drag and pressure difference at upstream and downstream ends is generally well studied but still with gaps for practical applications. Physical experiments were conducted but with no quantitative relationships developed (Pescod and Price, 1982). However, the gap still exists at the numerical simulation especially on the 3D two-phase simulation for resolving the free surface and the interaction of air

and water. Also, for air movement in sewer networks, there is no tool or model that practically predicts the air movement in the sewer systems with a dropshaft. The mechanism of geyser events in storm sewer systems is still unclear, especially for storm sewer with a rapid change water flow rate. The numerical models developed for the geyser events were mostly 1D model with more focus on the pressure transient. Physical and 3D numerical model on the geyser events in storm sewer systems was needed.

References

Anderson, A. G., and Dahlin, W. (1975). "Model Studies of Dropshafts for the Tunnel and Reservoir Plan." *Report*. St. Anthony Falls Hydraulic Laboratory, University of Minnesota.

Bouso, S., and Fuamba, M. (2014). "Numerical and experimental analysis of the pressurized wave front in a circular pipe." *Journal of Hydraulic Engineering*, 140(3): 300-312.

Bouso, S., Daynou, M., and Fuamba, M. (2013). "Numerical modeling of mixed flow in stormwater systems: critical review of literature." *Journal of Hydraulic Engineering*, 139(4): 385-396.

Bouso, S., Daynou, M., and Fuamba, M. (2014). "Mixed flows with depressurizing wavefront in circular pipe." *Journal of Irrigation and Drainage Engineering*, 140(1): 1-10.

Camino, G. A., Zhu, D. Z., and Rajaratnam, N. (2014). "Flow observations in tall plunging flow dropshafts." *Journal of Hydraulic Engineering, ASCE*, 141(1): 06014020.

Chan, S. N., Cong, J., and Lee, J. H. W. (2018). "3D numerical modeling of geyser formation by release of entrapped air from horizontal pipe into vertical shaft." *Journal of Hydraulic Engineering*, 144(3): 04017071.

Chanson, H. (2006). "Air bubble entrainment in hydraulic jumps, similitude and scale effects." *Research Report No. CE57/05*, Department of Civil Engineering, The University of Queensland.

Chanson, H. (2007). "Air entrainment processes in a full-scale rectangular dropshaft at large flows." *Journal of Hydraulic Research*, 45(1): 43-53.

Chanson, H. (2009). "Turbulent air-water flows in hydraulic structures: dynamic similarity and scale effects." *Environmental Fluid Mechanics*, 9(2): 125-142.

Chanson, H. and Brattberg, T. (2000). “Experimental study of the air-water shear flow in a hydraulic jump.” *International Journal of Multiphase Flow*, 26(4), 583-607.

Chanson, H. and Gualtieri, C. (2008). “Similitude and scale effects of air entrainment in hydraulic jumps.” *Journal of Hydraulic Research*, 46(1), 35-44.

Chanson, H. and Qiao, G. L. (1994). “Air bubble entrainment and gas transfer at hydraulic jumps.” *Research Report No. CE149*, Department of Civil Engineering, The University of Queensland.

Choi, Y. J., Leon, A. S., and Apte, S. V. (2014). “Three-dimensional numerical modeling of air-water geyser flows.” *World Environmental and Water Resources Congress*, June 1-5, Portland, Oregon.

Choi, Y. J., Leon, A. S., and Apte, S. V. (2016). “A one-dimensional numerical model to predict pressure and velocity oscillations of a compressed air pocket in a vertical shaft filled with water.” *World Environmental and Water Resources Congress*, May 22-26, West Palm Beach, Florida.

Cong, J., Chan, S. N., and Lee, J. H. W. (2017). “Geyser formation by release of entrapped air from horizontal pipe into vertical shaft.” *Journal of Hydraulic Engineering*, 143(9): 04017039.

Cunge, J. A., and Wegner, M. (1964). “Numerical integration of Saint Venant’s flow equations by means of an implicit scheme of finite differences. Applications in the case of alternately free and pressurized flow in a tunnel.” *La Houille Blanche*, 1: 33-39.

Edwini-Bonsu, S., and Steffler, P. M. (2004). “Air flow in sanitary sewer conduits due to wastewater drag: a computational fluid dynamic approach.” *Journal of Environmental Engineering and Science*, 3(5): 331-342.

Edwini-Bonsu, S., and Steffler, P. M. (2006a). “Dynamics of air flow in sewer conduit headspace.” *Journal of Hydraulic Engineering*, 132(8): 791-799.

Edwini-Bonsu, S., and Steffler, P. M. (2006b). "Modeling Ventilation Phenomenon in Sanitary Sewer Systems: A System Theoretic Approach." *Journal of Hydraulic Engineering*, 132(8): 778-790. 10.1061/(ASCE)0733-9429.

Escarameia, M. (2007). "Investigating hydraulic removal of air from water pipelines." *Water Management*, 160(1): 25-34.

Ferziger, J. H., and Peric, M. (2002). "*Computational Methods for Fluid Dynamics.*" 3rd edition, Springer: Berlin.

Guo, Q. and Song, C. S. S., (1990). "Surging in urban storm drainage systems." *Journal of Hydraulic Engineering*, 116 (12), 1523-1537.

Guo, Q. and Song, C. S. S., (1991). "Dropshaft hydrodynamics under transient conditions." *Journal of Hydraulic Engineering*, 117 (8), 1042-1055.

Guo, S., Qian, Y., Zhu, D., and Edwini-Bonsu, S. (2018). "Effects of Drop Structures and Pump Station on Sewer Air Pressure and Hydrogen Sulfide: Field Investigation." *Journal of Environmental Engineering*, 144(3): 10.1061/(ASCE)EE.1943-7870.0001336.

Hamam, M. A., and McCorquodale, J. A. (1982). "Transient conditions in the transition from gravity to surcharged sewer flow." *Canadian Journal of Civil Engineering*, 9: 189-196.

Hirt, C. W., and Nichols, B. D. (1981). "Volume of fluid (VOF) method for the dynamics of free boundaries." *Journal of Computational Physics*, 39: 201-225.

Huang, B. (2017) "Study on Geysers in Urban Drainage Systems." *PhD Thesis*, Nanjing Hydraulic Research Institute, Nanjing, China.

Kalinske, A. A. and Robertson, J. M. (1943). "Closed conduit flow." *Transactions, ASCE*, 108, 1435-1447.

Larchar, J. A. (2011). “*Air demand in low-level outlet works.*” MSc Thesis, Utah State University.

Leon, A. S., Ghidaoui, M. S., Schmidt, A. R., and Garcia, M. H. (2006). “Godunov-type solutions for transient flows in sewers.” *Journal of Hydraulic Engineering*, 132(8), 800–813.

Leon, A. S., Ghidaoui, M. S., Schmidt, A. R., and Garcia, M. H. (2009). “Application of Godunov-type schemes to transient mixed flows.” *Journal of Hydraulic Research*, 47(2), 147–156.

Leon, A. S., Ghidaoui, M. S., Schmidt, A. R., and Garcia, M. H. (2010). “A robust two-equation model for transient-mixed flows.” *Journal of Hydraulic Research*, 48(1): 44-56.

Lewis, J. M. (2011). “A physical investigation of air/water interactions leading to geyser events in rapid filling pipelines.” *PhD thesis*, University of Michigan, Ann Arbor, Michigan.

Li, J., and McCorquodale, J. A. (1999). “Modelling mixed flow in storm sewers.” *Journal of Hydraulic Engineering*, 125(11): 1170-1180.

Li, L., and Zhu, D. Z. (2018). “Modulation of transient pressure by an air pocket in a horizontal pipe with an end orifice.” *Water Science and Technology*, accepted.

Lowe, S. (2016). “Sewer ventilation: Factors affecting airflow and modeling approaches.” *Journal of Water Management Modeling*, doi: 10.14796/JWMM.C395.

Ma, Y., Zhu, D. Z., and Rajaratnam, N. (2016). “Air entrainment in a tall plunging dropshaft.” *Journal of Hydraulic Engineering*, 10.1061/(ASCE)HY.1943-7900.0001181, 04016038.

Malekpour, A., and Karney, B. W. (2016). “Spurious numerical oscillations in the Preissmann Slot Method: Origin and Suppression.” *Journal of Hydraulic Engineering*, 142(3): 04015060.

Mortensen, J. D., Barfuss, S. L., and Jhonson, M. C. (2011). "Scale effects of air entrainment by hydraulic jumps within closed conduits." *Journal of Hydraulic Research*, 49(1), 90-95.

Muller, K. Z., Wang, J., and Vasconcelos, J. G. (2017). "Water displacement in shafts and geysering created by uncontrolled air pocket releases." *Journal of Hydraulic Engineering*, 143(10): 04017043

Olson, D., Rajagopalan, S., and Corsi, R. L. (1997). "Ventilation of industrial process drains: Mechanisms and effects on VOC emissions." *Journal of Environmental Engineering*, 123(9): 939-947.

Parker, W. J., and Ryan, H. (2001). "A tracer study of headspace ventilation in a collector sewer." *Journal of the Air & Waste Management Association*, 51(4): 582-592.

Pescod, M. B. and Price, A. C. (1982). "Major factors in sewer ventilation." *Journal of Water Pollution Control Federation*, 54(4), 385-397.

Rajaratnam, N., Mainali, A., and Hsung, C. Y. (1997). "Observations of flow in vertical dropshafts in urban drainage systems." *Journal of Environmental Engineering*, 123(5): 486-491. 10.1061/(ASCE)0733-9372.

Shao (2013). "Two-dimensional hydrodynamic modelling of two-phase flow for understanding geyser phenomena in urban storm water system." *PhD thesis*, University of Kentucky, Lexington, Kentucky.

Song, C. C. S., Cardle, J. A., and Kim Sau, L. (1983). "Transient mixed flow models for storm sewers." *Journal of Hydraulic Engineering*, 109(11), 1487–1504.

Speerli, J., and Hager, W. H. (2000). "Air-water flow in bottom outlets." *Canadian Journal of Civil Engineering*, 27(3): 454-462.

Tullis, B., and Larchar, J. (2011). "Determining air demand for small- to medium-sized embankment dam low-level outlet works." *Journal of Irrigation and Drainage Engineering*, 137(12): 793-800.

U.S. Army Corps of Engineers (U.S. ACE) (1980). "Engineering and design: hydraulic design of reservoir outlet works." *Rep. EM1110-2-1602*. Washington, DC

U.S. Environmental Protection Agency (U.S. EPA) (1985). "Design manual: odor and corrosion control in sanitary sewerage systems and treatment plants." *Rep. epa/625/1-85/01*, Washington, DC.

Vasconcelos, J. G. and Marwell, D. T. B. (2011). "Innovative simulation of unsteady low-pressure flows in water mains." *Journal of Hydraulic Engineering*, 137(11): 1490-1499.

Vasconcelos, J. G., and Wright, S. J. (2005). "Experimental investigation of surges in a stormwater storage tunnel." *Journal of Hydraulic Engineering*, 131(10): 853-861.

Vasconcelos, J. G., and Wright, S. J. (2007). "Comparison between the two-component pressure approach and current transient flow solvers." *Journal of Hydraulic Research*, 45(2): 178-187.

Vasconcelos, J. G., and Wright, S. J. (2009). "Investigation of rapid filling of poorly ventilated stormwater storage tunnels." *Journal of Hydraulic Research*, 47(5): 547-558.

Vasconcelos, J. G., and Wright, S. J. (2011). "Geysering generated by large air pockets released through water-filled ventilation shafts." *Journal of Hydraulic Engineering*, 137(5): 543-555.

Vasconcelos, J. G., Wright, S. J., and Roe, P. L. (2006). "Improved simulation of flow regime transition in sewers: two-component pressure approach." *Journal of Hydraulic Engineering*, 132(6): 553-562.

Vasconcelos, J. G., Wright, S. J., and Roe, P. L. (2009). "Numerical oscillations in pipe-filling bore predictions by shock-capturing models." *Journal of Hydraulic Engineering*, 135(4): 296-305.

Vasconcelos, J. G., Klaver, P. R., and Lautenbach, D. J. (2015), "Flow regime transition simulation incorporating entrapped air pocket effects." *Urban Water Journal*, 12(6): 488-501.

Volkart, P. U., and Speerli, J. (1994). "Prototype investigation of the high velocity flow in the high head tunnel outlet of the Panix Dam." Proc. 18th ICOLD Congress, Durban, South Africa, Q. 71, R. 6, 55-78.

Wang, Y. C., Nobi, N., Nguyen, T., and Vorreiter, L. (2012). "A dynamic ventilation model for gravity sewer networks." *Water Science and Technology*, 65(1): 60-68.

Ward, M., Corsi, R., Morton, R., Knapp, T., Apgar, D., Quigley, C., Easter, C., Witherspoon, J., Pramanic, A., and Parker, W. (2011). "Characterization of natural ventilation in wastewater collection systems." *Water Environment Research*, 83(3): 265-273.

Ward, M., Hamer, G., McDonald, A., Witherspoon, J., Loh, E., and Parker, W. (2011). "A sewer ventilation model applying conservation of momentum." *Water Science and Technology*, 64(6): 1374-1382.

Wiggert, D. C. (1972). "Transient flow in free-surface, pressurized systems." *Journal of the Hydraulics Division*, 98(1): 11-27.

Wright, N. W. (2013). "Air vent sizing in low-level outlet works for small to medium-sized dams." MSc Thesis, Utah State University. Logan, Utah.

Wright, N. W., and Tullis, B. P. (2014). "Prototype and laboratory low-level outlet air demand comparison for small to medium-sized embankment dams." *Journal of Irrigation and Drainage Engineering*, 140(6): 04014013.

Wright, S. J., Lewis, J. W., and Vasconcelos, J. G. (2011a). “Geysering in rapidly filling storm-water tunnels.” *Journal of Hydraulic Engineering*, 137(1): 112-115.

Wright, S. J., Lewis, J. W., and Vasconcelos, J. G. (2011b). “Physical processes resulting in geysers in rapidly filling storm-water tunnels.” *Journal of Irrigation and Drainage Engineering*, 137(3): 192-202.

Wright, S. J., Vasconcelos, J. G., Creech, C. T., and Lewis, J. W. (2008). “Flow regime transition mechanisms in rapidly filling stormwater storage tunnels.” *Environmental Fluid Mechanics*, 8(5): 605-616.

Zhang, W. M., Liu, M. N., Zhu, D. Z., and Rajaratnam, N. (2014). “Mean and turbulent bubble velocities in free hydraulic jumps for small to intermediate Froude numbers.” *Journal of Hydraulic Engineering*, 140(11): 04014055. 10.1061/(ASCE)HY.1943-7900.0000924.

Zhang, W. M., Zhu, D. Z., Rajaratnam, N., Edwini-Bonsu, S., Fiala, J., and Pelz, W. (2016). “Use of air circulation pipes in deep dropshafts for reducing air induction into sanitary sewers.” *Journal of Environmental Engineering*, 142(4): 04015092. 10.1061/(ASCE)EE.1943-7870.0001046.

Zhou, F. (2000). “Effects of trapped air on flow transients in rapidly filling sewers.” *PhD thesis*, University of Alberta, Edmonton, Alberta.

Zhou, F., Hicks, F. E., and Steffler, P. (2004). “Analysis of effects of air pocket on hydraulic failure of urban drainage infrastructure.” *Canadian Journal of Civil Engineering*, 31: 86-94.

Zhou, F., Hicks, F. E., and Steffler, P. M. (2002). “Transient flow in a rapidly filling horizontal pipe containing trapped air.” *Journal of Hydraulic Engineering*, 128(6): 625-634.

Figure 2-1 Idealized air velocity contour due to the drag of wastewater. (Pescod and Price, 1982)

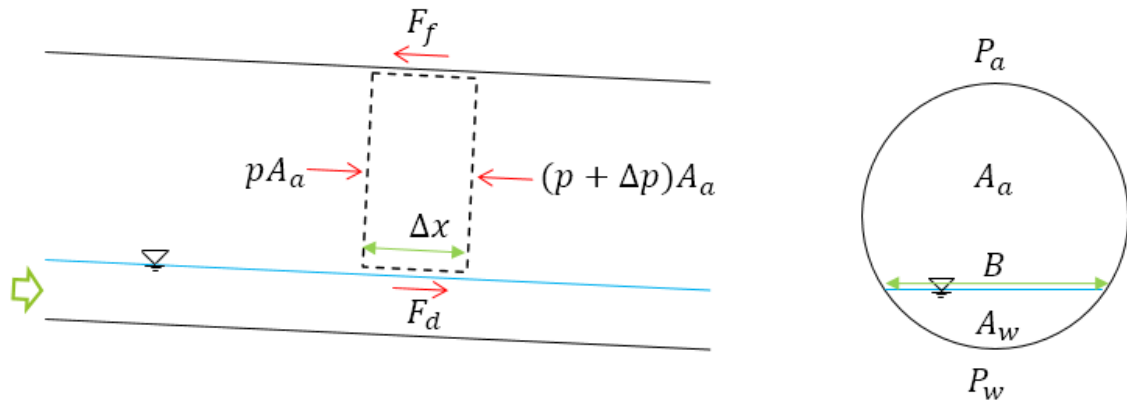


Figure 2-2 Schematic of the control volume for air flow calculation in a sewer pipe.

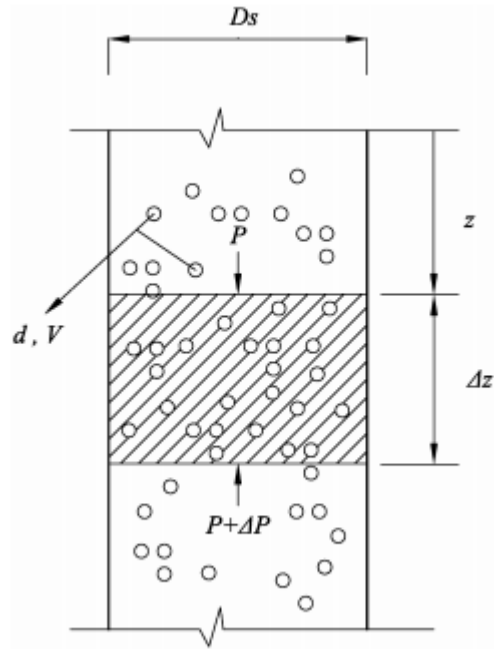


Figure 2-3 Schematic of the control volume for calculating air movement in a dropshaft. (Ma et al., 2016)

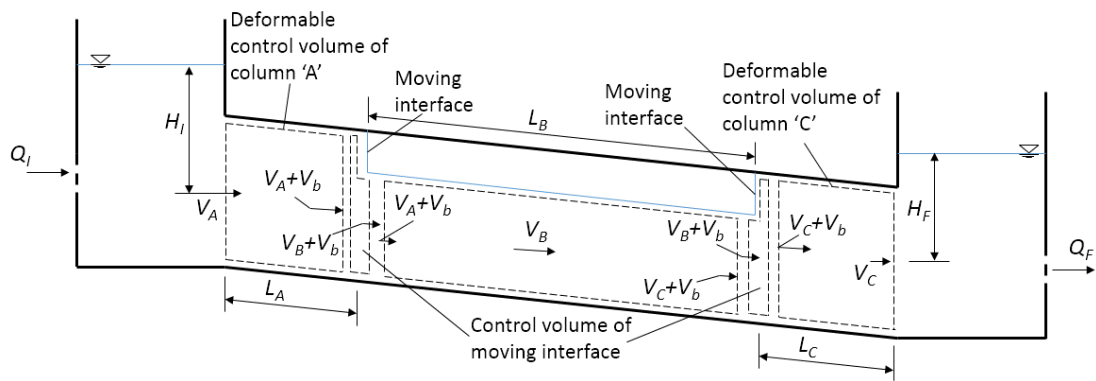


Figure 2-4 Schematic of the control volume for air pocket transportation in a pipe. (Li and McCorquodale, 1999)

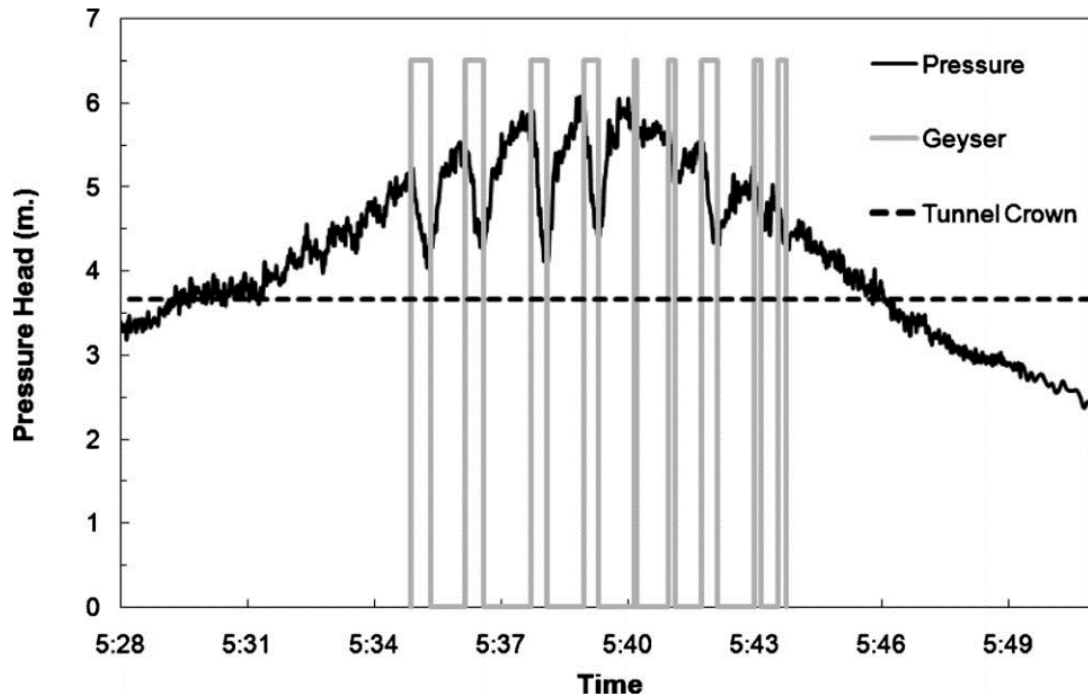


Figure 2-5 Sample pressure head during a series of geyser events. (Wright et al., 2011)

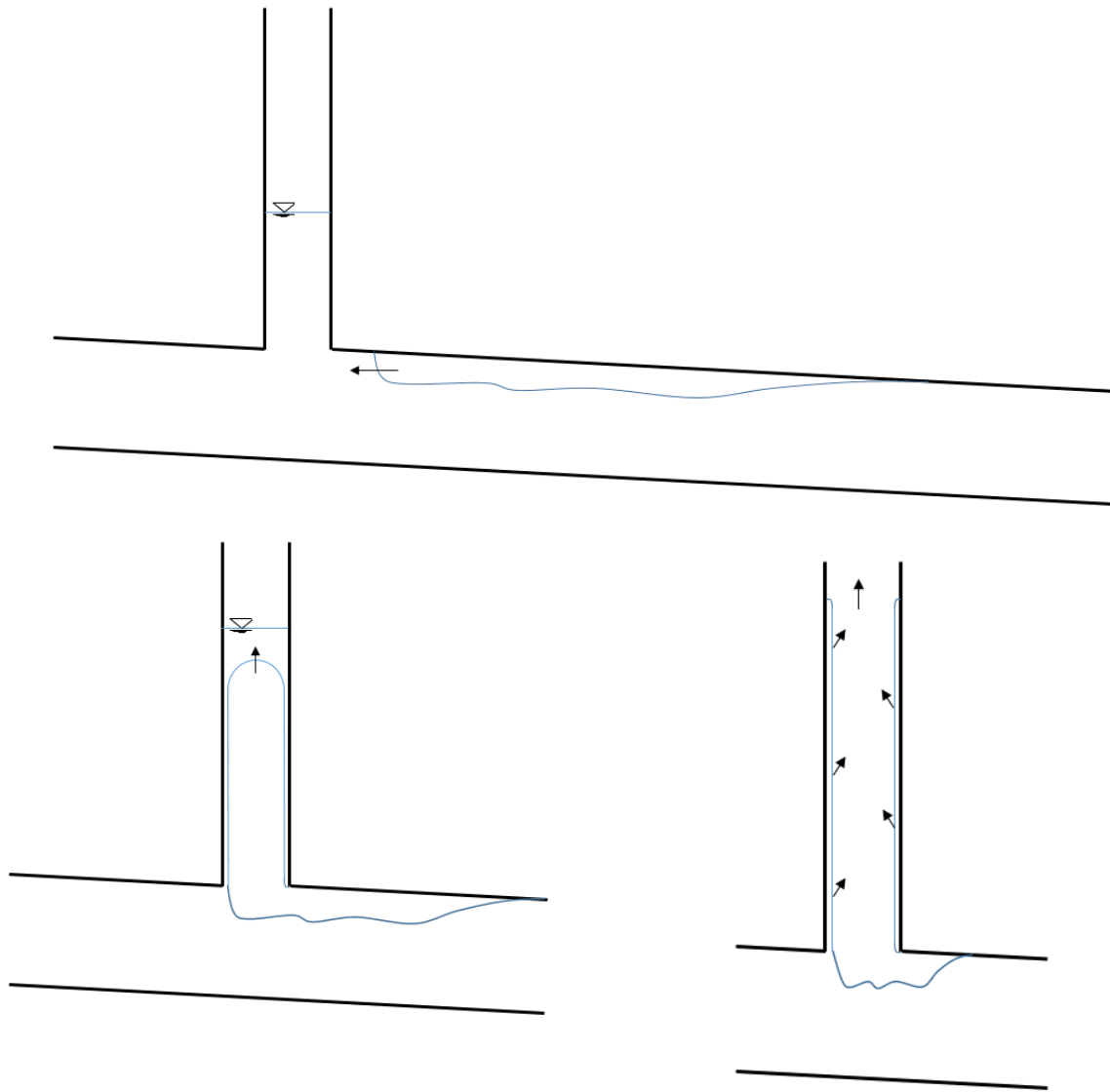


Figure 2-6 Schematic of the mechanism of geyser events. (Wright et al., 2011)

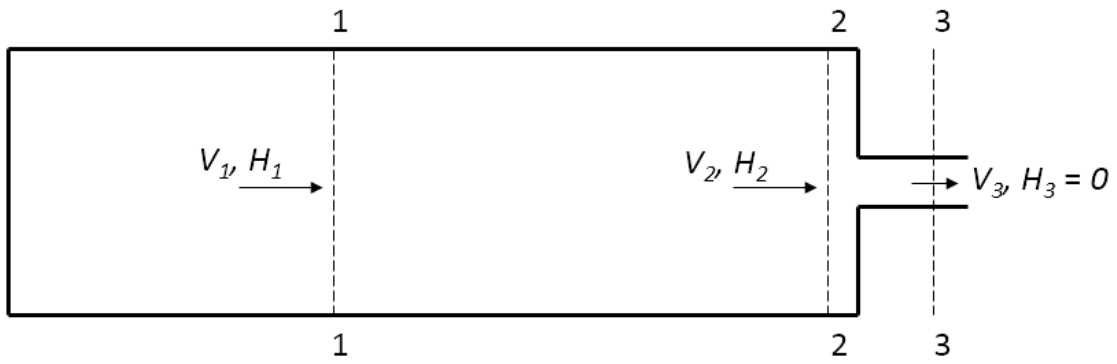


Figure 2-7 Schematic of the control volume on calculating the transient in a rapid filling pipe. (Zhou et al., 2002)

3. Air Movement Induced by Water Flow with a Hydraulic Jump in Changing Slope Pipes*

3.1. Introduction

Sewer pipes are generally designed for carrying liquid flow downstream without considering the air flow (Edwini-Bonsu and Steffler, 2004). Under anaerobic condition, hydrogen sulfide (H_2S) will be produced in the biofilm at the pipe wall and sediments. It is not only the main cause of sewer pipe corrosion but also an odor nuisance to the public (US EPA 1985). Therefore, an understanding of air movement in sewers is fundamental to guide the activity of sewer odor control (LA report, 2011). Certain drainage infrastructures such as dropshafts, inverted siphons, and changing slope pipes are expected to have a significant impact on the air movement in sewer systems due to the presence of air pressure in the pipe headspace (AE 2008; LA report, 2011; Zhang et al., 2016; Ma et al., 2016).

Pescod and Price (1982) experimentally examined the factors in sewer ventilation and reported that the pressure difference served as a primary factor in sewer ventilation while the liquid drag effect was secondary. However, no quantified relation between these two factors was proposed. Edwini-Bonsu and Steffler (2004) numerically studied the effect of water drag on air flow, whereas the combined effect of water drag and pressure gradient was studied by Edwini-Bonsu and Steffler (2006). Their models suggest that for laminar flow, the effects of water drag and pressure gradient

* The content of this chapter has been published as: Qian, Y., Zhu, D. Z., Zhang, W., Rajaratnam, N., Edwini-Bonsu, S., and Steffler, P. (2017). "Air Movement Induced by Water Flow with a Hydraulic Jump in Changing Slope Pipes." ASCE Journal of Hydraulic Engineering, 143(4): 10.1061/(ASCE)HY.1943-7900.0001252.

are additive, while not so in turbulent flow. Note that the water velocities in all these studies were relatively small (0.2 to 0.8 m/s), and a further study on higher water velocity is needed.

The air demand also needs to be considered in dam outlet work. U.S. ACE (1980) analyzed field measurement data and proposed an empirical equation for estimating the air flow demand. Larchar (2011), Tullis and Larchar (2011), Wright (2013), Wright and Tullis (2014) extensively studied the air demand in low-level outlet works. They measured the air demand under different flow scenarios. The ratio of air and water flow rates was found to be a function of filling ratio and had a maximum value of about 1.0. Volkart and Speerli (1994) measured the air demand in a high head dam and found that the air flow rate reached up to 50 times the water flow rate as the high-speed water became spray. Speerli and Hager (2000) observed the air flow in conduits and observed countercurrent air movement. However, the effect of pressure generated on air flow in the conduit was not assessed.

Hydraulic jumps in circular and rectangular open channels have been studied extensively, but mostly on understanding the liquid phase (e.g. Rajaratnam, 1965; Hager, 1992). Chanson et al. (1994, 2000, 2006, and 2008), and Zhang et al. (2014) conducted laboratory experiments on the bubble characteristics in hydraulic jumps in rectangular open channels. Kalinske and Robertson (1943) conducted experiments on the air entrainment in closed conduits, and proposed equations for the air entrainment rate due to hydraulic jumps. Escarameia (2007) summarized the existing data on closed conduits and reported that the air flow was lower than that of Kalinske and Robertson (1943). Mortensen et al. (2011) conducted experiments on the hydraulic jumps in circular pipes of different diameters and proposed a linear equation for the transportation of air

flow across hydraulic jumps. Note that these studies were all on conduit jumps where water filled the pipe after the jump and air was mainly transported in bubbly form. Given the fact that it is more common in sewers with headspace, it is necessary to study the air movement in pipes with hydraulic jumps with headspace. Edwini-Bonsu (2004) suggested that the hydraulic jump would generate a large amount of air flow due to the potential momentum transfer in the roller by the air/water bubbly flow, but a detailed analysis was not presented.

This research presents experimental and numerical studies on the air flow in a straight pipe and pipes with a hydraulic jump. The straight pipe model was used for assessing the combined effect of water drag and pressure gradient on air flow in sewer. The purpose of the hydraulic jump model was to measure the air flow rate induced by water flow with a hydraulic jump in pipes of changing slope. It was also used to explore the momentum transfer effect of a hydraulic jump on air flow. This study can be used to predict the air flow in a sewer pipe with known flow conditions, and thus useful in guiding activities in sewer odor control and pipe corrosion prevention.

3.2. Experimental design

The physical experiment of the air movement in changing slope pipes with a hydraulic jump was conducted in the T. Blench Hydraulic Lab at the University of Alberta. Figure 3-1 shows a schematic of the experimental apparatus. Two transparent Plexiglas pipes with an inner diameter of $D = 0.28$ m and a length of 2.0 m each were connected. The upstream pipe was set at an angle of $\theta = 10^\circ$ or 30° with the horizontal, while the downstream pipe was kept horizontal. A tailgate was used to control the downstream water level and the location of the hydraulic jump. Water was

supplied from a pump and the water discharge was measured by an electro-magnetic flow meter. A hole with a diameter of 10 cm was cut above the water inlet.

Table 3-1 provides a summary of the experimental conditions. Different downstream flow conditions as well as pipe slopes were examined. The downstream conditions were changed so that the air flow at the pipe outlet included free flow, partially restricted flow, or fully blocked flow. Exp. S1 was a numerical simulation of Exp. B1 at $Q_w = 6.5, 9.88, 13.58, \text{ and } 15.66$ L/s. The air flow rate, water depth upstream of the jump and the water flow rate were measured for $\theta = 30^\circ$ (Exp. A1). In addition to these measurements, air velocity and water surface profile in the center plane of the pipes were also measured for Exp. B1 for $Q_w = 9.88$ L/s.

A rotating vane anemometer (VelociCalc 5725, TSI Inc.) was mounted on the air inlet for measuring the air flow rate. An additional experiment was conducted for examining the measurement reliability. At the same air flow condition, the reading of the rotating vane anemometer was compared with the reading of two hotwire anemometers (HHF 42, Omega, Inc., and Velocicheck 8330, TSI Inc.). Over a total number of 22 readings, the rotating vane anemometer gave an air flow rate reading of 15.63 L/s with a standard deviation of ± 0.60 L/s. The air velocity was measured at 18 locations across the air vent, and the air flow rate through the air vent was estimated to 14.84 L/s by the hotwire. With a difference of 5%, the air flow rate measurement was considered reliable at the air vent.

The air velocity inside the pipe was visualized by dry ice mist created by mixing dry ice with water (Merzkirch, 1987) and captured using a high-speed camera (Phantom v211, Vision Research Inc.)

for a period of 3 minutes at 1000 frames/s. The local air velocities were obtained from the analysis of the videos, and each local velocity was an ensemble average of 15 velocity calculations. For the air velocity measurement inside the pipe, the nature of flow visualization limited the accuracy because the front of the mist was not as well defined sometimes and large discrepancies were expected. An averaged deviation of ± 0.28 m/s was observed with the measured air velocity ranging from 0.11 to 2.09 m/s. However, at this stage, there are no obviously better ways to conduct measurement due to the restriction of pipe walls and splashes of water drops in the pipe headspace. The water flow rate from the magnetic flow meter was checked with the traditional method of using a bucket and stopwatch, and the difference was less than 3%.

Two methods were used to measure the water flow depth in the pipes. Method (1) was by measuring the wetted perimeter of the pipe using a measuring tape accurate to 1 mm. The effect of the pipe wall thickness was corrected since the water level was curved upstream of the jump. Three readings were taken at the desired locations, 2 cm upstream and 2 cm downstream. This method was used to obtain the water depth for Froude number calculation. Method (2) involved a total of 7 small holes drilled on the pipe top. A wooden stick was inserted into one hole where the measurement was made, while other holes were kept sealed. The distance between the water surface and the pipe invert was the measured water depth. A comparison was made between these two methods 1 m downstream of the pipe joint for $Q_w = 9.88$ L/s. The direct measurement gave a reading of 19.5 cm, while the indirect method yielded a water depth of 19.7 cm. Therefore, these two methods compared well with each other and were considered reliable.

3.3. Numerical methods

Ansys CFX 14.0 was used for the numerical simulations. The geometry of the straight pipe and the hydraulic jump models are shown in Figure 3-2. The straight pipe model had a pipe diameter of 0.6 m, length of 10 m, and slope of 1.5%. For the hydraulic jump model, a box was added in front of the air inlet so that the atmospheric pressure specified on the box was far from the air inlet. Air boundaries were defined as opening at atmospheric pressure where air can move into or out of the domain. In Figure 3-2, the one-way arrows indicate water inlet or outlet boundary conditions. And the two-way arrows indicate “Opening” boundary conditions where air can either move into or out of the domain. Other boundaries of the pipes and box were set as no slip walls.

The Reynolds-Averaged Navier-Stokes (RANS) equation and the continuity equation can be written as (Ferziger and Peric, 2002):

$$\frac{\partial(\rho\bar{u}_i)}{\partial x_i} = 0 \quad (3-1)$$

$$\frac{\partial(\rho\bar{u}_i)}{\partial t} + \frac{\partial}{\partial x_j}(\rho\bar{u}_i\bar{u}_j + \rho\overline{u'_i u'_j}) = -\frac{\partial\bar{p}}{\partial x_i} + \frac{\partial\bar{\tau}_{ij}}{\partial x_j} \quad (3-2)$$

where x_i ($i = 1, 2, 3$) is the Cartesian coordinate; \bar{u}_i the mean velocity components; u'_i the fluctuating velocity component; ρ the density of fluid; t time; and $\bar{\tau}_{ij}$ the mean viscous stress tensor component; p the pressure.

For multi-phase flow modelling, the Volume of Fluid (VOF) method (Hirt and Nichols 1981) was used. This method introduces an additional variable α to present the volume fraction for each control volume. Its time-averaged governing equation is:

$$\frac{\partial\alpha}{\partial t} + u_i \frac{\partial\alpha}{\partial x_i} = 0 \quad (3-3)$$

For two-phase flow, $\alpha = 1$ represents that the control volume is completely filled with water, while $\alpha = 0$ means it is completely filled with air.

The κ - ω based Shear Stress Transport (SST) turbulence model was used. In free surface flows, a high velocity gradient at the interface between two fluids results in high turbulence generation. The turbulence damping effect at the free surface was considered by introducing an additional source term in the ω equation as (Egorov, 2004)

$$S_c = I\Delta n\delta\rho\left(\frac{E6\mu}{\delta\rho\Delta n^2}\right)^2 \quad (3-4)$$

where S_c is the source term added into ω equation; I the interfacial area density determined by the program; n the typical mesh size at interface; $\delta = 0.075$ the model constant; μ the viscosity of fluid; E the source coefficient.

Due to the air-water bubbly flow and the rough surface along the roller, the momentum transfer from water to air is enhanced by a hydraulic jump. Therefore, additional momentum flux on air flow was added in the hydraulic jump model because our preliminary experiment indicated that the numerical model was not able to model the momentum transfer between air and water flow along the roller. The strength of the additional momentum flux can be changed in the model to match measured flow rate (Ansys, 2011).

The node number and element size were determined based on a sensitivity analysis and on mesh independence. A series of meshes were generated by decreasing the node number by 1.3 times. Therefore, the node numbers tested were 2.70 million, 2.08 million, and 1.60 million. The model

became mesh independent at 2.70 million nodes where no significant improvement on water velocity profile was observed. The rest of the simulations was based on 2.70 million nodes.

3.4. Results and discussions

Mechanism of transportation of air in straight pipe model

Shown as Exp. C0 in Table 3-2, a straight pipe model of pipe diameter $D = 0.30$ m, zero slope and length of 6.0 m was firstly built according to Pescod and Price (1982). Air velocity profiles at different locations from the numerical model are plotted in Figure 3-3. The effect of mesh refinement (dash line) and turbulence damping (dot line) are studied at $x = 3.0$ m. The simulation with mesh refinement and turbulence damping at $x = 1.5, 3.0, 4.5$ m are shown in solid lines. Note that the comparison of air velocity profiles between the measured and simulated ones is only qualitative, and when the distance to the pipe inlet increases, the air velocity profile matches the experimental data better. In the above comparison, Pescod and Price (1982) did not provide the information of the pipe length and the location of their air velocity measurement.

The sensitivity of the turbulence damping was firstly analyzed. The air velocity profile at $x = 3.0$ m for the model without this damping was plotted as a dotted line in Figure 3-3. The inclusion of this damping substantially improved the simulated air velocity profile. Secondly, the mesh was locally refined at the air-water interface. The air velocity profile at $x = 3.0$ m without such refinement is plotted as dashed line, indicating that a mesh refinement would also improve the air velocity profile. However, further refinement would increase the node number exponentially and exceed the available computing power.

The simulated air flow rate was 10.12 L/s which was 38% higher than 7.33 L/s measured by of Pescod and Price (1982). In their study, the air flow rate was obtained by integrating the point velocity measurements which inherently had large uncertainties. And no detailed discussion on ambient pressure condition was provided in their study. In the numerical model, the momentum transferred from water to air was amplified due to the finite amount of mesh at the air-water interface. Therefore, large discrepancies was noticed, as expected. The coefficient E in Eq. (3-4) was determined at 150 and no more improvement was observed for a higher E value.

Further experimental conditions and simulation results are summarized in Table 3-2. For Exp. C1, the pipe exit pressure was fixed at atmospheric pressure while the pipe diameter and water flow rate were changed. For Exp. C2, the pipe exit pressure varied to study the effect of the pressure gradient inside the pipe. For Exp. C3, a single phase model was conducted where air flow was only driven by the pressure gradient. It was found that for the same pipe diameter, with the increase of water discharge, the Froude number (defined as: $Fr = V_w/(gh_e)^{0.5}$ where h_e is the hydraulic depth, V_w is averaged water velocity) decreases due to the increase of water depth, as shown in Table 3-2.

For Exp. C1, the ratio of air to water flow rates, β , decreases with the increase of the water flow rate. The ratio of the air to water velocity values, V_a/V_w , are plotted in Figure 3-4 with the study of Edwini-Bonsu and Steffler (2004) and Pescod and Price (1982). From the figure it can be seen that the V_a/V_w values for supercritical flow are substantially higher than published values. While for supercritical flow with lower Froude number and subcritical flow, the V_a/V_w are close to previous studies. As shown in Figure 3-5, even when the upstream inlet and downstream outlet were both

set at atmospheric pressure, a positive air pressure gradient was always generated in the pipe headspace, because the drag of water produces a negative pressure at the pipe inlet for air to move in. At the outlet, the pressure would be slightly higher than atmospheric pressure for air to move out so that the pressure increases from the inlet to the outlet. For example, for $D = 0.60$ m, and $Q_w = 40$ L/s, the averaged pressure gradient was 0.045 Pa/m.

With respect to Exp. C2, where the pressure at the pipe exit was above atmospheric pressure, most of the air flow rate decreased with the increase of the pipe exit pressure as stated in Table 3-2. If the pressure gradient was high enough, the air flow rate was negative. A typical air velocity contour under this condition is plotted in Figure 3-6. The maximum air velocity occurred at the water surface. The air velocity decreased with the vertical distance to the water surface. At the top of the cross-section, the air was moving opposite to the water flow due to the positive pressure gradient.

For Exp. C3, in which the air was purely driven by the pressure gradient, the effect of pressure gradient on the air flow is theoretically calculated using the energy equation. Considering a pipe of $D = 0.60$ m in diameter, 10 m length, filling ratio h/D (where h is the water depth) of 0.14, and a pressure gradient of 0.045 Pa/m, the air flow rate can be estimated at 300 L/s from energy equations, and the estimated air flow rate was 16.7% smaller than the simulated value of 350 L/s.

Associating with the control volume showed in Figure 3-1, assuming that the air and water velocities have uniform profiles, the force balance equation for a control volume is written as

$$\frac{1}{2} C_d \rho_w (V_w - V_a)^2 B \Delta x - \Delta p A_a \pm \frac{f}{8} \rho_a V_a^2 \Delta x P_a = 0 \quad (3-5)$$

where C_d is the drag coefficient; Δx the length of the control volume; B the water surface width; P_a the perimeter of headspace for air flow.

Looking at the balance of the first two terms in Eq. (3-5), the pressure gradient can be normalized with water depth and water velocity as $\frac{\Delta p}{\Delta x} \frac{D-h}{\rho_w V_w^2}$. The term C_d is obtained from the normalized pressure gradient and the filling ratio h/D . The relation of drag coefficient C_d with h/D and the normalised pressure gradient is fitted from software Origin 2016 (OriginLab Corporation, Version b9.3.226)

$$C_d = 230.3 \times \left(\frac{\Delta p}{\Delta x} \frac{D-h}{\rho_w V_w^2} \right)^{0.83} \times \left(\frac{h}{D} \right)^{3.23} + 5.2 \times 10^{-5} \quad (3-6)$$

with $R^2 = 0.98$. The value of C_d estimated from Eq. (3-6) is in the order of 10^{-4} ; thus the constant 5.2×10^{-5} is not ignorable. The drag coefficient between the air and water surfaces is commonly given as 0.0015 for wind force over a lake (Fischer et al., 1979). In a confined space such as in a pipe, the drag coefficient is expected to change given the unique air velocity profiles.

Hydraulic jump model: water surface profile and air velocity profile

The measured and simulated water surface profiles are plotted in Figure 3-7. The model was able to simulate the change in the water surface profile. The “bump” in the sloping pipe at $x \approx -1.0$ m was due to the sloshing of water from the circular water inlet. Similarly, the water surface change at the hydraulic jump was also predicted accurately by the numerical model.

Preliminary simulation suggests that the numerical model was not able to accurately model the extra momentum transfer between the air and water due to the rough surface and the bubbly flow at the roller of the hydraulic jump. While the momentum transfer from the hydraulic jump to the

air phase did not impact much on the water flow, it induces a pressure change that significantly affects the air flow given the small density of the air. Therefore, a momentum source term was incorporated on air flow in our numerical model. The momentum source term specified in the CFX code has a dimension of $[ML^{-2}T^{-2}]$ which meant momentum flux per unit volume (Ansys, 2011). In the hydraulic jump model, the source term was added to the pipe joint with a volume of 0.0015 m^3 . Therefore, the actual momentum flux added M_s is the amount added in the numerical model multiplied by the volume of 0.0015 m^3 . The measured air flow rate was used as a calibration quantity and the strength of the momentum source was adjusted accordingly. The air velocity profile and theoretically calculated pressure was used as a validation criteria.

The change of air flow rate with added M_s for $Q_w = 13.58 \text{ L/s}$ is plotted in Figure 3-8a. A clear growing trend of Q_a is observed, although the growth was small for a wide range of M_s . The M_s value was determined when the simulated air flow rate was within 10% of that measured in this case. As shown in Figure 3-8b, it was also found that for a higher water flow rate, a higher M_s value was needed to match the simulated air flow with experiment results. The M_s value increases rapidly if the water flow rate exceeds a certain value. It can be explained by the fact that higher water flow rate would generally produce a hydraulic jump with a higher Froude number which had rougher surface and more vigorous surface movement. Therefore, more momentum would be transferred to the air phase.

Air velocity profiles at sections 1.0 m, 0.5 m upstream of the pipe joint, and 1.0 m downstream of the pipe joint were measured in the pipe centre plane for Exp. B1 at $Q_w = 9.88 \text{ L/s}$, and these results were compared with those simulated in Figure 3-9. The error bars in the figure highlight the

uncertainties of air velocity measurement. The simulated air velocity profiles are overall in agreement with these measured with certain discrepancies. The discrepancies in Figure 3-9 mainly came from the chaotic form of air flow that was physically observed and the nature of air velocity measurement using flow visualization. In the upstream pipe, near the water surface, the water dragged the air flowing downstream, resulting in a positive air velocity. Close to the crown of the sloping pipe, negative air velocity was measured and simulated, due to the positive pressure gradient developed in the pipe headspace as shown in Figure 3-10. In the horizontal pipe, the air velocity were found positive from the water surface to the pipe top.

A theoretical estimation was made on the pressure at the air inlet to verify the pressure produced by our numerical model. Calculations are made at the air inlet, and the energy equation between far away from the air inlet and right inside the air inlet is:

$$\frac{p_{atm.}}{\rho_a g} = K_1 \frac{Q_a^2}{2g(0.25\pi D_a^2)^2} + \frac{p_1}{\rho_a g} \quad (3-7)$$

where D_a is the diameter of air vent; $K_1 = 1.0$ the minor loss coefficient at the air inlet; $p_{atm.}$ atmospheric pressure; p_1 pressure at inside of the air inlet. For Exp. S1, $Q_w = 9.88$ L/s, to have an air flow rate of 7.82 L/s, Eq. (3-7) yielded a pressure of -0.59 Pa which compared well with -0.58 Pa given by our numerical model.

The simulated cross-sectional air velocity contours are shown in Figure 3-11. At 1 m upstream of the pipe joint (Figure 3-11a) the air velocity contour was somehow symmetric to the center plane. In the pipe headspace near the water surface, a maximum air velocity was computed. In the upper region of the headspace, negative air flow was noted. At 0.5 m upstream of the pipe joint, a similar flow pattern was computed (Figure 3-11b) but the simulated air velocity distribution was

asymmetric due to the uneven distribution of the water surface obtained in the numerical model. The maximum simulated air velocity at this location was computed at the left bottom of the pipe headspace where water flowed downstream at a relatively high velocity. Reversed air flow was observed at the right bottom of the pipe and at the top of the pipe headspace. At 1 m downstream of the pipe joint, positive air velocity was found in the entire pipe headspace, and the highest air velocity was at the top right of the pipe headspace. The reason for the asymmetry distribution of air velocity was that the pressure upstream of the jump was not evenly distributed.

Hydraulic jump model: bulk air flow rate

The measured and simulated air flow rates and β values are presented in Figure 3-12 with water discharge and the Froude number in the upstream pipe. The air flow rate was used as a calibration criteria in the hydraulic jump numerical model as mentioned previously. The air flow rate increases with the water flow rate. The trend of air and water flow rate in Figure 3-12a is in good agreement for Exp. A1 and B1, suggesting that the effect of θ on β is relatively small. The air flow rate in Exp. B4 shows a slightly faster growth rate with the water flow rate due to the fact that there was no sudden reduction of headspace. The air flow rate for conduit jump (Exp. B3) was lower than other cases because the air was mainly transported in the forms of bubbles and air pockets, while headspace existed for air movement in other cases (except for Exp. B2). The Exp. B3 was similar to most of the previous studies (Kalinske and Robertson, 1943; Mortensen et al., 2011; and Escarameia, 2007). Finally, no air was transported in Exp. B2 where the tailgate was closed from top and with no headspace.

In Figure 3-12b, most of the present β values were found to be substantially higher than the published values in which the roller of the hydraulic jump filled the pipe and the flow became a conduit jump. Due to the blockage of headspace, the transportation of bubbles induced by hydraulic jump was the dominant mechanism of air transportation. Therefore their β values were lower than those in the present study in which headspace existed and air moved freely from upstream to downstream. In Exp. B3, a conduit jump was created and the β value was found to be fairly close to the published values (Figure 3-12b).

The method proposed previously from the straight pipe model can be used to estimate the air flow in the sloping pipe. Considering Exp. B1 and a water flow rate of 9.88 L/s, the numerical model suggests a filling ratio of 0.11, an averaged water velocity of 2.33 m/s, and a pressure gradient of around 0.52 Pa/m. Equation 3-6 yields a drag coefficient of 7.9×10^{-5} . From Equation 3-5, a critical pressure gradient is calculated to be 0.64 Pa/m. Therefore, the air is flowing at the same direction as the water flow. Solving for Equation 3-5 gives the averaged air velocity $V_a = 0.20$ m/s, which results in an air flow rate of 11.60 L/s or about 27% higher than the measured value. Given that the air flow rate is sensitive to the pressure changes and thus a small pressure change may lead to a dramatic change on air flow rate. This accuracy is acceptable.

The effect of the length of the pipe and the diameter of air opening for the hydraulic jump model were studied with a pipe length of 3 m and 4 m and with a larger air inlet for a water flow rate of 9.88 L/s. It was found that when the diameter of the air vent area increased from 10 cm to 15 cm, the air flow rate was 8.2 L/s. The increasing of air flow rate was 7.8% when the area of air vent increased by 2.25 times. Therefore, the diameter of air vent did not significantly restrict the air

flow. For the pipe length of 3 m and 4 m, air flow rate was found to be 7.6 L/s and 7.1 L/s respectively. The change was not significant compared with the one from our original model. The water surface for all three cases was found to be similar. Therefore, pipe length did not significantly impact on air flow.

3.5. Conclusions

Three-dimensional, multiphase numerical models were built to study the effect of water drag and pressure gradient on air flow in partially filled sewer pipes. The straight pipe model suggested that for a circular pipe with the inlet and outlet open to the atmosphere, an air pressure gradient was automatically generated in the pipe. Positive pressure gradient reduces the air flow rate. If the pressure gradient is high enough, the air can move at the opposite direction of the water flow. For the air flow affected by both water drag and pressure gradient, the drag coefficient was found to be a function of filling ratio and normalized pressure gradient. A general method was proposed to predict the air flow rate in a straight sewer pipe with known flow conditions. This work provides a way for predicting the air flow in a certain sewer network given the upstream and downstream pressure and wastewater flow conditions. It is noted that for sewer networks, the pressure in pipes are not necessarily atmospheric. With the proposed method, one can estimate the air flow condition (e.g., air flow rate and flow direction) in sewer systems and therefore have a general understanding of the odor transportation in such a system.

The hydraulic jump model was focused on a more complex flow regime. The momentum transfer of a hydraulic jump on air flow was proposed from the hydraulic jump model. For the hydraulic jump experiment and numerical model, when a hydraulic jump existed the air flow rate was larger

than published values and the ratio of air to water flow rates β was in the order of 1.0 when downstream pipe was not full. By forming a hydraulic jump with a Froude number large enough to partially ‘seal’ the head space, the air flow rate was found to decrease and approach published values. No air was transported if the tailgate was closed from top leaving no headspace downstream of the jump. The proposed method from straight pipe model also works well with the hydraulic jump model. The additional momentum flux caused by the roller of a hydraulic jump on air flow was discussed. It was found that the numerical model was not able to accurately simulate the air flow induced by a hydraulic jump without adding additional momentum sources in the model. The strength of this momentum flux source increases with the increase of water flow. The detailed mechanism and quantified relationship were not discussed in present study.

Acknowledgements

The authors gratefully appreciate the financial support from China Scholarship Council (CSC), the City of Edmonton, and the Natural Sciences and Engineering Research Council (NSERC) of Canada. The authors also would like to thank Perry Fedun for his technical assistance.

List of symbols

A_a : Headspace area

B : Width of water surface

C_d : Non-dimensional drag coefficient

D : Pipe diameter

D_a : Diameter of air vent

E : Source coefficient

F : Froude number

I : Interfacial area density

K_l : Minor loss coefficient

L : Pipe length

M_s : Momentum added in the numerical model

P_a : Perimeter of headspace

Q_a : Air flow rate

Q_w : Water flow rate

S_c : Source term added into the ω function

V_a : Averaged air velocity

V_w : Averaged water velocity

f : Darcy-Weisbach friction coefficient

g : Acceleration due to gravity

h : Water depth

h_e : Hydraulic depth

p : Pressure

$p_{atm.}$: Atmospheric pressure

p_{exit} : Pressure at pipe exit

t : Time

u_a : Local air velocity

\bar{u}_i : Mean velocity components

u'_i : Fluctuating velocity components

x_i ($i = 1, 2, 3$): Cartesian coordinates

n : Typical mesh size at interface

x : Length of control volume

y : Vertical coordinate

α : Volume fraction of fluid

β : Ratio of air flow rate and water flow rate

δ : Model constant 0.075

θ : Angle between pipes

μ : Viscosity of fluid

ρ : Density of fluid

ρ_a : Density of air

ρ_w : Density of water

$\bar{\tau}_{ij}$: Mean viscous stress tensor components

References

Ansys (2011). “ANSYS CFX Guide.” Release 14.0.

Associate Engineering (AE) (2008). “Odor control program report.” for the City of Edmonton, Alberta, Canada.

Chanson, H. (2006). “Air bubble entrainment in hydraulic jumps, similitude and scale effects.” *Research Report No. CE57/05*, Department of Civil Engineering, The University of Queensland.

Chanson, H. and Brattberg, T. (2000). “Experimental study of the air-water shear flow in a hydraulic jump.” *International Journal of Multiphase Flow*, 26(4), 583-607.

Chanson, H. and Gualtieri, C. (2008). “Similitude and scale effects of air entrainment in hydraulic jumps.” *Journal of Hydraulic Research*, 46(1), 35-44.

Chanson, H. and Qiao, G. L. (1994). “Air bubble entrainment and gas transfer at hydraulic jumps.” *Research Report No. CE149*, Department of Civil Engineering, The University of Queensland.

Edwini-Bonsu, S. (2004). “Air flow in sanitary sewer systems: a physically-based approach.” PhD Thesis, University of Alberta, Canada

Edwini-Bonsu, S., and Steffler, P. M. (2004). “Air flow in sanitary sewer conduits due to wastewater drag: a computational fluid dynamics approach.” *Journal of Environmental Engineering Science*, 3(5): 331-342.

Edwini-Bonsu, S., and Steffler, P. M. (2006). “Dynamics of air flow in sewer conduit headspace.” *Journal of Hydraulic Engineering*, 132(8): 791-799. 10.1061/(ASCE)0733-9429.

Egorov, Y. (2004). “Contact condensation in stratified stream-water flow.” *Technical Report*, EVOL-ECORA-D 07. <<https://domino.grs.de/ecora/ecora.nsf/>> (Apr. 09, 2016)

Escarameia, M. (2007). "Investigating hydraulic removal of air from water pipelines." *Water Management*, 160(1): 25-34.

Ferziger, J. H. and Peric, M. (2002). "*Computational Methods for Fluid Dynamics.*" 3rd edition, Springer-Verlag, Berlin.

Fischer, H. B., List, E. J., Koh, R. C. Y., Imberger, J., and Brooks, N. H. (1979). "*Mixing in inland and coastal waters.*" Academic Press, San Diego.

Hager, W. H. (1992). "*Energy dissipators and hydraulic jump.*" Kluwer Academic Publishers: Dordrecht.

Hirt, C. W. and Nichols, B. D. (1981). "Volume of fluid (VOF) method for the dynamics of free boundaries." *Journal of Computational Physics*, 39(1), 201-225.

Kalinske, A. A. and Robertson, J. M. (1943). "Closed conduit flow." *Transactions, ASCE*, 108, 1435-1447.

LA report (2011). "Waste odor control master plan." Wastewater Engineering Services Division, Bureau of Sanitation. <
http://www.lacitysan.org/lasewers/sewers/odors/pdf/Odor_Master_Plan_2011.pdf> (Jan. 11, 2016)

Larchar, J. A. (2011). "*Air demand in low-level outlet works.*" MSc Thesis, Utah State University.

Lowe, N. J., Hotchkiss, R. H., and Nelson, E. J. (2011). "Theoretical determination of sequent depths in closed conduits." *Journal of Irrigation and Drainage Engineering*, 137(12): 801-810. 10.1061/(ASCE)IR.1943-4774.0000349.

Ma, Y., Zhu, D. Z., and Rajaratnam, N. (2016). "Air entrainment in a tall plunging dropshaft." *Journal of Hydraulic Engineering, ASCE*, 142(10): 04016038.

Merzkirch, W. (1987). *Flow visualization.* 2nd Edition. Academic Press, Orlando.

Mortensen, J. D., Barfuss, S. L., and Jhonson, M. C. (2011). "Scale effects of air entrainment by hydraulic jumps within closed conduits." *Journal of Hydraulic Research*, 49(1), 90-95.

Pescod, M. B. and Price, A. C. (1982). "Major factors in sewer ventilation." *Journal of Water Pollution Control Federation*, 54(4), 385-397.

Rajaratnam, N. (1965). "Hydraulic jump in horizontal conduit." *Water Power*, 17: 80-83.

Speerli, J., and Hager, W. H. (2000). "Air-water flow in bottom outlets." *Canadian Journal of Civil Engineering*, 27(3): 454-462.

Tullis, B., and Larchar, J. (2011). "Determining air demand for small- to medium-sized embankment dam low-level outlet works." *Journal of Irrigation and Drainage Engineering*, 137(12): 793-800. 10.1061/(ASCE)IR.1943-4774.0000345.

U.S. Army Corps of Engineers (US ACE) (1980). "Engineering and design: hydraulic design of reservoir outlet works." *Rep.* EM1110-2-1602. Washington, DC

U.S. Environmental Protection Agency (US EPA) (1985). "Design manual: odor and corrosion control in sanitary sewerage systems and treatment plants." *Rep.* epa/625/1-85/01, Washington, DC.

Volkart, P. U., and Speerli, J. (1994). "Prototype investigation of the high velocity flow in the high head tunnel outlet of the Panix Dam." *Proc. 18th ICOLD Congress*, Durban, South Africa, Q. 71, R. 6, 55-78.

Wright, N. W. (2013). *"Air vent sizing in low-level outlet works for small to medium-sized dams."* MSc Thesis, Utah State University. Logan, Utah.

Wright, N. W., and Tullis, B. P. (2014). "Prototype and laboratory low-level outlet air demand comparison for small to medium-sized embankment dams." *Journal of Irrigation and Drainage Engineering*, 140(6): 04014013. 10.1061/(ASCE)IR.1943-4774.0000712.

Zhang, W. M., Liu, M. N., Zhu, D. Z., and Rajaratnam, N. (2014). "Mean and turbulent bubble velocities in free hydraulic jumps for small to intermediate Froude numbers." *Journal of Hydraulic Engineering*, 140(11): 04014055. 10.1061/(ASCE)HY.1943-7900.0000924.

Zhang, W. M., Zhu, D. Z., Rajaratnam, N., Edwini-Bonsu, S., Fiala, J., and Pelz, W. (2016). "Use of air circulation pipes in deep dropshafts for reducing air induction into sanitary sewers." *Journal of Environmental Engineering*, 142(4): 04015092. 10.1061/(ASCE)EE.1943-7870.0001046.

Table 3-1 Summary of experiments. (A: angle $\theta = 30^\circ$; B: $\theta = 10^\circ$)

Exp.	Q_w (L/s)	Downstream condition
A1	6.50 - 13.58	Hydraulic jump with headspace
B1	6.50 - 15.66	
B2	9.90	Hydraulic jump with no headspace
B3	15.84	Conduit jump
B4	5.01 - 15.00	Tailgate fully open, supercritical flow
S1	6.50 – 15.66	Numerical simulation for Exp. B1

Table 3-2 Numerical experiment list for straight pipe model and results.

Exp.	Specified values		Values obtained and calculated from the model						
	Q_w (L/s)	p_{exit} (Pa)	h/D	V_w (m/s)	F	dp/dx (Pa/m)	Q_a (L/s)	β	V_a/V_w
C0	21.21	0	0.50	0.6	0.56	N/A	10.12	0.48	0.48
C1	20	0	0.10	1.30	2.20	0.058	197.09	9.85	0.57
	40		0.14	1.53	2.01	0.045	173.78	4.34	0.44
	80		0.22	1.78	1.89	0.088	205.12	2.56	0.49
	160		0.32	2.08	1.71	0.055	136.23	0.85	0.33
C2	20	1	0.10	1.30	2.20	0.066	21.52	1.076	0.070
		5				0.32	-107.36	-5.37	-0.30
		7				0.45	-143.24	-7.162	-0.40
	40	1	0.14	1.53	2.01	0.137	158.97	3.97	0.41
		5				0.471	59.45	1.49	0.16
		7				0.613	18.41	0.46	0.057
	80	1	0.22	1.78	1.89	0.347	288.91	3.61	0.68
		5				0.623	234.40	2.93	0.56
		7				0.784	209.47	2.62	0.058
C3	N/A	N/A	0.14	N/A	N/A	0.045	350.71	N/A	N/A

C0: For model validating, $D = 0.30$ m, $L = 6.0$ m, pipe slope = 0.0%.

C1 – C3: $D = 0.60$ m, $L = 10.0$ m, pipe slope = 1.5%.

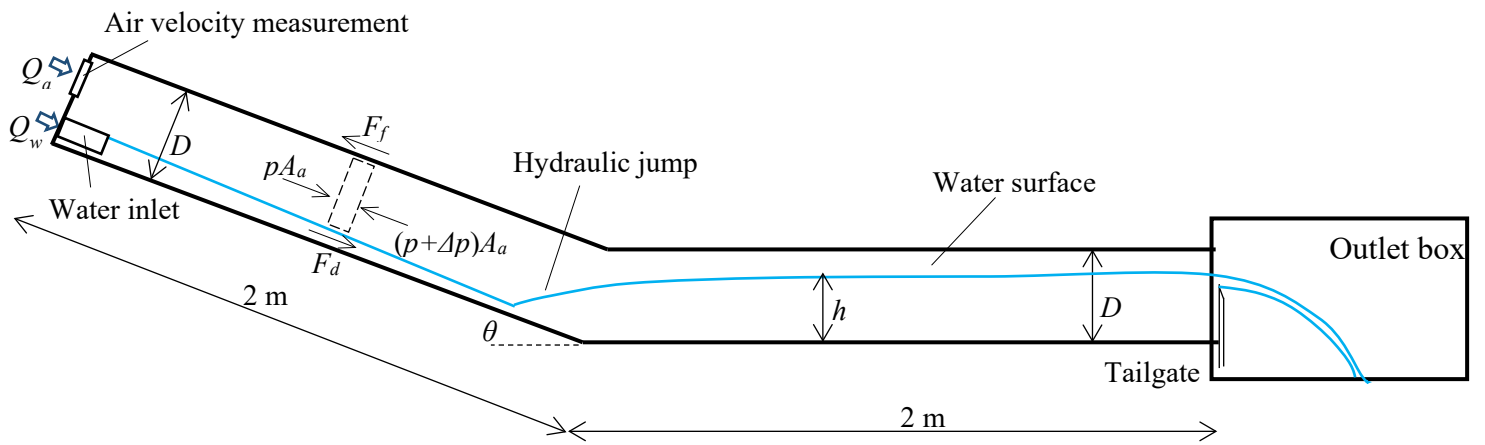


Figure 3-1 Schematic of experimental apparatus showing sloping and horizontal pipes.

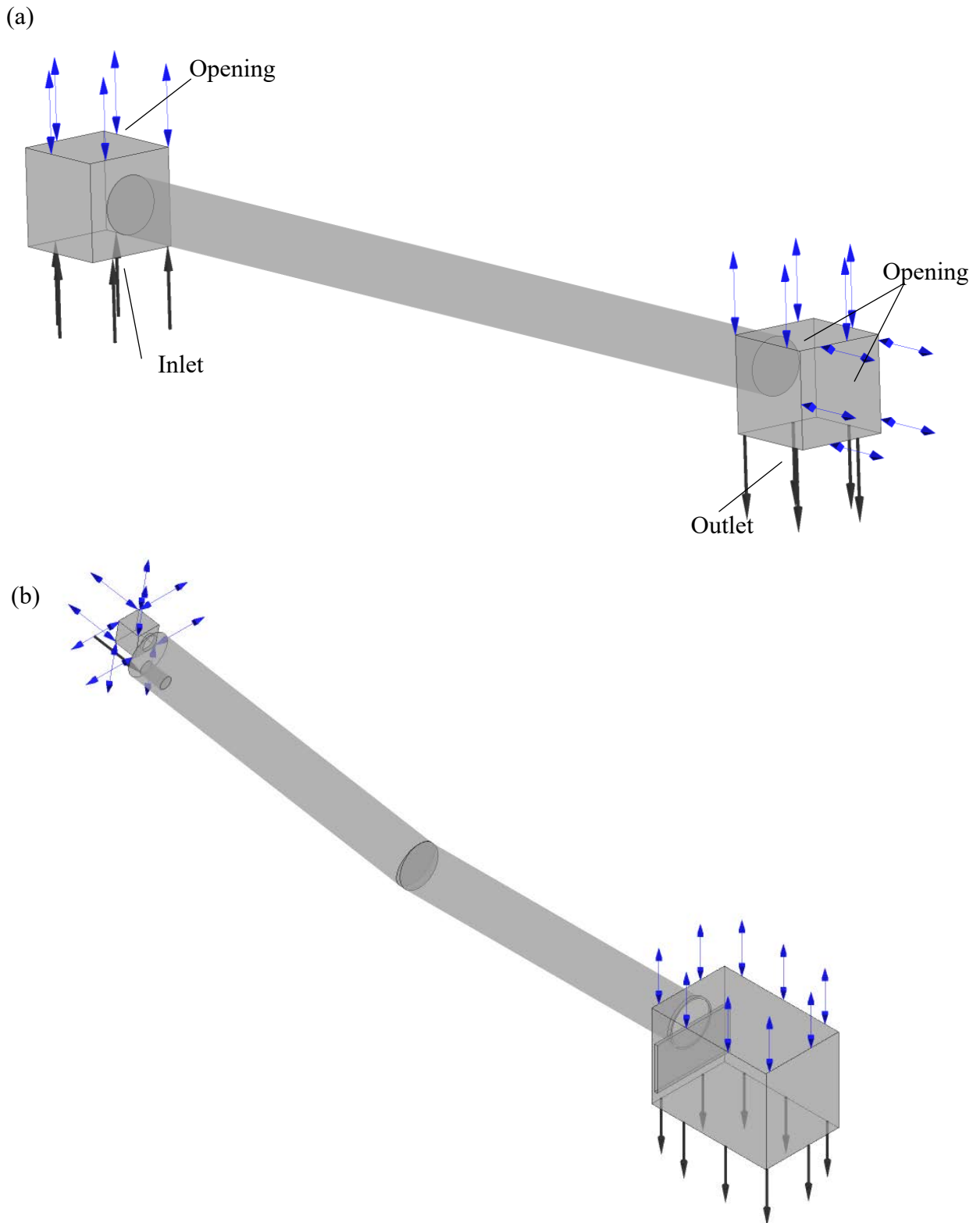


Figure 3-2 Geometry and boundary conditions of numerical models. (a) straight pipe model; (b) hydraulic jump model.

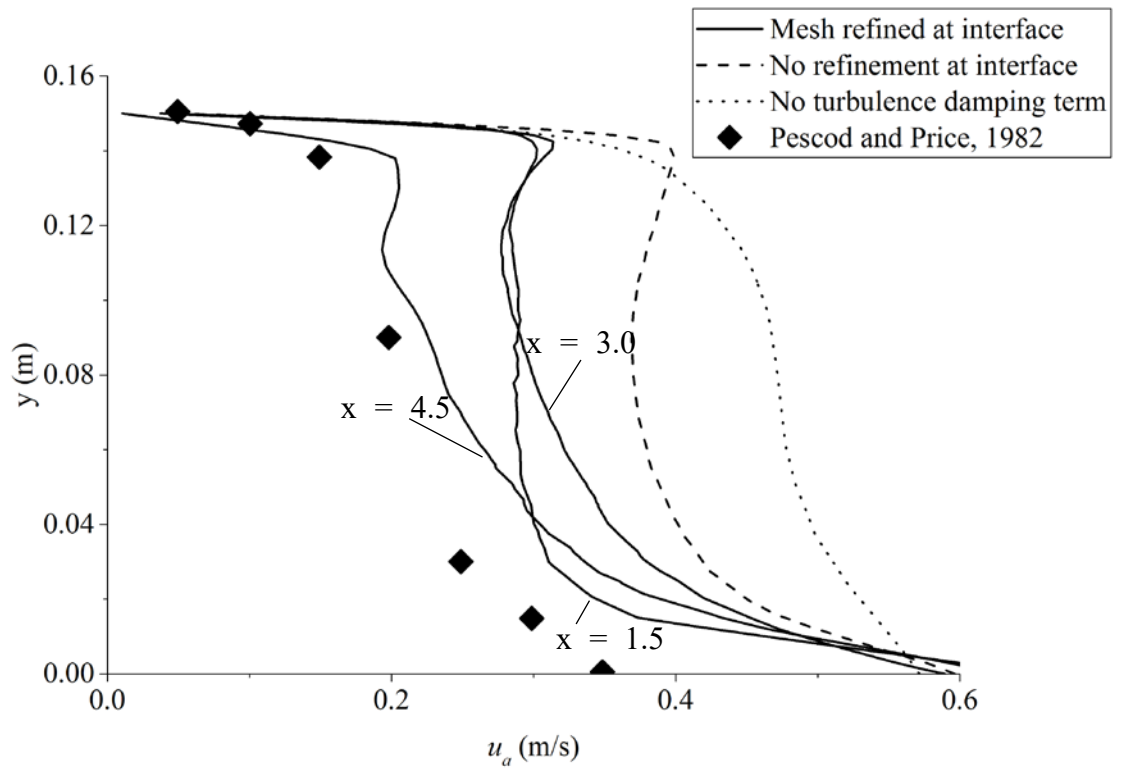


Figure 3-3 Comparison of simulated air velocity profiles at pipe center plane with Pescod and Price (1982).

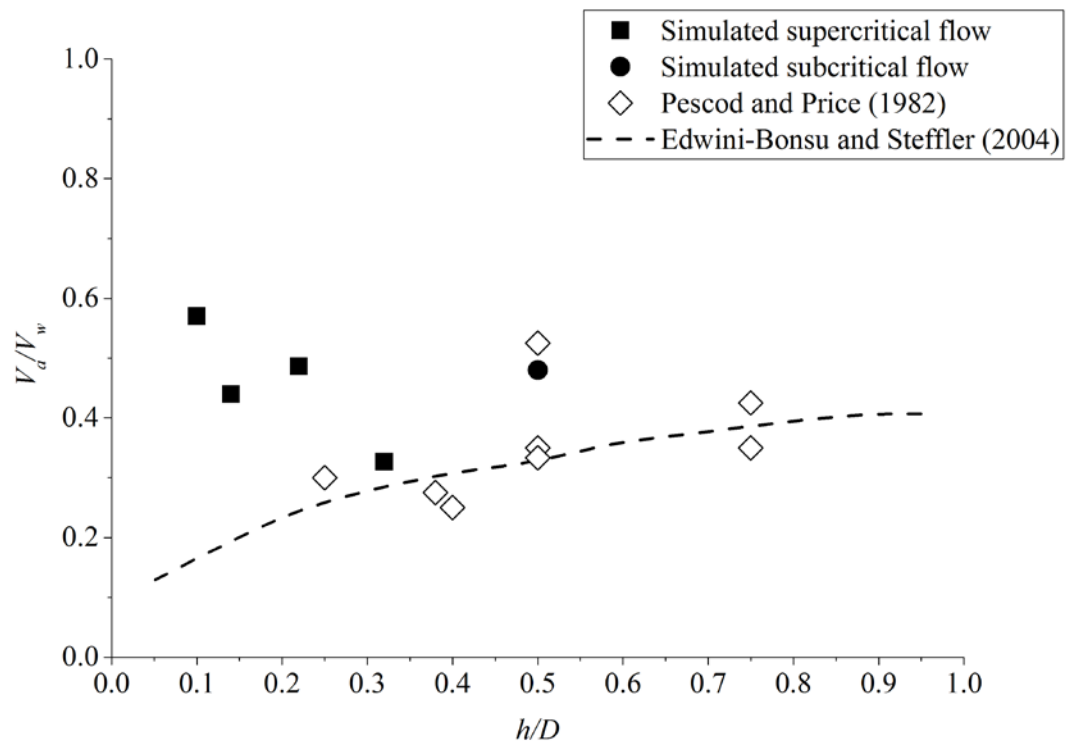


Figure 3-4 Plot of the air and water velocity ratio with filling ratio for Exp. C0 and C1.

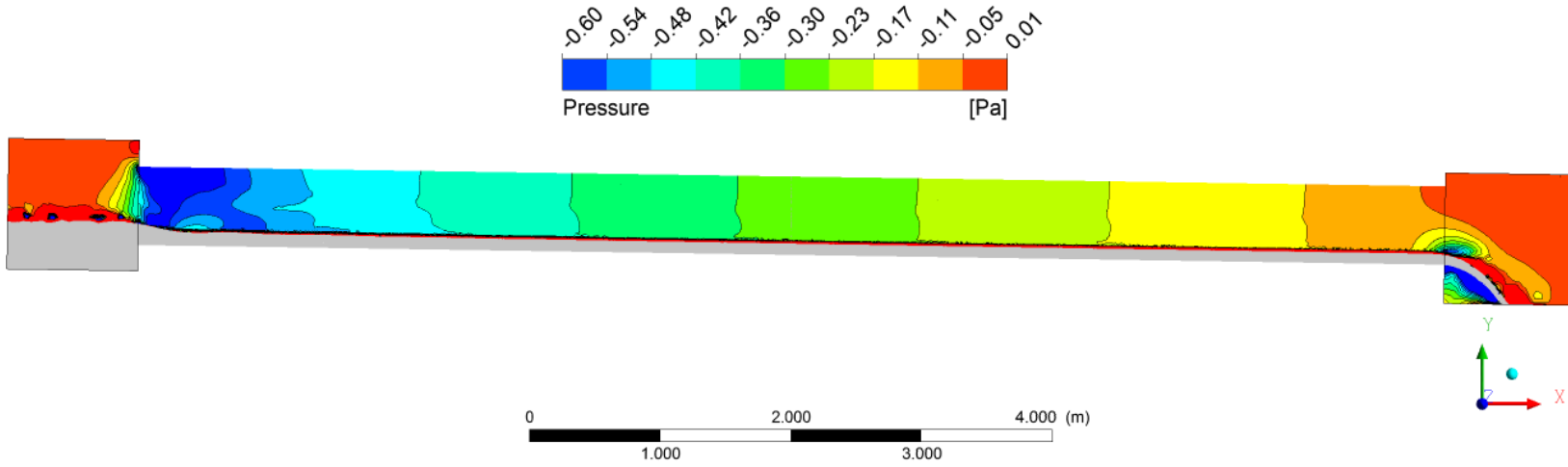


Figure 3-5 Typical pressure distribution in straight pipe model for $D = 60$ cm, $Q_w = 40$ L/s, $p_{exit} = 0$ Pa, $L = 10$ m.

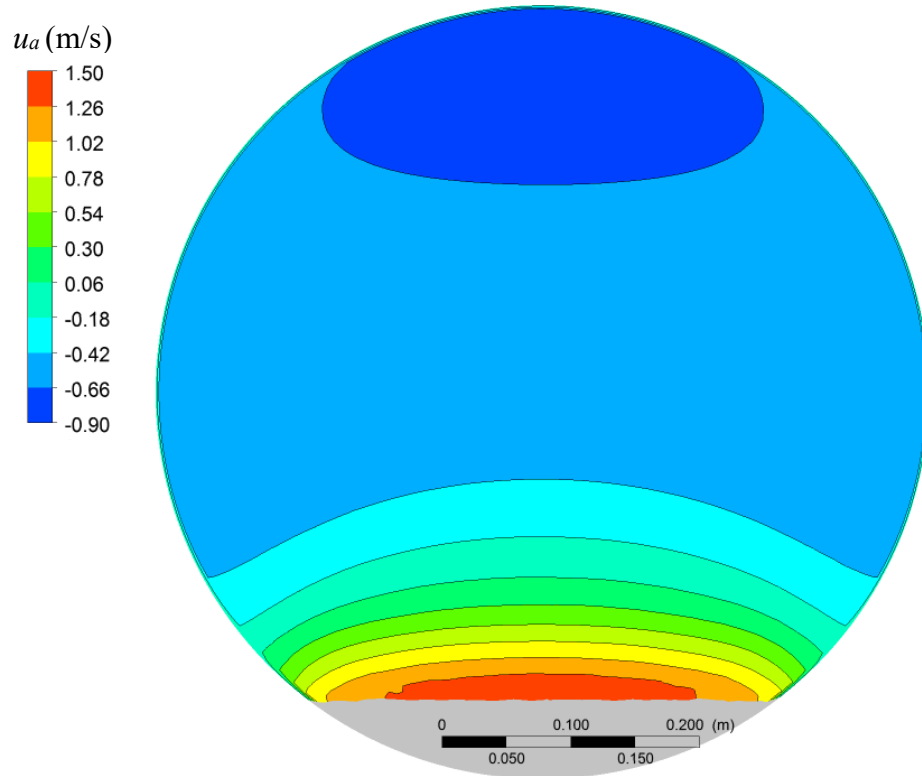


Figure 3-6 Typical velocity contour at pipe location of $x = 5$ m showing reversed air flow at top; $D = 0.60$ m, $Q_w = 20$ L/s, $p_{exit} = 5$ Pa.

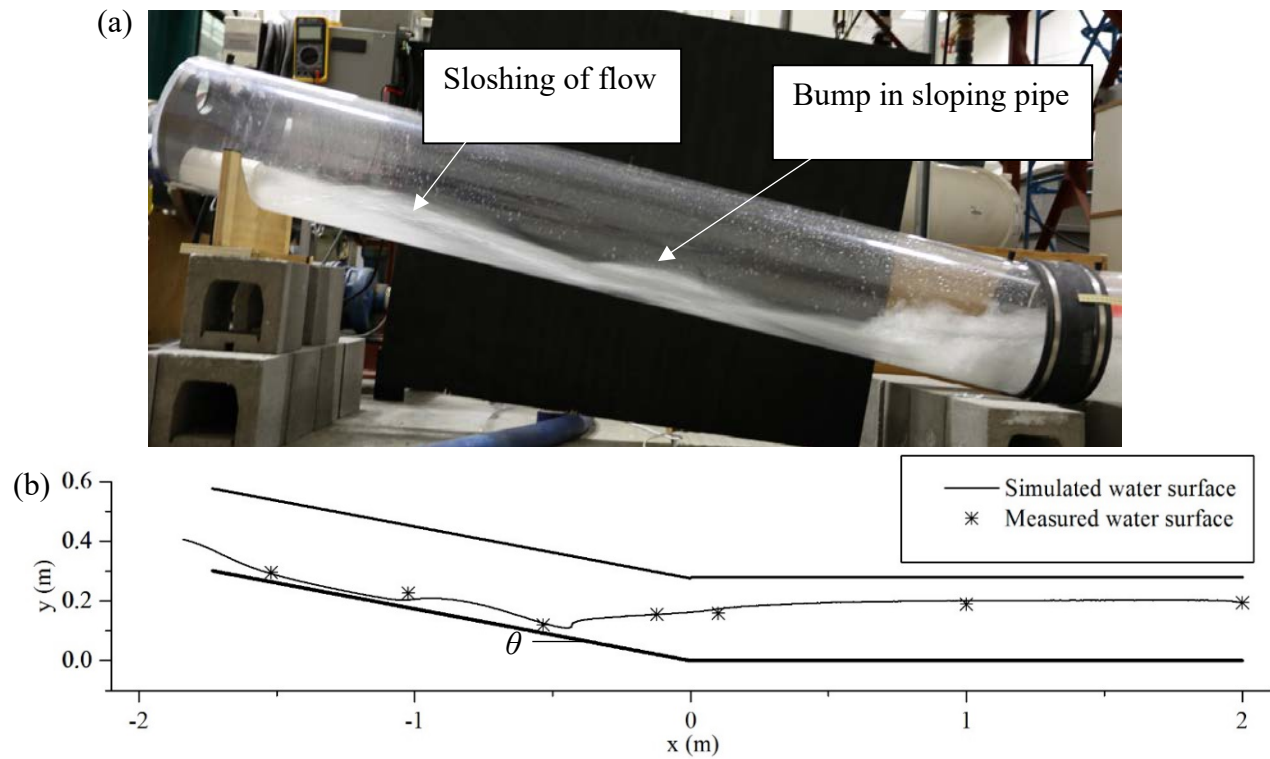


Figure 3-7 Comparison between measured and simulated water surfaces for $Q_w = 9.88$ L/s, $\theta = 10^\circ$. (a) Photo of water surface in sloping pipe; (b) Measured and simulated water surfaces.

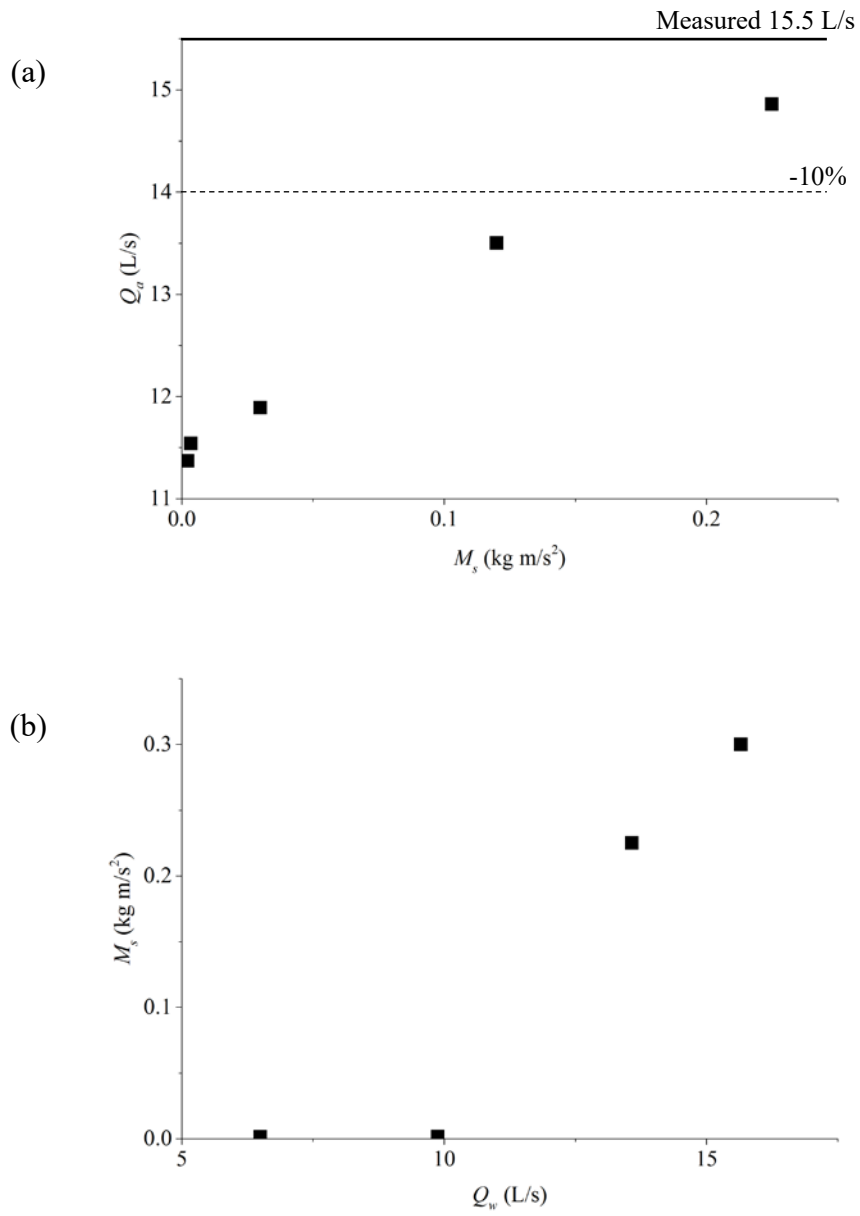
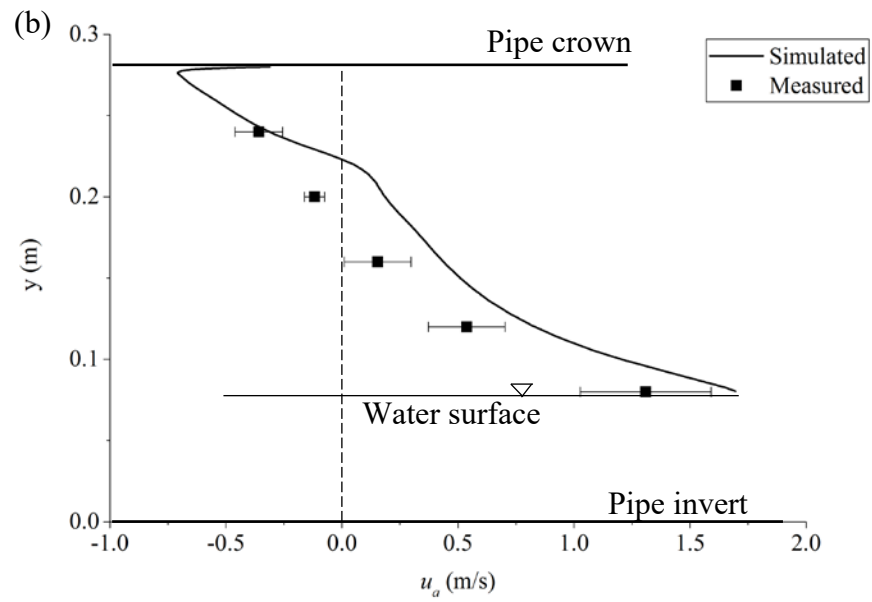
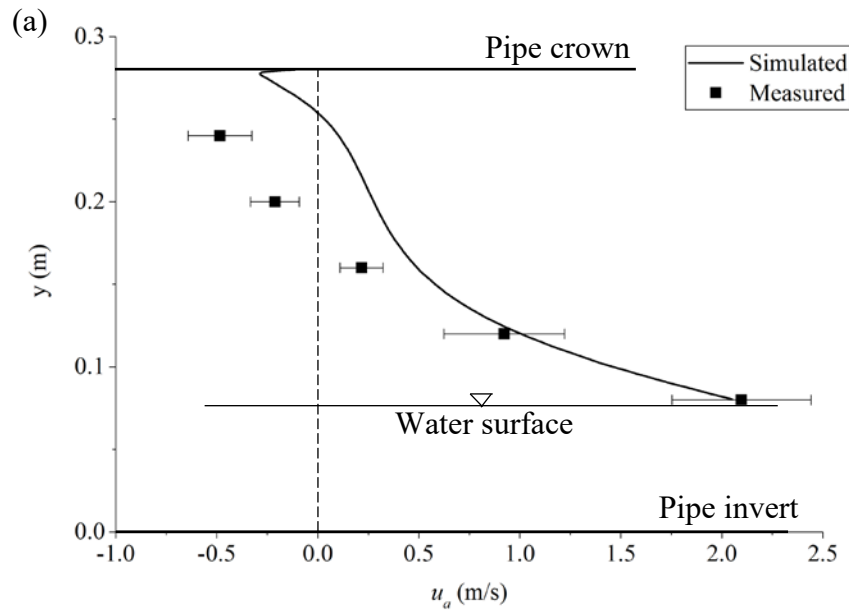


Figure 3-8 Plot of additional momentum source induced by the hydraulic jump. (a) Change of air flow rate with different M_s values for $Q_w = 13.58$ L/s; (b) Different M_s values versus Q_w .



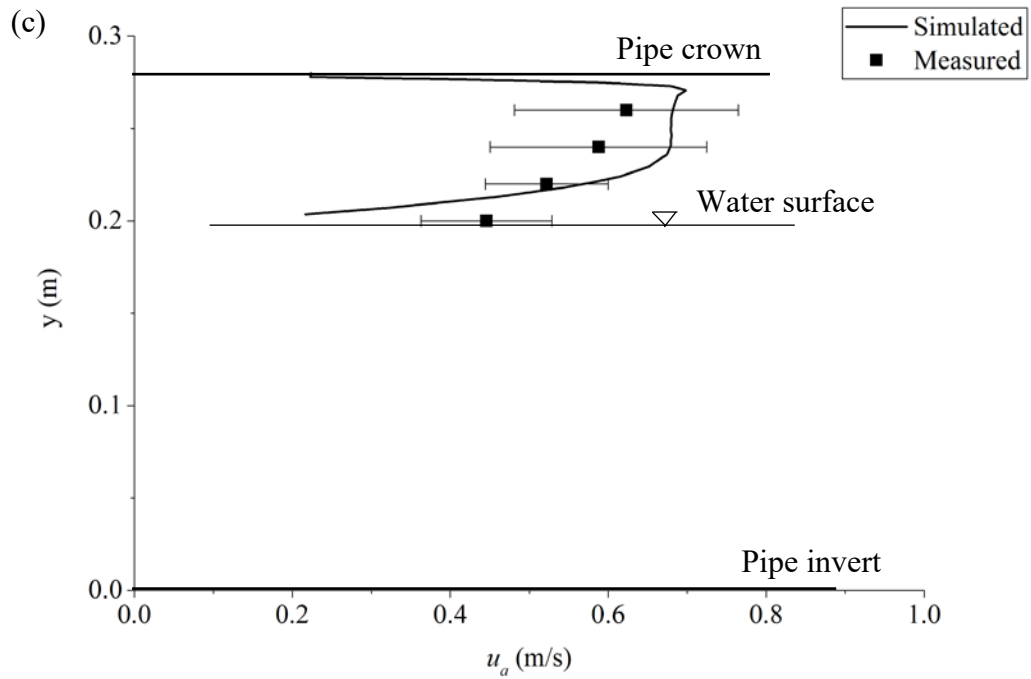


Figure 3-9 Comparison of measured and simulated air velocity profiles at centre plane. $Q_w = 9.88$ L/s, $\theta = 10^\circ$, water level 20 cm in the downstream pipe, $M_s = 0.0015$ kg m/s². (a) 1 m upstream of the pipe joint, (b) 0.5 m upstream of the pipe joint, and (c): 1 m downstream of the pipe joint.

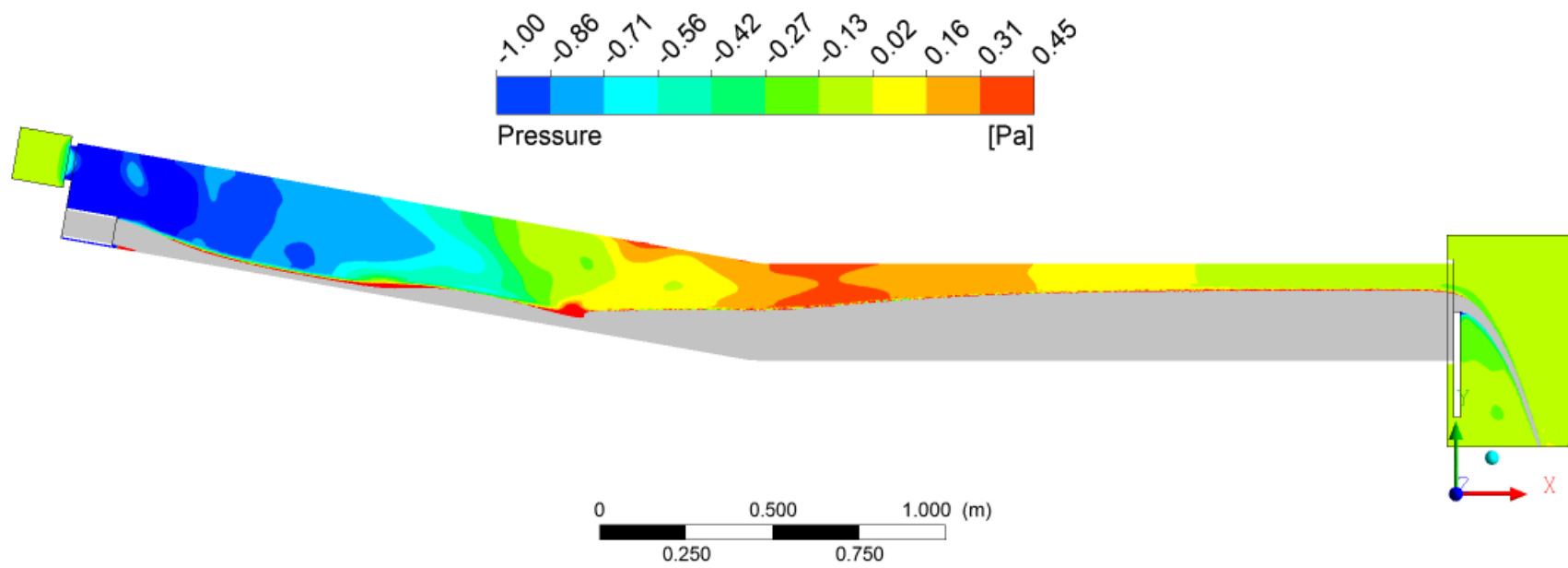


Figure 3-10 Simulated air pressure distribution for B1. $Q_w = 9.88 \text{ L/s}$, $\theta = 10^\circ$, $M_s = 0.0015 \text{ kg m/s}^2$.

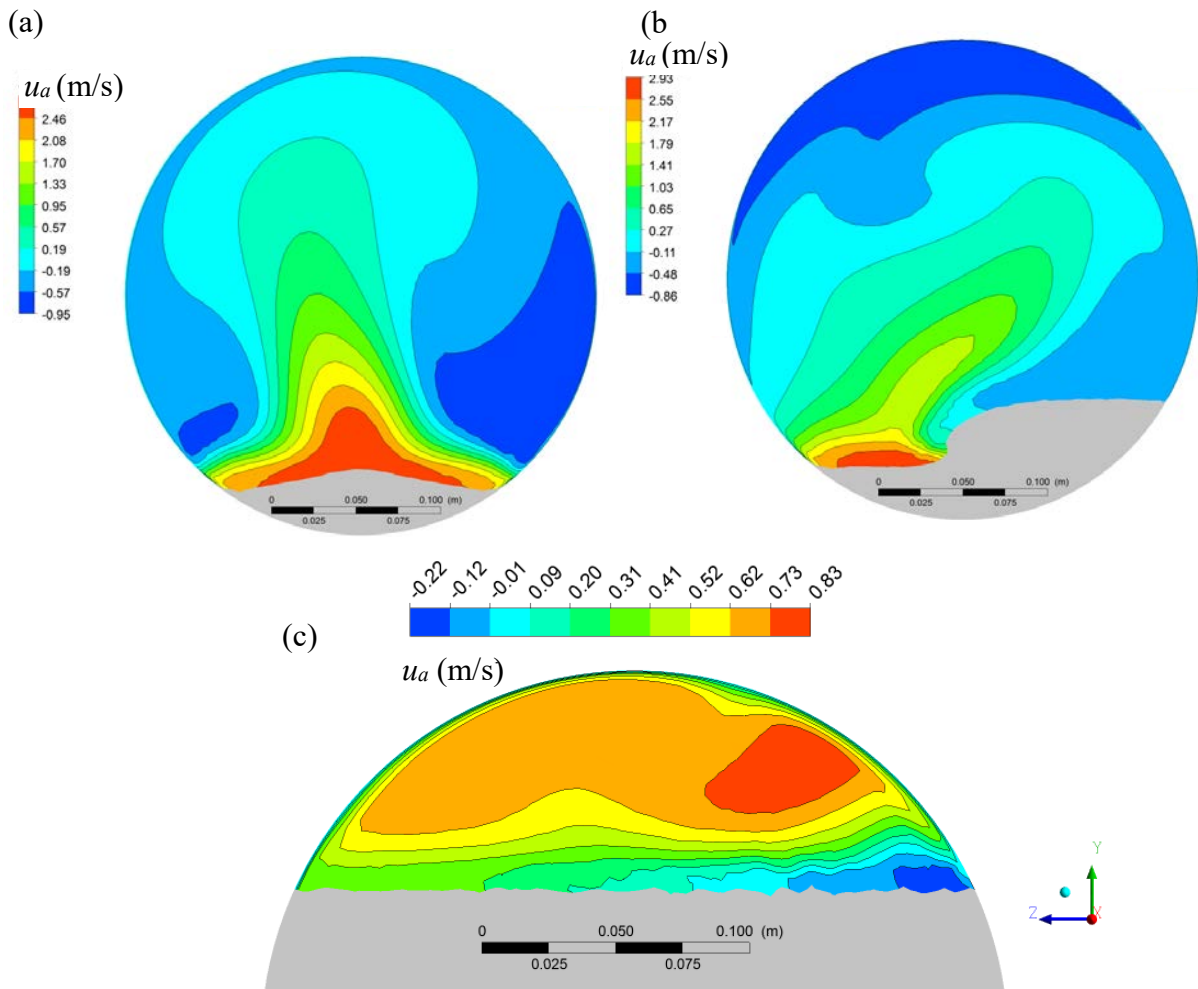


Figure 3-11 Simulated air velocity contour at different locations. (a) 1 m upstream of the pipe joint, (b) 0.5 m upstream of the pipe joint, (c) 1 m downstream of the pipe joint. Looking from downstream. $Q_w = 9.88$ L/s, $\theta = 10^\circ$, $M_s = 0.0015$ kg m/s².

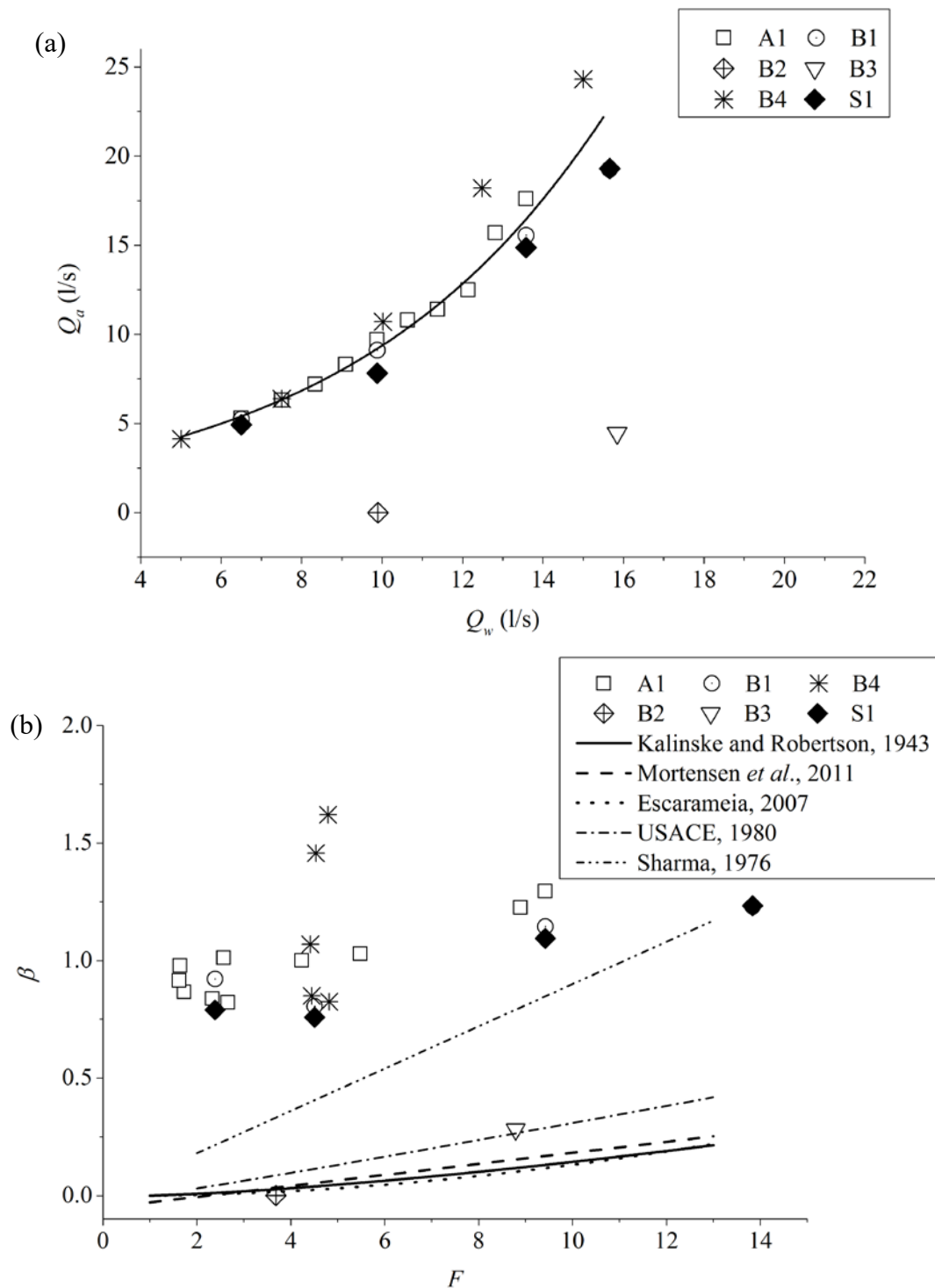


Figure 3-12 Plot of air flow rate in hydraulic jump model. (a) air flow rate versus water flow rate, and (b) ratio of air/water flow rate β versus Froude number at the toe of jump or in supercritical flow (for case B4).

4. Air Flow Modelling in a Prototype Sanitary Sewer System*

4.1. Introduction

Sewer systems are normally designed for conveying sewage flow without much considerations for air movement, and consequently, at certain locations, the pressure in sewer networks may build up and air can be released uncontrolledly (Edwini-Bonsu and Steffler, 2004). The emission of hydrogen sulfide (H₂S), which is generated in the sewer biofilms under anaerobic conditions (US EPA, 1985), is the leading cause for sewer odor complaints. Previous studies indicated that dropshafts can drive significant sewer pressurization (Zhang et al., 2016, Ma et al., 2016). With the effect of dropshafts, the air movement in sewer networks and its modelling is complex. Therefore, knowing the air pressure distribution and air movement in sewer networks is essential for efficient sewer system design.

A number of studies on modelling air movement in a single sewer pipe have been conducted. Pescod and Price (1982) measured the air velocity profile for a single pipe due to wastewater drag and pressure gradient. Other factors affecting the air flow in a pipe include the wind across the stacks, temperature difference, fluctuation of water level, and barometric pressure (Pescod and Price, 1982). However, the magnitude and influence of each factor was insufficiently discussed. Edwini-Bonsu and Steffler (2004, 2006a) numerically studied the air flow in sewer pipes due to a combined effect of water drag and pressure gradient. For a single pipe with no change on momentum flux, the sewage drag force, pressure induced force and the pipe wall friction force should be balanced. Qian et al. (2017) numerically studied the air flow in a straight pipe due to the

* The content of this chapter has been published as: Qian, Y., Zhu, D. Z., and Edwini-Bonsu, S. (2018). "Air Flow Modelling in a Prototype Sanitary Sewer System." *Journal of Environmental Engineering, ASCE*, 144(3): 10.1061/(ASCE)EE.1943-7870.0001342.

increased drag of supercritical water flow and pressure gradient exerted on both ends. Other studies on air flow in dam outworks were reported in U.S. ACE (1980), Tullis and Larchar (2011), which were similar to air flow in a sewer pipe but with a much higher water velocity.

Dropshafts are commonly used to deliver flow to deep trunks. Plunge-type dropshaft is believed to cause a large amount of air entrainment and pressurization of downstream pipes. Rajaratnam et al. (1997) studied the air entrainment in a plunged-type dropshaft with a drop height ranging from 0.98 to 2.9 m. Camino et al. (2014) observed the flow pattern and air demand for a plunging dropshaft with a drop height of 7.72 m. The sewage flow breaks into water drops when falling in the dropshaft. The increased contact area between air and water enhances the drag effect and produces pressure gradient in the dropshaft. Ma et al. (2016) experimentally studied the air demand and developed analytical relationship between the air demand and water flow conditions. The increased drag would induce a large amount of air flow into dropshafts and pressurize downstream pipe through momentum transfer. For a prototype dropshaft, the air flow rate can reach as high as 160 times of the water flow rate (Zhang et al., 2016).

Models were developed for predicting the air pressure and air movement in sewer systems. Edwini-Bonsu and Steffler (2006b) developed a model using a system dynamic approach combining with their earlier research to predict air pressure at each manhole in their study area, and provided a general framework on modelling air flow in sewer systems. However, the pumping effect of dropshafts on air flow was treated as a quadratic pumping characteristic function with assumed parameters. Also, their results were not compared with field measured data. Further study on air movement in dropshafts was recommended by Edwini-Bonsu and Steffler (2006b). Ward et al.

(2011a, b) and Wang et al. (2012) developed a model using the conservation of momentum. Equations of force balance and mass balance between nodes were solved and their results compared generally well with field measurement. However, their model did not include dropshafts and might have limitations when model the system where dropshafts exist. For sewer networks with dropshafts, no literature was found to reliably predict the air flow in sewer networks. Also, the models mentioned above only do calculation in the trunk without considering the air leakage via lateral connections. The leakage air flow through lateral pipes acts similar to a manifold diffuser with its calculation procedure reported in Fischer et al. (1979). The pressure along the lateral pipes decreases due to the release of air at each manhole.

This study is conducted to predict the air movement in sewer networks in a prototype sanitary sewer system. Analytical calculations as well as field monitoring were conducted. The objective of this study is to develop a framework for modelling the air pressure distribution in sewer networks. Also, the amount of air leakage from lateral pipes due to the pressurization in the trunk is assessed. Another objective of this study is to identify the factors of and their magnitude in controlling air movement in sewer system. The third objective is to develop a tool for predicting the pressure distribution in a sewer system, and identifying potential hotspots of odor emissions.

In the City of Edmonton, Alberta, the depth of major trunk sewer could be as deep as 50 meters at certain locations. Sewer flows from lateral pipes are delivered to major trunks using dropshafts and therefore, the systems are prone to pressurization and odor issues (Zhang et al. 2016). With the outcome of this study, one can predict the local air pressurization and detailed air flow in sewer

networks. This study also provides the City of Edmonton with ideas on implementing its city-wide odor mitigation strategy.

4.2. Methodologies

Area of field study

The studied sewer trunk system is located in Edmonton, Alberta, Canada, with a long-term odor issue with air pressurization in the trunk and H₂S odor release. Air in the sewer system leaks from manhole pickholes with measured velocity as high as 50 m/s due to the pressurization. The trunk is 3 km in length with a diameter of 1.5 m and decreases to 1.2 m as shown in Figure 4-1. The starting point of the trunk is denoted as T1 where T means the sewer trunk where flow joins from 2 laterals. The manholes on lateral pipes are denoted as T1-L1, etc. Dropshafts are located at T1-L1, T6, T7 and T8. The studied sewer ends at a pump station denoted as P.S. Fieldwork was carried out in this area in 2016. Detailed description on the fieldwork and result can be found in Guo et al. (2018).

Air pressure in trunk line

The air pressure in the manholes was measured by ACR SmartReader Plus 4 LPD data logger (ARC Systems, Canada). The data loggers were installed under the manhole cover measuring the differential pressure inside and outside of the manhole. The sampling interval was set at 2 min. All devices were carefully calibrated and checked prior to installation.

The air is sucked into the system due to negative pressure induced by the dropshaft at T1-L1. Because the manholes on the trunk are completely sealed, the induced air is leaked out of the

system through manhole openings in lateral pipes. The air flow at each manhole is defined as the air flow in a node. The mass conservation requirement indicates that the air flow into the node equals to the air flow out of the node.

The air movement in the dropshaft is mainly due to the momentum transfer from liquid drops. The pressure gradient in a dropshaft can be estimated following Ma et al. (2016):

$$\frac{dp}{dz} = \frac{3Q_w}{\pi D_s^2 d} C_d \rho_a V_w \left(1 - \frac{V_a}{V_w}\right)^2 \quad (4-1)$$

where p is pressure, z the vertical distance, Q_w the water flow rate, D_s the dropshaft diameter, d drop diameter, V_w water terminal velocity, V_a air velocity, ρ_a air density, C_d drag coefficient and $C_d = 0.4$. This equation was developed from a model with a drop height of about 7 m where the terminal water drop velocity was measured at $V_w = 6$ m/s. Ma et al. (2016) suggested that the pressure gradient at the top 5 meters of the dropshaft is about half of the pressure gradient predicted by Equation 4-1.

For a given air flow rate and water flow conditions, the pressure at the upstream and downstream of a trunk pipe can be estimated according to Qian et al. (2017). In a single pipe, if the momentum of air is not changed, the force induced on air by pressure difference upstream and downstream is to be balanced with the wastewater drag and the friction force on pipe wall. The wastewater drag is to be estimated using a drag coefficient following:

$$C_d^* = 1.91 \times 10^5 \times \left(\left|\frac{dp}{dx}\right| \frac{D-h}{\rho_w V_w^2}\right)^{0.83} \times \left(\frac{h}{D}\right)^{3.23} + 0.043 \quad (4-2)$$

where C_d^* is the drag coefficient at the water surface, D is trunk pipe diameter, h is water flow depth, ρ_w is water density. Assuming there is no change in momentum flux, an expression on the force balance equation can be written as:

$$\underbrace{\pm \frac{1}{2} C_d^* \rho_a (V_w - V_a)^2 B}_{\text{Drag force}} \underbrace{\pm \frac{dp}{dx} A_a}_{\text{Pressure difference}} \underbrace{\pm \frac{f}{8} \rho_a V_a^2 P_a}_{\text{Friction force}} = 0 \quad (4-3)$$

where A_a is the area of air flow, B is the width of water surface, where f is the Darcy-Weisbach friction coefficient, P_a is the non-wetted perimeter. The sign \pm of each term depends on the direction of air flow and the relative velocity between air and water.

Calculation of air flow in lateral pipes

As shown in Figure 4-2, the pressurized trunk will cause air to leak out of the sewer system from manhole pickholes at lateral connections via manhole 1, 2, 3 and so on. The leakage of air at lateral connection determines the total flow rate in the trunk and the flow rate should be in accordance with the air induced by dropshaft. A higher pressure in the trunk will cause more air to leak through lateral connections. The amount of air leakage is determined by the lateral pipe properties, number of lateral pipes, and the pressure in the trunk. The pressure in the lateral pipes decreases along the line due to pipe friction and pressure release at manholes. Notice that beyond a certain distance, the lateral pressure drops to a low level and the amount of the air leakage becomes insignificant. When the change of the total air flow is within 0.5% of the air flow if the number of pipe is increasing, the distance is defined as the zone of influence.

The major forces exerting on the air flow in a sewer pipe include the drag of wastewater, pressure gradient force, and the friction force. The drag of wastewater per unit pipe length is $\frac{1}{2} C_d^* \rho_a B (\Delta V)^2$ where C_d^* is of order of 0.1 (Qian et al., 2017), ΔV is the relative velocity between air and water. The friction force per unit pipe length can be written as $\frac{f}{8} \rho_a P_a V_a^2$. The summation of wastewater drag force and friction force should be balanced by the pressure induced force in a

pipe. However, the wastewater drag force is a function of water depth, pressure gradient, etc. Assuming the velocity of water flow in the lateral pipes is much smaller than the velocity of air, based on $\frac{1}{2}C_d^* \rho_a B(\Delta V)^2$ for wastewater drag and $\frac{f}{8} \rho_a P_a V_a^2$ for pipe wall friction, an order of magnitude analysis suggests that the summation of wastewater drag force and friction force per unit length can be written as ($C_d^* = 0.1$):

$$0.06BV_a^2 + 0.0045P_aV_a^2 \approx \frac{f^*}{8} \rho_a \pi D V_a^2 \quad (4-4)$$

where: f^* is the corrected friction coefficient considering the drag by wastewater.

Hydraulic calculation was made on the air flow rate through lateral pipes. A theoretical derivation on the pressure at the trunk and the flow rate through lateral pipes yields an expression of $Q_a = Kp^{0.5}$, where: Q_a is the air flow rate through lateral pipes, p is the pressure in the trunk, and K is a leakage coefficient which corresponds to the characteristic of the lateral pipes.

Following are the assumptions made for the lateral leakage model. Lateral connection is without loops and any further branches. Each of the lateral pipes has a diameter of D and length of L as shown in Figure 4-2. Air leakage is driven by the pressure at the trunk and air only leaks through four pickholes with a diameter of $D_{MH} = 2.5$ cm on the manhole cover located on lateral pipes. The trunk manhole covers are sealed, as is the case in the study sewer system. The area of manhole pickholes $A_{MH} = \pi D_{MH}^2$. Calculating from the furthest manhole in the lateral connections, the pressure and air flow rate in pipe $i+1$ can be written as:

$$p_{i+1} = p_i + f^* \frac{8\rho_a L}{\pi^2 D^5} Q_i^2 \quad (4-5)$$

$$Q_{i+1} = Q_i + A_{MH} \sqrt{\frac{2}{\rho_a} p_{i+1}}^{0.5} \quad (4-6)$$

where: p_i is the pressure at i -th manhole starting from the furthest manhole. Q_i is the air flow rate in pipe i . Equations 4-5 and 4-6 form a set of non-linear equation system. The solution to the equation system is implicit and cannot be derived directly.

The flow rate Q_i is a summation of the air flow rate via manhole pickholes from the furthest manhole to manhole i . For a fixed pressure at the trunk, Equation 4-5 suggests that the pressure drops as a function of Q_a^2 and Equation 4-6 shows that the flow rate decreases as a function of $p^{0.5}$. Therefore, after certain distance, the local pressure continues decreasing and the flow rate through manhole pickholes decreases and becomes negligibly small. The additional lateral pipe does not contribute much on the air flow. Equations 4-5 and 4-6 suggest that the zone of influence is only affected by $f^* \frac{8\rho_a L}{\pi^2 D^5}$.

Figure 4-3a is a plot of the number of pipes that when the K values reach a certain portion of the maximum possible K values with different $f^* \frac{8\rho_a L}{\pi^2 D^5}$ values. The percentage in the figure shows the relative change of the K value with one more pipe added. The 0.5% line is the zone of influence where the relative change of K values reaches 0.5% if one more pipe is added. Therefore, for a given $f^* \frac{8\rho_a L}{\pi^2 D^5}$, if the number of pipes is more than the zone of influence, extra pipe will not impact on the air flow through the lateral connection. From the figure, it can be also seen that for a higher $f^* \frac{8\rho_a L}{\pi^2 D^5}$ value, the pressure drops faster due to high head loss in the pipes and the zone of influence is therefore small.

Figure 4-3b shows a plot of the K values as a function of pipe numbers and $f^* \frac{8\rho_a L}{\pi^2 D^5}$. From the figure it can be seen that for a certain head loss coefficient, the leakage coefficient K increases with pipe number. The envelop line of Figure 4-3b is when pipe number is 100. No further increase of K values was observed when more pipes are considered. The K values obtained from Figure 4-3b is defined as simplified method.

Field pressure measurements were obtained at T8 and all its lateral pipes to validate the air leakage model discussed above. Figure 4-4a shows the actual pipe connection at T8. There are 6 lateral pipes connected to T8. The lateral pipes have an averaged diameter of 0.23 m and length of 53.30 m. Figure 4-4b is a one-day pressure changes during the fieldwork. A special bursting pattern of pressure can be observed due to the operation of the pump station where a decrease of the water level in the pump station decreases the water level in the sewer trunk. The free surface reaches T7 and T8 and the head space of these two manholes connects with the upstream pipe with high pressure at the head space. The measured non-zero pressure was normalized by the pressure at T8-L1 and plotted in Figure 4-4c. The standard deviation of the measured pressure is also plotted in Figure 4-4c. Sensitive analysis was conducted on the corrected friction coefficient f^* and shown in Figure 4-4c. The pressure at lateral lines decreases when the friction coefficient increases. The estimated pressure at T8 and its lateral pipes agrees well with the measured ones when $f^* = 0.03$. Therefore, the corrected friction coefficient f^* for air is determined at 0.03.

For lateral pipes with further branches or loops, the pressure, air flow rate and head loss of air along the lateral line depend on the pressure at trunk, the actual connection, and the properties of the pipes. By following the lateral connection, the air flow rate through the lateral pipes and the

pressure at each manhole can be calculated for a given trunk pressure. This method is defined as conventional method hereafter. Due to the actual pipe configurations and change in pipe diameter and lengths, the K value from the conventional method may differ from the simplified method. Table 4-1 is a comparison of the K values for a given lateral connection calculated by the conventional method and the simplified method. The maximum difference of K values from the simplified and the conventional method is about 12%.

The $f^* \frac{8\rho_a L}{\pi^2 D^5}$ value of the lateral of T8 is 2416 kg/m⁷. According to Figure 4-3a, the zone of influence is about 25 pipes. Figure 4-3b shows the K values is 0.0110 kg^{-0.5}m^{3.5}. Using the conventional method, the K value is 0.0121 kg^{-0.5}m^{3.5} which is close to the predicted one. Similarly, for other lateral connections, simplification can be made to use the averaged diameter and length to predict the K values from Figure 4-3b.

Additionally, due to the difficulties in directly measuring the air flow rate in the lateral pipes, the total flow rate via the laterals connected to T8 is estimated by calculating the air flow rate at each manhole using the measured pressure data. Figure 4-4d is a comparison of the flow rate calculated from the measured pressure and predicted using the K value from the simplified method. The figure suggests that the K value obtained from the simplified method agrees well with the air flow rate calculated from the measured pressure. Considering the complexity of the actual connections, calculating the K values using the conventional method for each lateral connections is not practical. Therefore, it is reasonable to use the simplified K to obtain a close estimation of the air flow out of lateral connections.

The K value for T6, T7 and T8 are therefore estimated as 0.0879, 0.0253, and 0.0125 $\text{kg}^{-0.5}\text{m}^{3.5}$ respectively. The K values for T1-L1 is to be calibrated from the measured data because the connection upstream of T1-L1 has multiple laterals.

Model framework

The field measurement data suggested that the pressure at manhole T10 and T9 was around 0Pa. The model starts with the period that the headspace of T8 is connected with the pressurized headspace of upstream pipe. Therefore, the downstream boundary of the pressure estimation is T8. The model starts with an initial guess on the pressure at T8 and the air flow rate through T8's lateral pipes. The air flow rate in the trunk between T7 and T8 equals to the air flow rate through T8's lateral connections.

The following assumptions are made due to the complexity of the system: the wastewater discharge via lateral pipe was estimated as 3 L/s for T8 and 10 L/s for T7 according to their catchment areas. Two steady-state pressure calculation was conducted. Case 1 is when the headspace of T8 and T7 are connected with upstream trunk at 16:30. Case 2 is when the headspace of T8 and T7 are not connected at 03:00.

Based on equation 4-3, the first term indicates the drag force inducted by the wastewater flow. The second term is the force due to pressure, and the third term is the pipe friction. For a pipe with no momentum change on air flow, these three forces should be balanced. Given the upstream pressure, water flow condition, and the property of the pipe, the downstream pressure can be calculated using equation 4-3. Then, the air flow rate in the trunk between T6 and T7 can be obtained by

adding the air flow rate in the trunk between T7 and T8 and the air flow rate through T7's lateral connections. The pressure at T6 can be calculated based on the air flow rate in the trunk, downstream pressure and wastewater flow information. Following this procedure, the pressure and air flow rate at each manhole can be calculated. At a dropshaft, the pressures in the trunk and before the dropshaft at ground level are calculated. The difference of these two pressures is the pressure gradient caused by the dropping water. The pressure in the trunk is used to calculate the air flow in the trunk following the procedure discussed above and the pressure before the dropshaft at ground level is used to calculate the air flow through lateral pipes using the K values calculated for the specific lateral connection. Once the calculation reaches T1-L1, the pressure estimated at T8 is to be adjusted until the air flow into the system equal to the total air leakage flow.

4.3. Results and discussions

Sewage flow validation

The wastewater level in the pump station (P.S.) was continuously monitored. The wet well has a cylindrical shape with a diameter of 4.9 m. The volume of water in the system is the water volume in the wet well plus the volume in the trunk. The net wastewater flow rate can be estimated from the rate of change of monitored water volume. The water inflow would be the net flow rate minus the pump flow rate. Figure 4-5 shows the comparison between simulated and monitored wastewater flow. The diurnal change and magnitude of derived wastewater discharge compares well with the simulated ones. Therefore, using the simulated wastewater flow data for predicting air flow is reasonable.

Pressure distribution along the trunk line

Figure 4-6 shows the measured pressure distribution along the trunk. The pressure between T2 and T5 fluctuates with obvious diurnal changes and with a similar magnitude. The pressure at T7 and T8 shows a different pattern due to the pump operations. The fieldwork showed that the pressures at manholes T9 and T10 were always around 0 Pa. This suggested that the trunk was flowing in full and the upstream pressurized head space cannot reach T9 and further downstream.

The simulated and measured pressure at 16:30 and 03:00 is plotted in Figure 4-7a and b. The error bars show the variations of pressure at the same time on different days. For case 1, T8 has a measured pressure of around 500 Pa. T7 has a lower pressure at around 260 Pa and it is mainly because T7 has a larger catchment area and therefore larger water flow rate. The dropshaft at T7 would produce a larger pressure gradient and therefore results in a lower measured pressure at T7. The measured pressure at T6 is around 350 Pa. For manholes T5 to T2, because they are directly connected to the trunk, and without lateral connections and dropshafts, the measured pressure is at around 550 Pa. For the pressure at the most upstream dropshaft T1-L1, negative pressure of around -10 Pa was observed. This negative pressure is for air suction from further upstream. The uncertainty for the field measurement comes mainly from the minor changes of flow rate at different days, as well as the weather condition.

Figure 4-7a shows the simulated pressure at each manhole and the measured one for case 1. The simulated pressure at each manholes is in good agreement with the measured ones. The maximum pressure difference is about 29% at T6. The predicted pressure in the trunk at each manhole is almost the same at around 560 Pa. The difference at T8, T7, and T1-L1 mainly comes from the

predict pressure gradient generated in dropshafts. The pressure gradient predicted from equation 4-1 generally performed well compared with laboratory results when considering a pressure gradient reduced by half at the first 5 m of drop. Due to the large size of the water column from the prototype inlet pipe, the actual breakup length can be larger than 5 m and a larger breakup length can lead to a smaller pressure gradient. Therefore, the total pressure gradient calculated by Equation 4-1 was reduced by 60% to match the predicted pressure to the measured ones. At other manholes, the difference is within 15%. The K value for T1-L1 is estimated as $0.75 \text{ kg}^{-0.5} \text{ m}^{3.5}$. The high K value at T1-L1 is mainly due to the large tributary area upstream. The simulated air flow rate for case 1 is $2.2 \text{ m}^3/\text{s}$.

Figure 4-8b shows the pressure distribution along the trunk at 03:00 (Case 2). The trunk at T7 and T8 ran full pipe flow and not connected with the pressurized upstream pipe in this case. In this scenario, the water level at the pump station was high and the full pipe flow condition moved further upstream of T7. Also the predicted pressure at T5, T4, T3 and T2 compares well with the measured ones. Similar to case 1, for the pressure at T1-L1, the pressure gradient predicted was multiplied by 0.37 to match the predicted and measured pressure. The simulated air flow rate for this case is $1.1 \text{ m}^3/\text{s}$ according to the K value of $0.75 \text{ kg}^{-0.5} \text{ m}^{3.5}$ for T1-L1 and the negative pressure calculated at -2.2 Pa .

Air flow rate in the trunk

The air flow rate in the trunk is difficult to measure directly because the trunk is deep and difficult to access. The air flow rate in the trunk is therefore estimated by comparing the measured pressure drop. Although the pressure from T2 and T5 is similar, air flow can still be derived using the

pressure difference using the equation: $\Delta p = f^* \frac{L}{D} \frac{Q_a^2}{2A_a^2} \rho_a$. Figure 4-8 is a plot of estimated air flow rate from the pressure difference between T2 and T5. Diurnal change on air flow rate can be seen from the figure. Most of the air flow rates are with positive values which means the air flows downstream. The positive part of the air flow rate appears at night when pressure valley occurs between 00:00 to 08:00. However, negative air flow rate can be seen in day times roughly from 08:00 to 24:00. The negative air flow rate indicates that the pressure at T5 is bigger than T2 and the air flows towards upstream. This is because that the pressure in the trunk fluctuates during the day and the pressures at T2 and T5 are close to each other. T5 is close to a dropshaft at T6. The water inflow at T6 may influence the pressure at T5 at high sewage flow condition. The uncertainty of the air flow rate analysis comes mainly from the corrected friction coefficient f^* . The current f^* of 0.03 is based on the measurement at T8 and may be slightly different for the trunk from T2 to T5. However, the air flow rate Q_a is proportional to $\sqrt{f^*}$ where the change of f^* does not influence much on Q_a . Therefore, the predicted air flow rate in the trunk is reasonably well. The actual pressure difference between T2 and T5 is in order of 20 Pa which is small comparing to the maximum pressure values in these two manholes of about 800 Pa. The small pressure difference is a significant uncertainty for the measurement.

The negative air flow rate alters with positive flow rate. The air is moving forward and backward. The total transportation of air downstream is therefore decreased due to this phenomenon. The averaged air flow rate for the positive flow rate is around 2.0 m³/s, and with the negative air flow rate, the averaged air flow rate is 1.2 m³/s. The measured air flow rate is close to the simulated 2.2 m³/s for Case 1 where the laterals connected to T7 and T8 are included and 1.1 m³/s for Case 2 where the laterals of T7 and T8 not included due to downstream surcharge.

Effect of dropshaft on downstream pressurization

Dropshafts have been identified as the key factor for downstream pressurization (Zhang et al., 2016). Figure 4-9 is a plot of the measured pressure change due to the dropshaft at T1-L1 with the one predicted by Ma et al. (2016) (Equation 4-1). For high air flow rate at 2 m³/s, the predicted pressure change is at the top limit of the measured data. Several assumptions were made when developing the Equation 4-1. Ma et al. (2016) measured that the water flow broke into droplets at 5 m, and in current case, the breakup length can be longer due to a larger jet size. If the water flow breaks into a larger drop diameter, a lower pressure drop can be generated according to Equation 4-1. Another uncertainty comes from the air/water velocity. The terminal velocity of water drops used in this study is 6 m/s. If the pressure gradient in the dropshaft changes, the terminal velocity of droplets can change accordingly and therefore changes the pressure gradient.

If the air flow rate is lower, Equation 4-1 tends to over predict the pressure change by up to 40%. This is because that the terminal velocity of water drops is estimated as 6 m/s according to the physical observations of Ma et al. (2016). The relative velocity between air flow and water drops therefore increases for a lower air flow rate, and a larger pressure change is estimated. At prototype dropshafts, the terminal drop velocity is unknown. Therefore, prototype measurement on the terminal velocity of water drops, drop sizes, and the breakup length are of importance in order to successfully predicting the pressure change due to dropshafts. Further study is needed in order to apply the equation for field applications.

Factors influencing the air flow in pipes with dropshafts

The three forces in equation 4-3 between two manholes for Case 1 and Case 2 are plotted in Figure 4-10. For Case 1, the force induced by pressure difference overweigh the other two forces. This is because for this case, the air is flowing in the same direction as the water flow but at a higher velocity. The direction of wastewater drag is therefore the same as the friction force. The pressure force needs to balance the other two forces and therefore, it is the highest in Case 1. For Case 2, due to the low water flow rate and low air flow rate, the wastewater drag force is low. To balance the pressure force, a high friction force is observed. However, the magnitude of the overall force is smaller than that of Case 1.

Other factors that influence the air flow in sewer systems include the temperature, barometric pressure, and the fluctuation of water level (Pescod and Price, 1982). The temperature difference inside and outside of the manholes mainly induces buoyance force to enhance the release of air via manhole pickholes. Assuming the ambient air is $-20\text{ }^{\circ}\text{C}$ and the sewer air is $10\text{ }^{\circ}\text{C}$, the density of air is 1.394 kg/m^3 and 1.247 kg/m^3 respectively (Potter et al., 2012). Assuming the exit velocity is 30 m/s due to the pressurization of around 500 Pa , for a single manhole pickhole, the air flow rate $Q_a = 0.0147\text{ m}^3/\text{s}$. the turbulent jet and plume theory (Fischer et al., 1979) suggests that the momentum flux is $0.441\text{ m}^4/\text{s}^2$, and the buoyancy flux is $0.017\text{ m}^4/\text{s}^3$ which is much less than the momentum flux. The velocity induced by the pressure change is 30 m/s while the velocity induced by the density difference is 1.2 m/s at 1 m above the manhole pickhole. The velocity induced by the pressure difference is much larger than the one induced by the density difference. Therefore, the effect of the density difference on the air flow is minor compared with the effect of pressure difference.

Given the diurnal change and the long period oscillation of water flow, the rate of the change on water level in sanitary sewer system is relatively small comparing with storm sewer. The Mike Urban simulation provided by the City of Edmonton suggests that the filling ratio in the study trunk varies between 0.08 and 0.13. For the pipe diameter of 1.5 m, length of 300 m, the volume of change is 19.5 m^3 . The shortest time duration between high and low water level is 2 hr. Therefore, the air flow rate induced by the change of wastewater level is $0.003 \text{ m}^3/\text{s}$. Comparing with the actual air flow rate of around $2 \text{ m}^3/\text{s}$, the air flow induced by water level change can be neglected.

Additionally, the barometric pressure can change during a day. The change is generally in a large area. Although the change of barometric pressure may have significant influence on total air inflow or outflow of the system, the relative pressure in the manholes increase or decrease simultaneously. Therefore, minor changes on air flow due to pressure difference in trunk are expected. For a trunk of around 3 km, the change of barometric pressure is synchronized and therefore has minimum influence on the air flow in sewer pipes.

4.4. Conclusions

A conceptual model was developed for simulating the pressure distribution and the air movement in a prototype sewer system in Edmonton, Alberta, Canada. Two simulations were conducted for two typical flow conditions obtained from the fieldwork. The simulated results agreed well with the field measurements. The model was also found stable and robust according to sensitive analysis.

A lateral leakage model is developed and performed well comparing with field measurement. It was found that the leakage coefficient is a function of pipe properties and pipe number. For lateral pipes with certain property, the leakage coefficient increases with pipe number and reaches a certain value which is defined as zone of influence.

Among all possible factors affecting the air flow in sewer pipes, the wastewater drag, pressure force and friction force are the three dominating factors. Other factors such as the temperature change, rise and fall of water level, barometric pressure change were analyzed and it showed that they had limited effect on the air flow in sewer pipes.

Current model tends to over-predict the pressure change in a dropshaft. For high air flow rate, the predicted pressure change is generally close to measured ones. However, for low air flow rate, the predicted pressure change is larger than measured ones. The main discrepancy comes from three areas: drop diameter, breakup length, and terminal velocity. Due to a lack of field measurement, a bulk reduction factor was used in the current study.

Acknowledgement

The writers gratefully acknowledge the financial support from the City of Edmonton, Natural Sciences and Engineering Research Council (NSERC) of Canada, and the China Scholarship Council (CSC). The writers would also like to thank Perry Fedun for his technical supports and all crew members for their assistance on the field work conducted in the summer of 2016.

List of symbols

A_a : Area of air flow.

A_{MH} : Area of manhole pickholes.

B : Width of water surface.

C_d : Drag coefficient in dropshaft $C_d = 0.4$.

C_d^* : Drag coefficient between water surface and air.

D : Sewer pipe diameter.

D_{MH} : Diameter of manhole pickhole.

D_s : Dropshaft diameter.

K : Leakage coefficient.

L : Sewer pipe length.

N : Pipe numbers.

P_a : Non-wetted Perimeter.

Q_a : Air flow rate.

Q_w : Water flow rate.

V_w : Water velocity.

V_a : Air velocity.

d : droplet diameter.

f : Darcy-Weisbach friction coefficient.

f^* : Corrected friction coefficient.

g : Accelerate due to gravity.

h : Water flow depth.

p : Pressure.

z : Vertical distance from the inlet of a dropshaft.

ρ_a : Air density.

ρ_w : Water density.

References

Associate Engineering (AE) (2008). “Odor control program report.” for the City of Edmonton, Alberta, Canada.

Camino, G. A., Zhu, D. Z., and Rajaratnam, N. (2014). “Flow observations in tall plunging flow dropshafts.” *Journal of Hydraulic Engineering, ASCE*, 141(1): 06014020.

Edwini-Bonsu, S., and Steffler, P. M. (2004). “Air flow in sanitary sewer conduits due to wastewater drag: a computational fluid dynamics approach.” *Journal of Environmental Engineering Science*, 3(5): 331-342.

Edwini-Bonsu, S., and Steffler, P. M. (2006a). “Dynamics of air flow in sewer conduit headspace.” *Journal of Hydraulic Engineering*, 132(8): 791-799. 10.1061/(ASCE)0733-9429.

Edwini-Bonsu, S., and Steffler, P. M. (2006b). “Modeling Ventilation Phenomenon in Sanitary Sewer Systems: A System Theoretic Approach.” *Journal of Hydraulic Engineering*, 132(8): 778-790. 10.1061/(ASCE)0733-9429.

Fisher, H. B., List, E. J., Koh, R. C. Y., Imberger, J., and Brooks, N. H. (1979). “*Mixing in Inland and Coastal Waters.*” Academic Press. San Diego, California.

Guo, S., Qian, Y., Zhu, D., and Edwini-Bonsu, S. (2018). “Effects of Drop Structures and Pump Station on Sewer Air Pressure and Hydrogen Sulfide: Field Investigation.” *Journal of Environmental Engineering*, 144(3): 10.1061/(ASCE)EE.1943-7870.0001336.

Ma, Y., Zhu, D. Z., and Rajaratnam, N. (2016). “Air entrainment in a tall plunging dropshaft.” *Journal of Hydraulic Engineering*, 10.1061/(ASCE)HY.1943-7900.0001181, 04016038.

Pescod, M. B. and Price, A. C. (1982). “Major factors in sewer ventilation.” *Journal of Water Pollution Control Federation*, 54(4), 385-397.

Potter, M. C., Wiggert, D. C., and Ramadan, B. H. (2012). “*Mechanics of Fluids.*” 4th edition, Cengage Learning. Stamford, Connecticut.

Qian, Y., Zhu, D. Z., Zhang, W. M., Rajaratnam, N., Edwini-Bonsu, S., and Steffler, P. (2017). “Air movement induced by water flow with a hydraulic jump in changing slope pipes.” *Journal of Hydraulic Engineering*, 143(4): 10.1061/(ASCE)HY.1943-7900.0001252, 04016092.

Rajaratnam, N., Mainali, A., and Hsung, C. Y. (1997). “Observations of flow in vertical dropshafts in urban drainage systems.” *Journal of Environmental Engineering*, 123(5): 486-491. 10.1061/(ASCE)0733-9372.

Tullis, B., and Larchar, J. (2011). “Determining air demand for small- to medium-sized embankment dam low-level outlet works.” *Journal of Irrigation and Drainage Engineering*, 137(12): 793-800. 10.1061/(ASCE)IR.1943-4774.0000345.

U.S. Army Corps of Engineers (US ACE) (1980). “Engineering and design: hydraulic design of reservoir outlet works.” *Report. EM1110-2-1602*. Washington, DC

U.S. Environmental Protection Agency (US EPA) (1985). “Design manual: odor and corrosion control in sanitary sewerage systems and treatment plants.” *Report. epa/625/1-85/01*, Washington, DC.

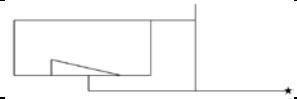

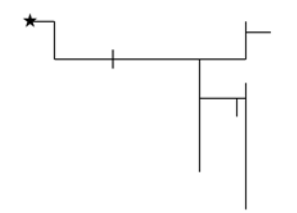

Wang, Y. C., Nobi, N., Nguyen, T., and Vorreiter, L. (2012). “A dynamic ventilation model for gravity sewer networks.” *Water Science and Technology*, 65(1): 60-68.

Ward, M., Corsi, R., Morton, R., Knapp, T., Apgar, D., Quigley, C., Easter, C., Witherspoon, J., Pramanic, A., and Parker, W. (2011a). “Characterization of natural ventilation in wastewater collection systems.” *Water Environment Research*, 83(3): 265-273.

Ward, M., Hamer, G., McDonald, A., Witherspoon, J., Loh, E., and Parker, W. (2011a). "A sewer ventilation model applying conservation of momentum." *Water Science and Technology*, 64(6): 1374-1382.

Zhang, W. M., Zhu, D. Z., Rajaratnam, N., Edwini-Bonsu, S., Fiala, J., and Pelz, W. (2016). "Use of air circulation pipes in deep dropshafts for reducing air induction into sanitary sewers." *Journal of Environmental Engineering*, 142(4): 04015092. 10.1061/(ASCE)EE.1943-7870.0001046.

Table 4-1 Comparison of K values from conventional and simplified method.

Avg. D (m)	Avg. L (m)	Pipe layout (Not to scale)	Number of pipes	$f \frac{8\rho aL}{\pi^2 D^5}$ (kg/m ⁷)	K (Conventional method) (kg ^{-0.5} m ^{3.5})	K (Simplified method) (kg ^{-0.5} m ^{3.5})	Difference
0.20	45.27		24	4128	0.0098	0.0095	3%
0.25	62.74		8	1875	0.0125	0.0118	6%
0.29	69.14		42	1036	0.0179	0.0158	12%
0.23	53.30		6	2416	0.0121	0.0110	10%

Stars indicate trunk manhole.

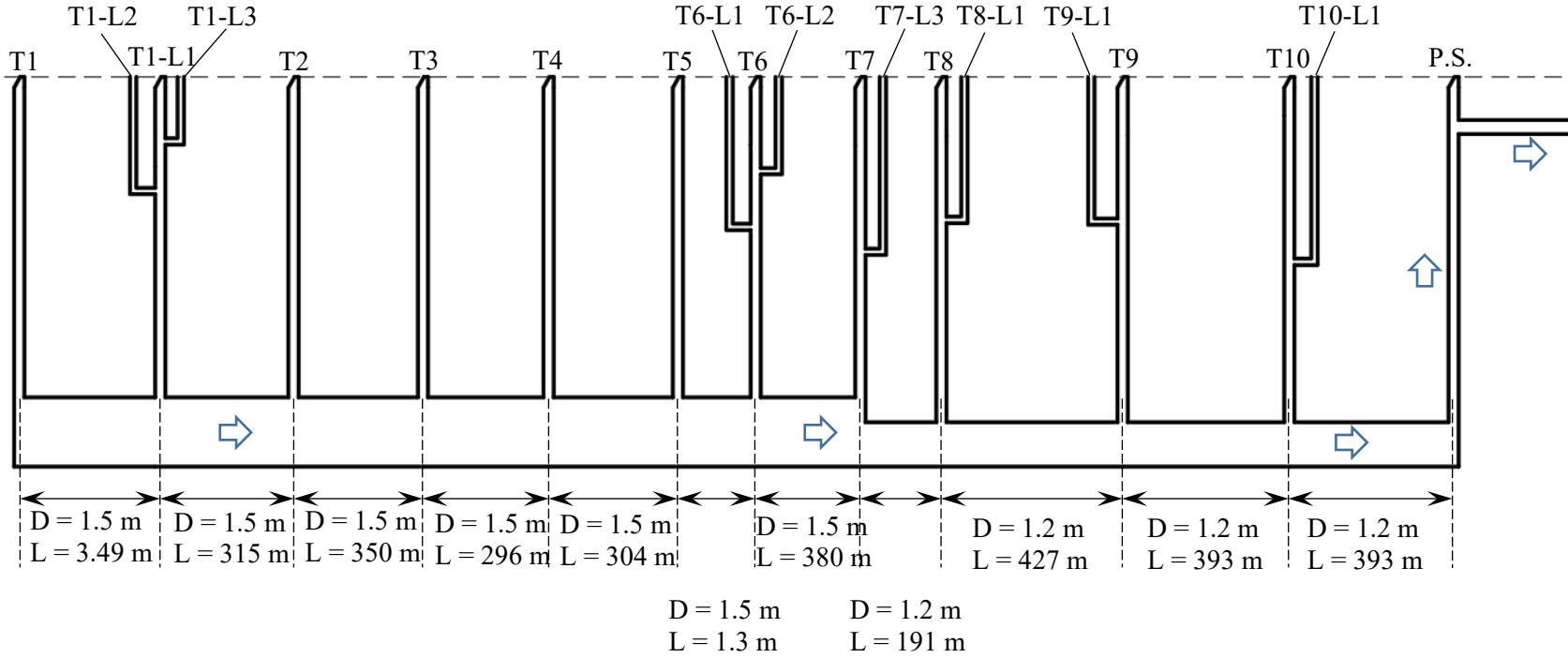


Figure 4-1 Schematic drawing of the sewer system. Drawing not to scale.

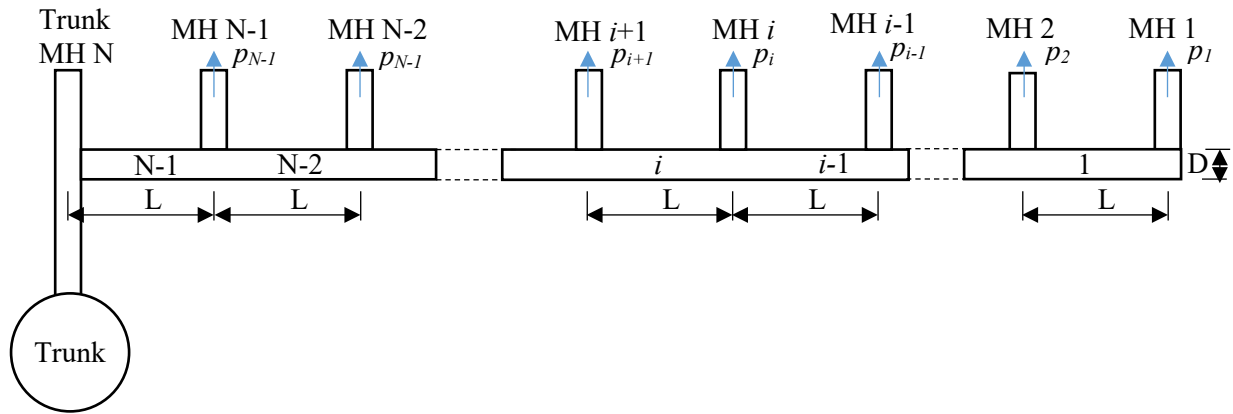


Figure 4-2 Schematic of an idealized lateral connection.

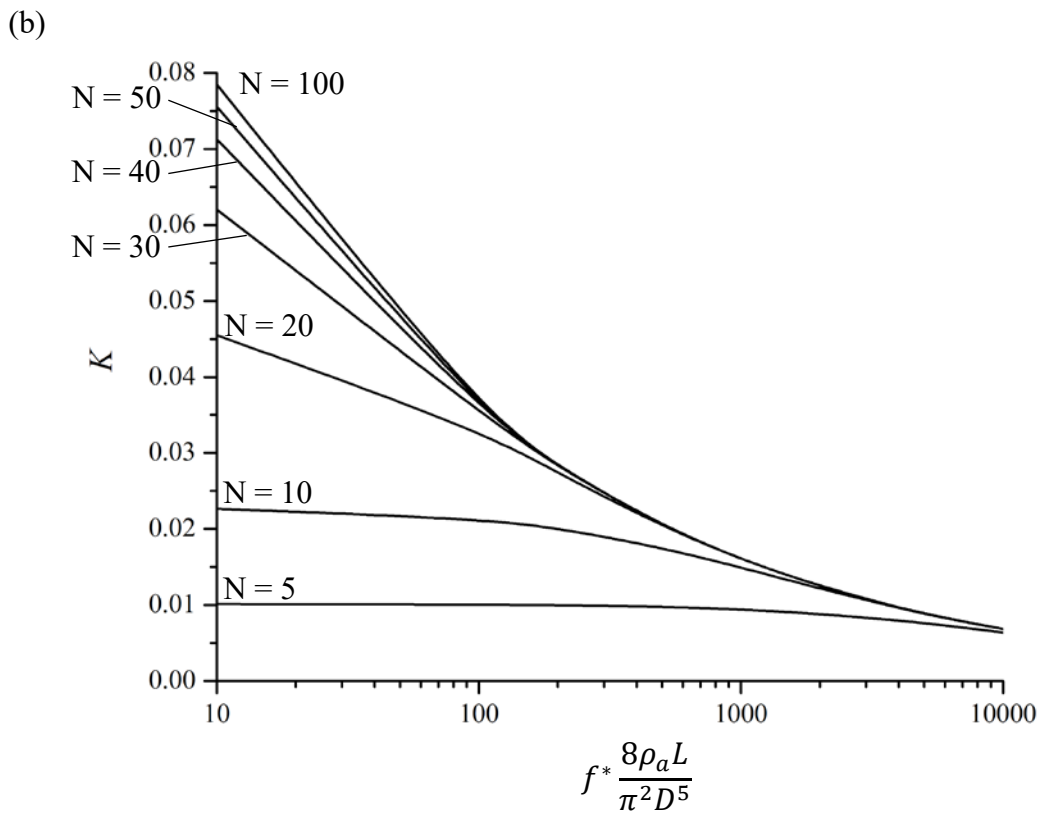
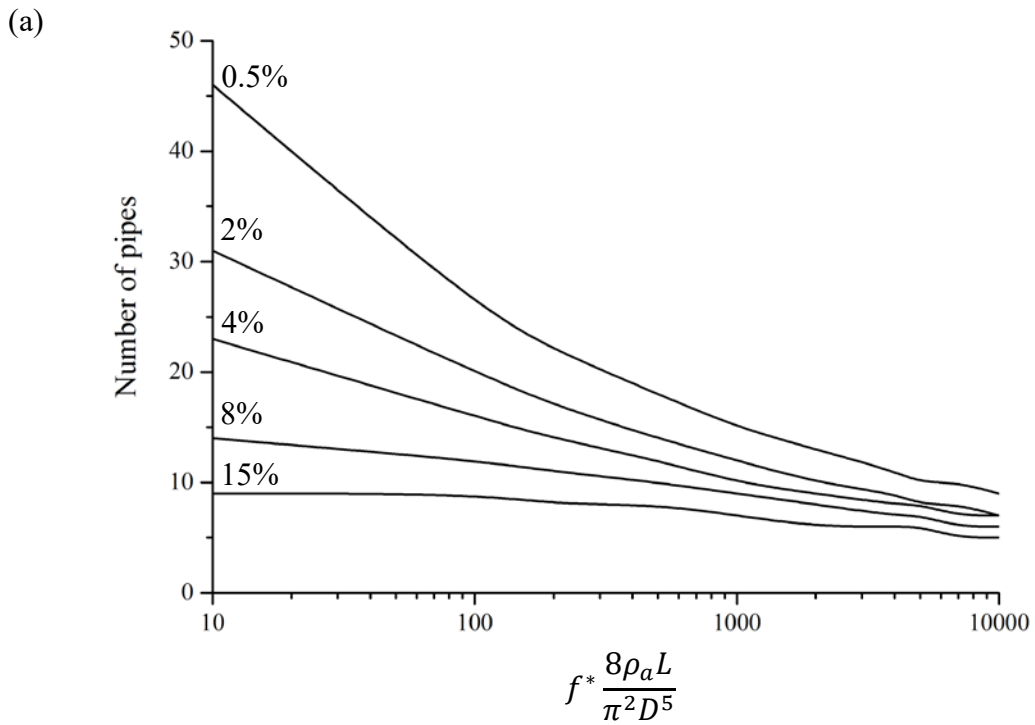
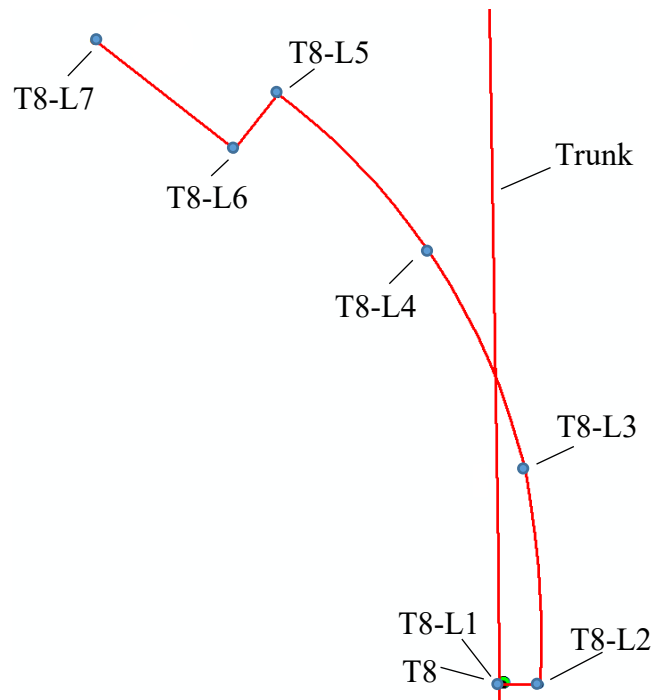
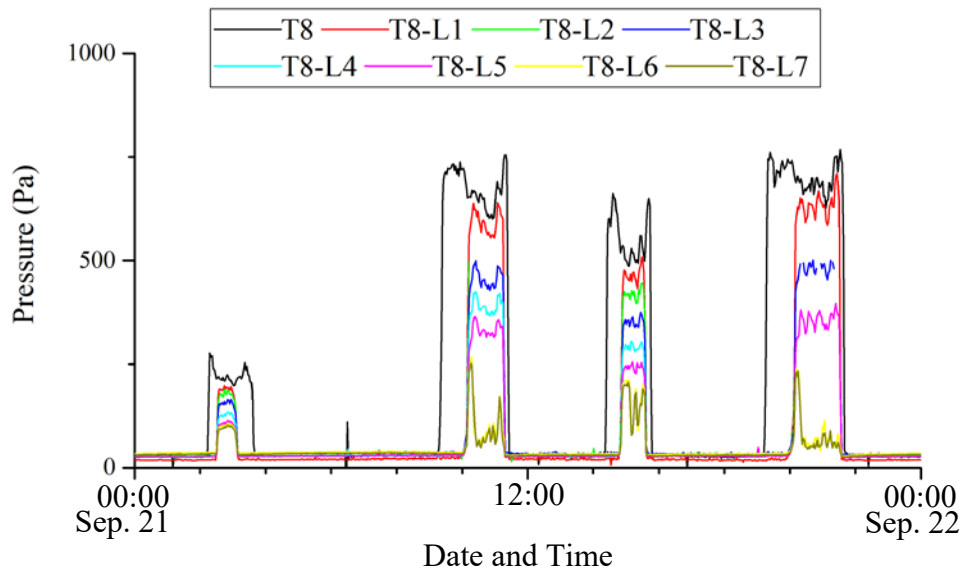


Figure 4-3 Plots of leakage coefficient. (a) Pipe numbers with head loss coefficient and the zone of influence; (b) Calculated K with different pipe number and head loss coefficient.

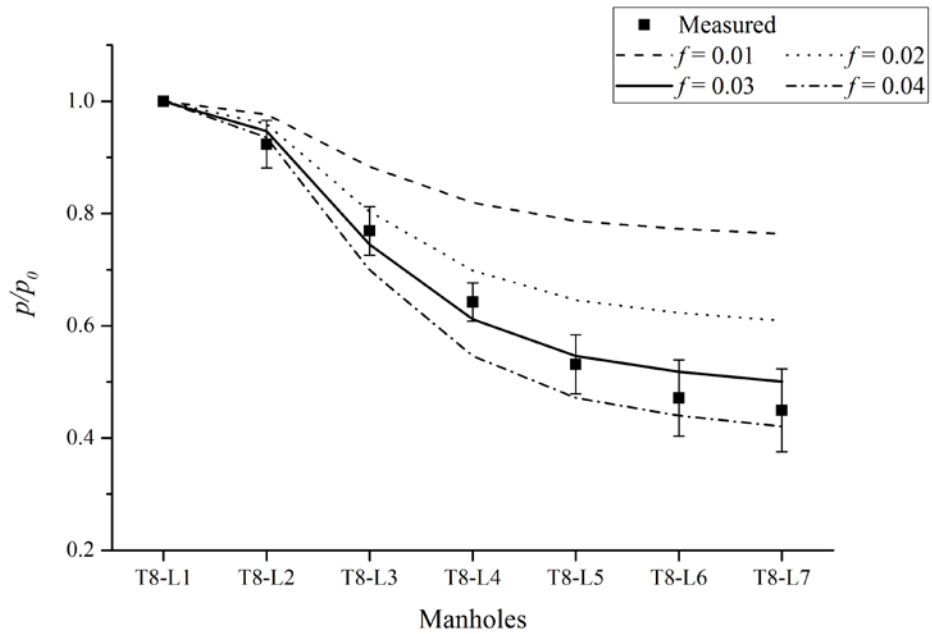
(a)



(b)



(c)



(d)

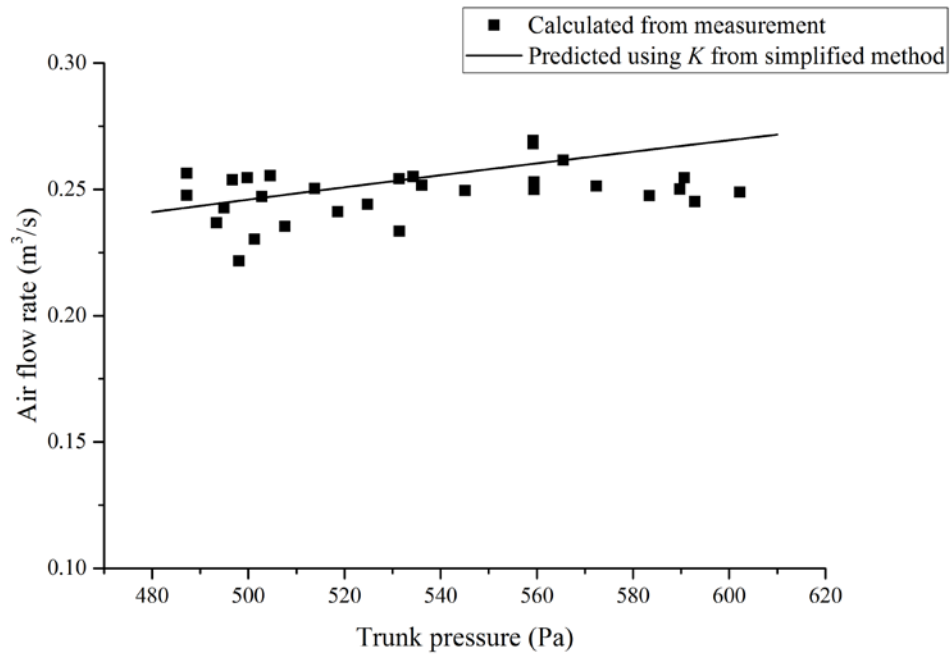


Figure 4-4 Measured and estimated pressure at T8 and its lateral connections. (a) Schematic of T8 and its lateral connection; (b) Measured pressure distribution at T8 to T8-L7; (c) Measured and predicted pressure distribution from T8 to T8-L7; (d) Comparison of air flow rate through T8 lateral from measurement and prediction.

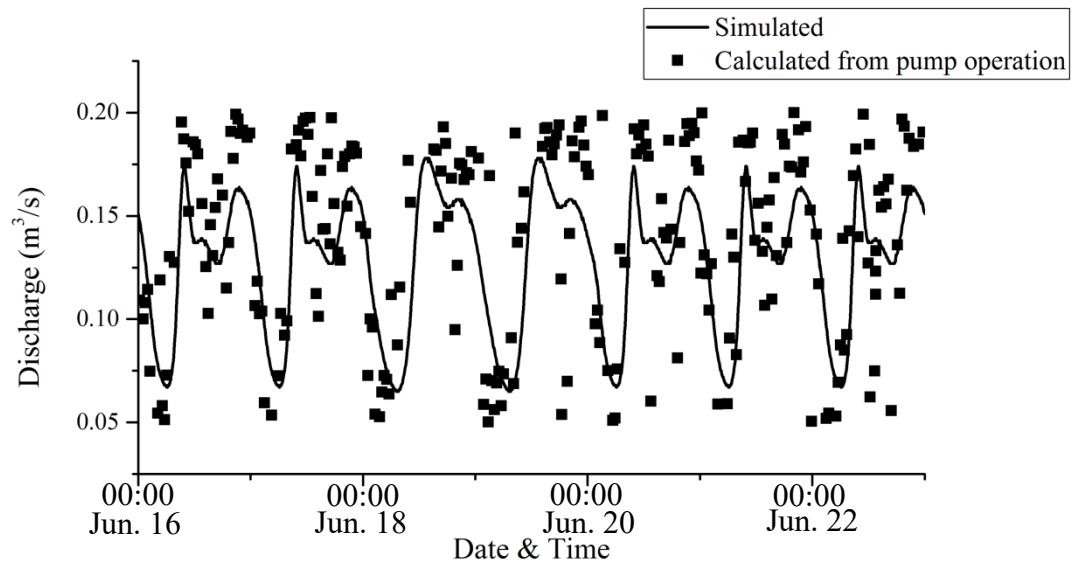


Figure 4-5 Comparison of simulated data and measured data.

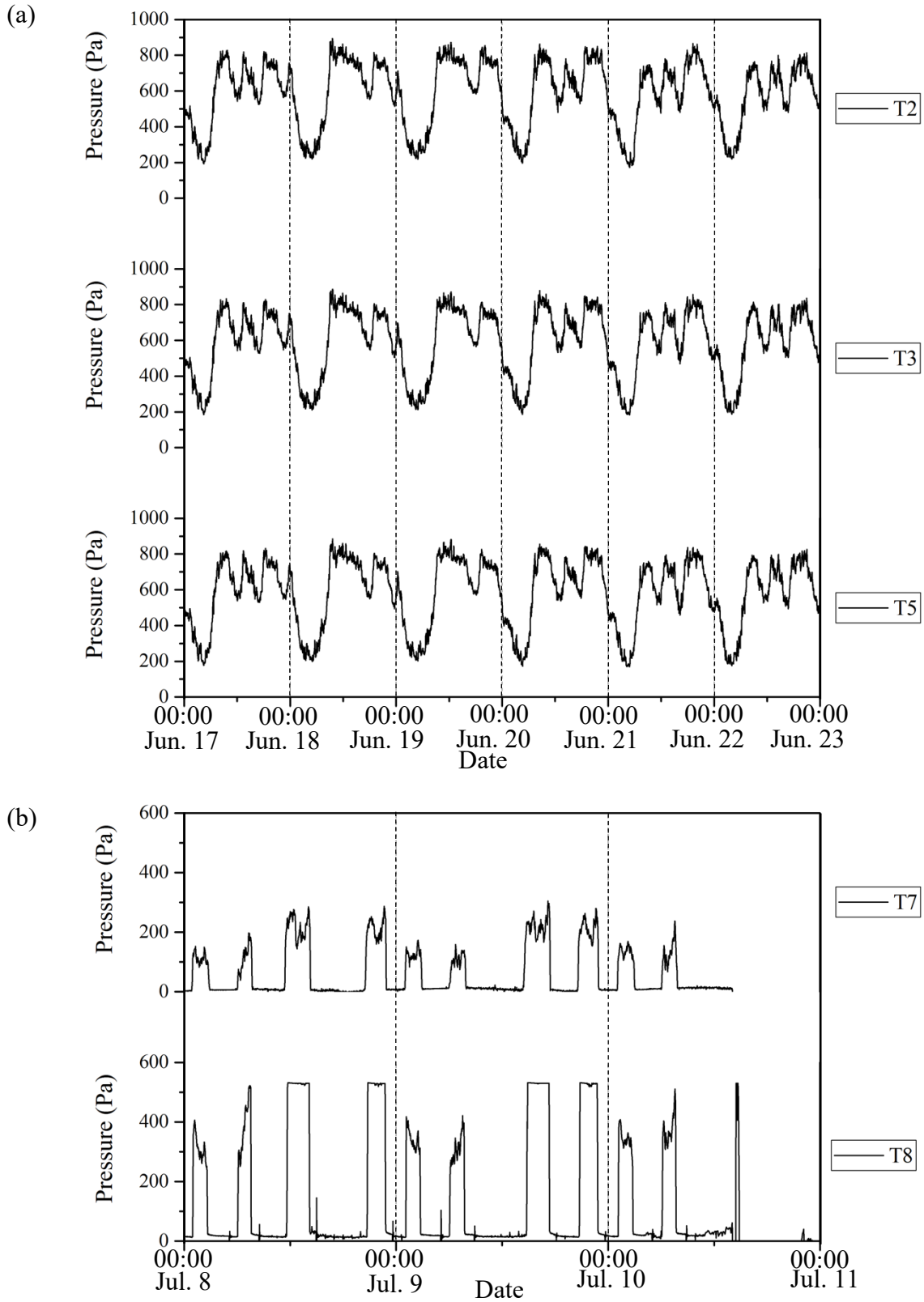


Figure 4-6 Plot of measured pressure at fieldwork. (a) Measured pressure between T2 and T5; (b) Measured pressure for T7 and T8.

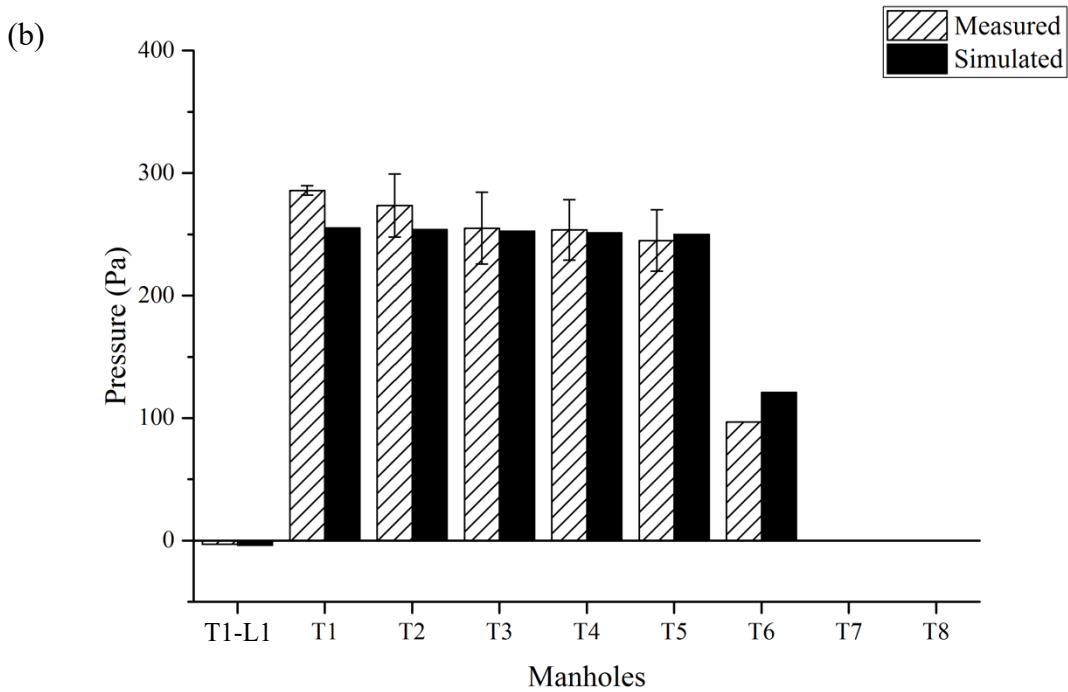
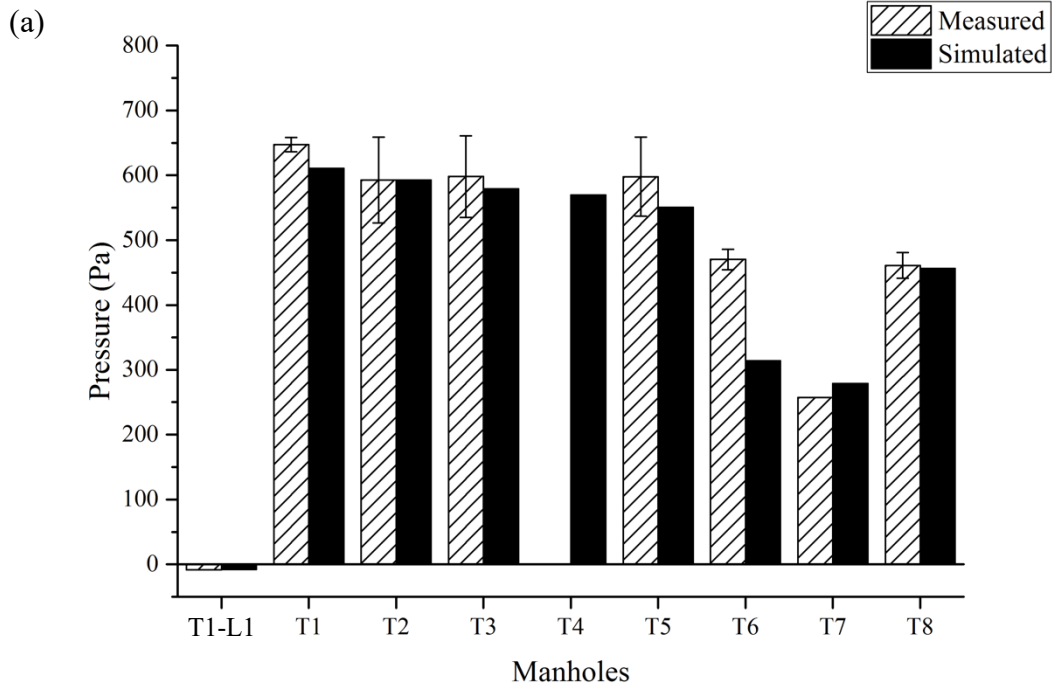


Figure 4-7 Pressure distribution along trunk lines. (a) Pressure distribution when T7 and T8 are pressurized (Case 1); (b) Pressure distribution when T7 and T8 are not pressurized (Case 2).

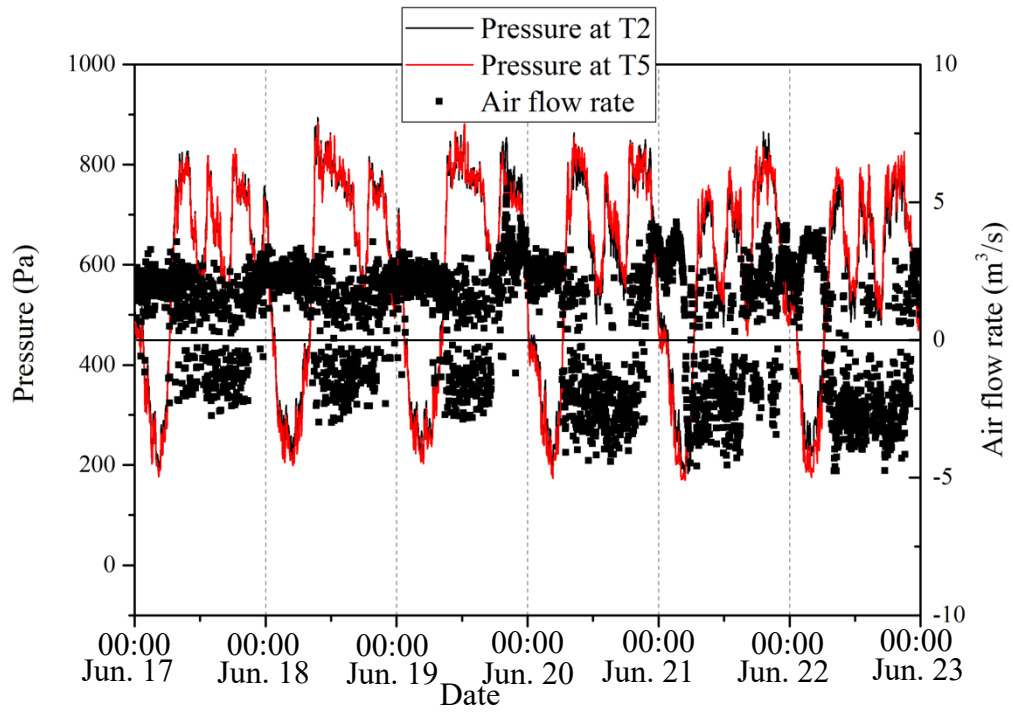


Figure 4-8 Estimated air flow rate from measured pressure data in the trunk line.

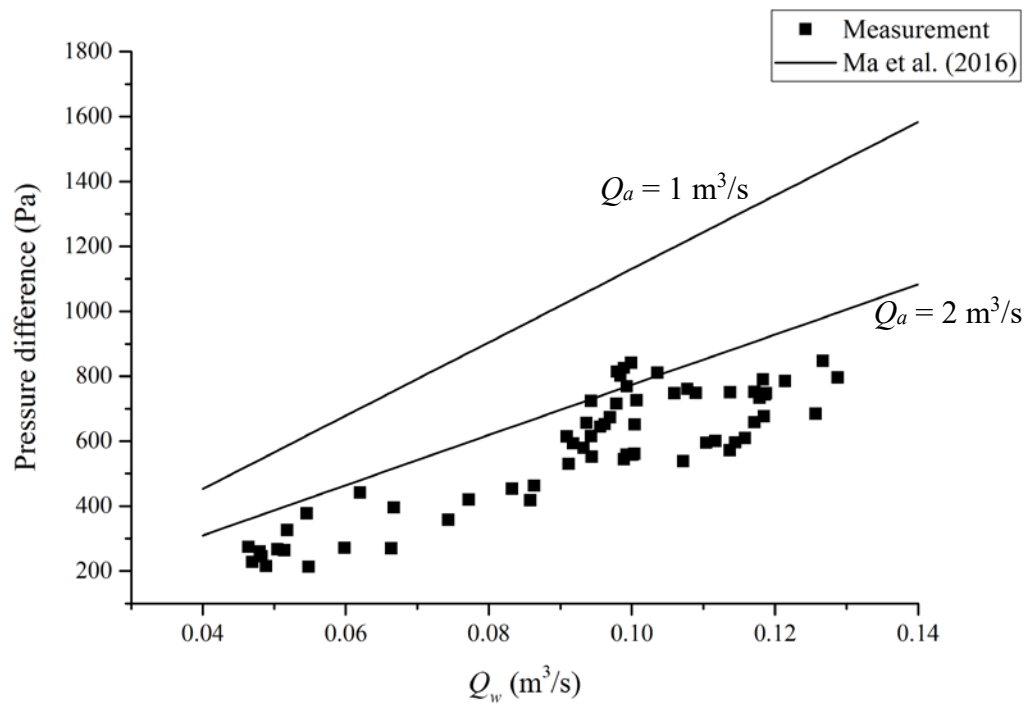


Figure 4-9 Plot of measured and predicted pressure change before and after the drop structure at T1-L1.

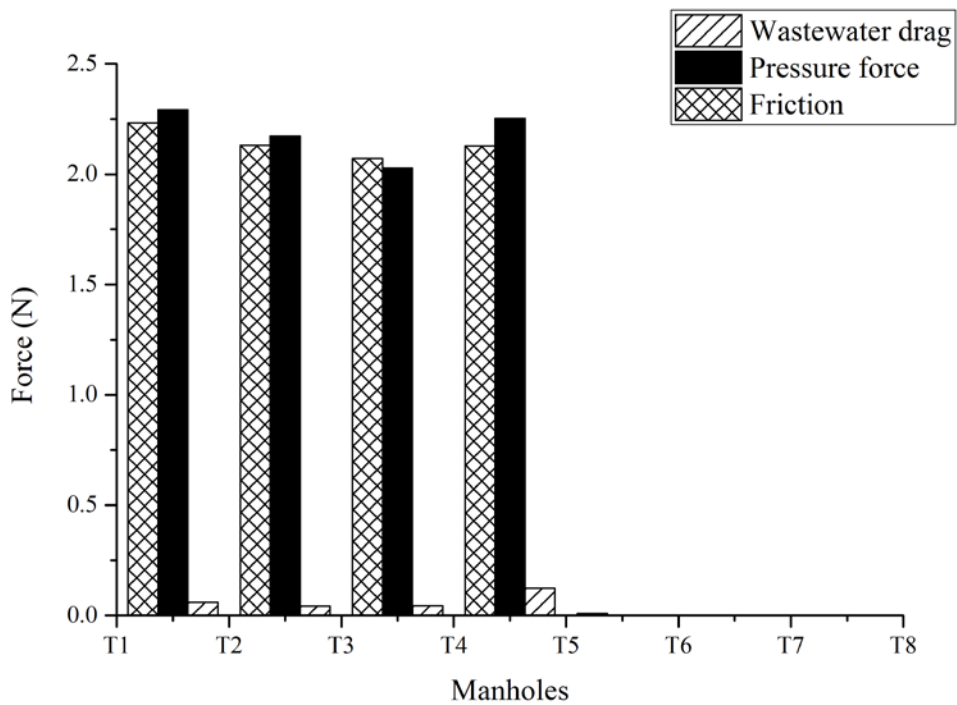
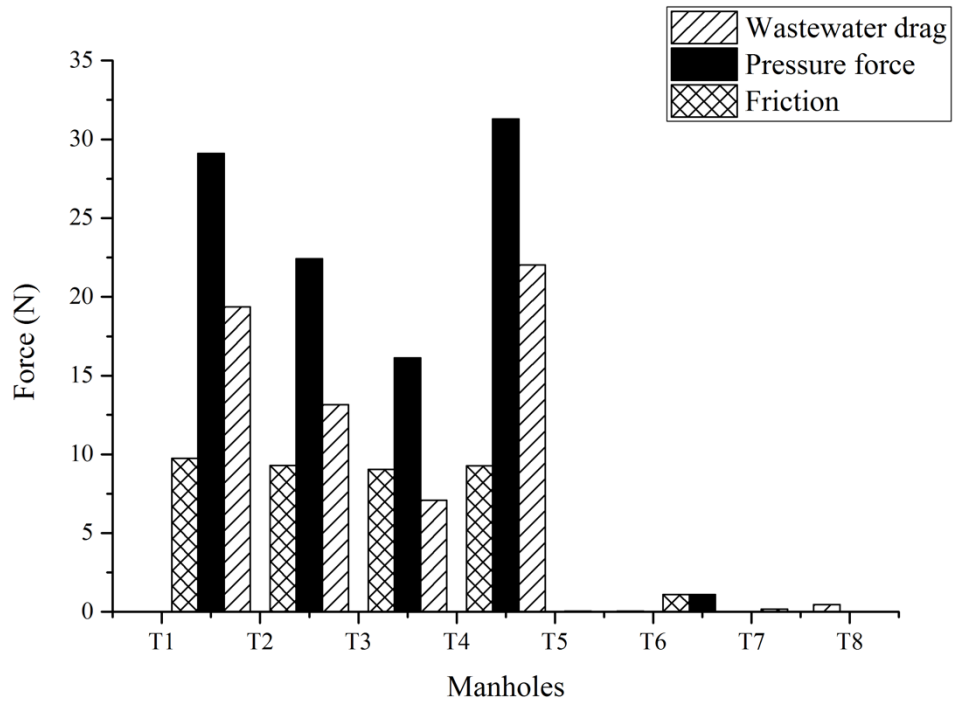


Figure 4-10 Plot of magnitude of forces in sewer pipes. Data plotted is the pipe between manholes in horizontal axis. (a) Case 1; (b) Case 2.

5. Numerical Study on the Mechanism and Mitigation of Storm Geysers *

5.1. Introduction

Geyser events in storm sewer systems are observed as the explosive ejection of air/water mixture from manholes during heavy rain storm events. They can induce public safety concerns such as manhole cover blow-off, local flooding, and even system failure (Li and McCorquodale, 1999; Shao, 2013; Huang, 2017). In Edmonton, AB, Canada, several geyser events were witnessed at one location, with the latest one shown in Figure 5-1 in July 2016. This geyser was estimated to be as high as 17 m, and the duration of the geyser was at least 1 minute (Youtube, 2018). It was estimated that the storm was more likely a 1:10 year storm, and the mitigation method is urgently needed for this site in order to prevent geysers due to the sensitivity of this location and public safety concerns.

Extensive studies on geysers in storm sewer systems have been reported in the literature. Vasconcelos and Wright (2011) concluded that it was the releasing of air from the entrapped air pocket in the pipe that triggered the geyser events. The triggers of geyser in the previous studies can be divided into two kinds: one is when an air pocket in the horizontal pipe reaches a vertical shaft (denote as riser in the current study) (Vasconcelos and Wright, 2009; Wright et al., 2008), and another one is when a rapidly filling bore propagates in a horizontal pipe and also reaches a vertical riser (Lewis 2011). Li and McCorquodale (1999), Vasconcelos and Wright (2011), and Wright et al. (2011a, b) systematically studied the generation of geysers including the movement

* The content of this chapter is being prepared and will be submitted as a journal manuscript.

of air pockets in horizontal pipes and found that the pressure head in the pipe was not necessary to be as high as the ground level. Cong et al. (2017), Chan et al. (2018), Huang et al. (2017), and Muller et al. (2017) studied the mechanism of geyser formation triggered by the air release experimentally and/or numerically. Muller et al. (2017) and Chan et al. (2018) confirmed that CFD is feasible to be used to simulate the geyser events.

The researchers mentioned above studied the flow of an air/water mixture out of a vertical riser connected directly to a horizontal pipe. However, in the sewer system analyzed in this study, there is a chamber beneath the riser, and the upstream and downstream pipes have different diameters and are not aligned. Also, all studies listed above treated the top of the riser as fully open to atmosphere except for Huang et al. (2017). In prototype storm sewer systems, the diameter of manhole cover is usually smaller than the one of manhole shaft. Therefore, it is more realistic to study geyser events in a riser with a smaller opening at the top end.

For geyser events triggered by a rapid filling surge, Zhou et al. (2011), Choi et al. (2014, 2016) developed CFD models simulating the releasing of an air pocket in a pipe. Based on the studies by Zhou et al. (2002), Li and Zhu (2018) numerically simulated the transient pressure in a horizontal pipe with an end orifice due to rapid filling flow and assessed the cushion effect of the air pocket on the peak pressure with different orifice diameters. All of these studies confirm that CFD can be applied on the detailed modelling of geyser events with an orifice plate.

Regarding to geyser mitigation methods, Wright et al. (2009) proposed two conceptual methods to mitigate geysers where the riser was originally directly connected to the horizontal pipe. One is

to add two 90° bends to the riser to create a near-horizontal section with the intent of separating the air phase from the liquid. Another one is to expand the diameter of the top part of the shaft. Lewis (2011) physically modeled these two mitigation methods in the laboratory and found that the additional horizontal pipe method was not effective in preventing a geyser event, and the diameter expansion method was successful in reducing the strength of the geyser only under certain conditions. Huang et al. (2017) proposed using an orifice plate at the riser top end to reduce the pressure in the horizontal pipe and the height of the geyser.

Currently the understanding of the mechanism of geyser and its mitigation methods is still limited. Geyser mitigation methods were only discussed qualitatively (Lewis, 2011), and only the orifice plates were tested in Huang (2017). To mitigate the geyser events, it is important to reduce the amount of water flowing out of the manhole. The pressure variation in the system and the amount of air transported downstream still need to be considered. For the mitigation methods in this study, the orifice plate is considered. The benching (See Figure 5-3c) and water recirculation chamber (WRC) (See Figure 5-3b) are considered. The benching is a changing diameter pipe installed in the chamber to connect the upstream and downstream pipes. The top of the benching has multiple openings for the releasing of air pocket trapped in the upstream pipe. The purpose of the benching is to lead the increased flow smoothly from the upstream to downstream pipe and reduce the vigorous motion of air/water mixture in the chamber. The WRC is a chamber installed beside the chamber and it is connected to the riser with an elbow. The bottom of the WRC is connected to the riser for water flowing back to the storm system. The purpose of the WRC is to redirect the air/water mixture from the upward direction to a horizontal direction towards the WRC. The

air/water mixture gets separated in the WRC where the air is released to the atmosphere and the water flows back to the riser.

To better understand the mechanism of geyser formation and to assess potential mitigation solutions of geysers, this study was conducted based on the configuration of the aforementioned problematic manhole. The upstream and downstream pipes of the model have different invert elevations and are connected to the riser through a chamber. A 3D transient computational fluid dynamics (CFD) model was developed. The detailed process of geyser formation (i.e. pressure variation and air/water interaction) was described and analyzed. Three geyser mitigation methods of water recirculation chamber (WRC), benching and orifice plate were employed to mitigate the geyser triggered by a surge front while the downstream pipe was nearly full. Orifice plates with different opening sizes were tested for the geyser triggered by an entrapped air pocket with water initially existing in the riser. The purpose of this study is to provide municipalities with feasible mitigation methods to address geyser issues in storm sewer systems.

5.2. Numerical methods

A commercial software Ansys CFX 16.2 was used to simulate the process of geyser events and the effectiveness of potential solutions to mitigate the geyser events. The software was known for its stability and efficiency on solving 3D CFD problems. Physical experiments were conducted prior to the numerical model for calibration and validation.

The schematic of the physical model is shown in Figure 5-2a. It is designed based on the aforementioned prototype connection in Edmonton. The upstream and downstream pipes have

diameters of 0.2 m and 0.28 m respectively and both have a length of 6 m due to the spatial limitation in the lab. The dimension of the chamber beneath the riser is 0.3 m × 0.3 m × 0.45 m. The diameter of the riser is 0.057 m and the length is 1.22 m. A circular overflow weir is installed in the downstream tank to control the water level in the downstream pipe. A removable tailgate is built between the downstream pipe and the downstream tank to adjust the flow capacity in the downstream pipe. Pressure is measured at the upstream pipe crown and 0.3 m upstream of the chamber and is denoted as PG1.

Figure 5-2b shows the geometry of the numerical model, of which the size is the same as the physical model. In the numerical model, the open space above the riser is modeled as a cylindrical block to better define boundary condition as atmospheric pressure. The boundaries of this cylindrical block and the top boundary of the downstream tank are defined as atmospheric pressure. The outlet boundary of the system is defined as a pressure outlet at the top opening of the circular weir in the downstream tank, as illustrated in Figure 5-2b. The pressure at the outlet boundary is set as 0.2 kPa across the outlet area to match the simulated water level in the downstream pipe and in the chamber with the measured one in the physical model. The pressure specified at the outlet boundary has no significant effect on the geyser process in this study according to a sensitive analysis, which indicates that a slight change in the outlet pressure does not affect the pressure variation during the geyser event in the simulation. In the current air-water two-phase model, air is defined as an ideal gas following the ideal gas law and is compressible. The water is considered to be an incompressible liquid.

In the simulation, the RANS model with $k-\varepsilon$ turbulence model was used to simulate the transient flow process, of which the Reynolds-averaged Navier-Stokes equations and the continuity equation are (Ferziger and Peric, 2002):

$$\frac{\partial(\rho\bar{u}_i)}{\partial x_i} = 0 \quad (5-1)$$

$$\frac{\partial(\rho\bar{u}_i)}{\partial t} + \frac{\partial}{\partial x_j}(\rho\bar{u}_i\bar{u}_j + \rho\overline{u'_i u'_j}) = -\frac{\partial\bar{p}}{\partial x_i} + \frac{\partial\bar{\tau}_{ij}}{\partial x_j} \quad (5-2)$$

where x_i or x_j ($i, j = 1, 2, 3$) is the Cartesian coordinate; \bar{u}_i, \bar{u}_j are the mean velocity components; u'_i, u'_j are the fluctuating velocity component; ρ is the density of fluid; t is time; and $\bar{\tau}_{ij}$ is the mean viscous stress tensor component; \bar{p} is the mean pressure.

The standard $k-\varepsilon$ turbulence model was used to model the turbulent flow. The model is the most commonly used turbulence model in CFD studies. Additional two equations are added to the governing equations for solving the turbulent kinetic energy and dissipation rate to close Equations 5-1 and 5-2. The $k-\varepsilon$ model is able to reflect the turbulent features without excessive computing requirements such as LES or DNS models. Therefore, this model is selected in the current numerical model.

For multi-phase flow modelling, the Volume of Fluid (VOF) method (Hirt and Nichols, 1981) was used. This method introduces an additional variable α to represent the volume fraction of each phase in each control volume. Its time-averaged governing equation is:

$$\frac{\partial\alpha}{\partial t} + u_i \frac{\partial\alpha}{\partial x_i} = 0 \quad (5-3)$$

For air-water two-phase flow, $\alpha = 1$ is that the control volume is completely filled with water, while $\alpha = 0$ means it is completely filled with air.

The mesh size for the geometry was determined by the mesh independence test. Local refinement and inflation layer were made at pipe walls and at the intersection of the pipe and the chamber as shown in Figure 5-3a. A total number of 760K nodes was generated. The mesh independence test was conducted by comparing the total volume of water flowing out of the riser during geyser events. The size of the mesh was decreased at a rate of 1.2 for a series sets of meshes. The results at 760K nodes showed that the variation of water volume was less than 10% for further mesh refinement at a smaller mesh size, which indicated that the mesh was in the independence region with 760K nodes. All runs were then conducted at this mesh level. The time step was initially set as 0.005s to maintain the Courant number at around 1.0 at this mesh level. Based on the sensitive analysis on time steps, a shorter time step of 0.001s was used when an abrupt change of monitored pressure in the riser occurs. The simulation was conducted using a Dell workstation with Intel Xeon E5-2450 processor. Four cores were used during one simulation and the computing time at this mesh level for each case was about one week.

Table 5-1 is a summary of all simulated cases. Experimental results were applied to validate the CFD models for Run A1, and A2. Run B1 to B3 tested different mitigation methods for geysers triggered by a surge front while the downstream pipe was nearly full. The orifice plate for Run B3 was installed in the riser at 0.76 m above the bottom of the riser. For Run C1 to C4, the orifice plate was located at the top of riser. C0 was for testing the flow pattern when the riser is fully sealed at the top based on the boundary condition of B2. For Run A1 and B1 to B3, the tailgate was removed from the numerical model so the downstream pipe was flowing in full flow capacity. For Run A2 and C0 to C4, the tailgate was partially closed which restrains the flow capacity in the

downstream pipe. The initial water slug height in the riser was 0.41 m from the bottom of riser. The initial inflow rate was 20 L/s and an air pocket of 0.071 m³ was predefined in the upstream pipe at 0.5 m upstream of the chamber.

The potential retrofitting methods of WRC and benching listed in Table 5-1 are shown in Figure 5-3b and 5-3c. The WRC shown in Figure 5-3b was built beside the riser at the top with a chamber. The chamber had a diameter of 0.3 m and a height of 0.45 m. It was connected to the original riser by a 90 degree bend and a pipe sloped 30 degrees. The top of the chamber was defined as atmospheric pressure. Figure 5-3c showed the benching installed in the chamber. The benching was a varying-diameter pipe segment connecting the upstream and downstream pipes. Five openings with diameters of 0.03 m each were cut at the top of the benching for ventilation.

5.3. Results and discussions

Scenario 1: Geyser generated by a surge front while downstream pipe was almost full

For Run A1, the flow in the downstream pipe was almost a full pipe flow with a thin layer of air. The numerical model diverged once the downstream was flowing full. However, the initial air flow rate in the downstream pipe was 0.9 L/s towards downstream and the initial water flow rate was 20 L/s. The flow in the upstream pipe was open channel flow with a water depth of 0.08 m. The initial water level in the chamber was nearly even with the crown of the downstream pipe, and no water was in the riser prior to the geyser event. In this case, the sudden increasing of water inflow rate would cause a rapidly filling flow with a surge front in the upstream pipe and induce geyser events, which was observed both in the physical experiment and in the numerical simulation. A steady state simulation with $Q_w = 20$ L/s was conducted prior to the transient simulation. For this

initial steady state, the measured water depth in the chamber of the physical model was 0.24 m, and the simulated pressure at the bottom of the chamber was 2657 Pa, which indicated a water depth in the chamber of around 0.27 m. The numerically simulated pressure showed an agreement with the measured data.

Figure 5-4a shows the simulated and measured pressures at PG1. The numerical simulation shows a similar pressure process to the physical measurement and agrees well with the measured one. Specifically, the pressure starts to increase sharply at $t = 2.0$ s, which is the moment when the water front reaches the chamber and completely chokes the downstream pipe as shown in Figure 5-4b. The simulated pressure reaches its maximum of 7.89 kPa at $t = 2.43$ s, which is about 6.3% lower than the measured 8.43 kPa at $t = 2.37$ s. During $t = 2.5$ s and 2.7s, the geyser event onsets when the air/water mixture ejects out of the riser and the simulated pressure decreases due to the release of the air/water mixture. After the geyser event, the simulated pressure in the upstream pipe starts to increase again because of the continuous incoming flow from the upstream. The pressure peak occurs again at 2.9 kPa, which is about 20% of difference compared to the measured 3.6 kPa. The major discrepancy between the experimental data and numerical results is that there is a pressure increase at the beginning of the simulation within 0.5 s. This is mainly due to the instability of the numerical model when dealing with a sudden change of the water inflow rate at the beginning of the simulation. However, the numerical and experimental processes after the onset of the geyser still agree well with one another, which indicates that the analysis of the geyser is acceptable even though there is a discrepancy before the onset of the geyser. Therefore, the numerical model can be used to simulate the geyser triggered by a surge front while the downstream pipe is almost full.

The oscillation of pressure in Figure 5-4 depends on the compression and expansion of the trapped air pocket during the geyser process. At $t = 2.25$ s, the simulated air volume in the system is about 10.7 L, which is composed of the air volume in the riser (3.41 L), and the air volume in the chamber and the upstream pipe (7.29 L). At $t + \Delta t = 2.26$ s, the air volume trapped in the system including the one in the riser and the one in the chamber and upstream pipe is 9.99 L. The amount of air released via the riser is 0.16 L given the air flow rate via the riser of 16.27 L/s during the period between $t = 2.25$ and 2.26 s. Therefore, the compression rate of the air pocket during the period between $t = 2.25$ and 2.26 s is 54.7 L/s. The pressure at PG1 at $t = 2.25$ s is 3864 Pa, which is the pressure inside the air pocket. Assuming that the air entrapped follows the ideal gas law where the production of pressure and volume is constant, the rate of pressure increase can be written as:

$$\frac{dp}{dt} = p_1 V_1 \left(-\frac{1}{V_2^2} \right) \frac{dV}{dt} \quad (5-4)$$

where p_1 is the initial air pressure, V_1 is the initial air volume, V_2 is the air volume after compression. The estimated air pressure increasing rate at $t = 2.25$ s is 22661 Pa/s, which is 13% lower than the simulated 26185 Pa/s. Therefore, it can be concluded that the increase of pressure is induced by the surge front which causes the compression of the air pocket.

Figure 5-4b is the simulated volume fraction of water for Run A1. At $t = 0$ s, the air in the upstream pipe and in the chamber is connected with the atmosphere via the riser. The surge front in the upstream pipe propagates at a speed of about 2.6 m/s, which is close to the physically measured 2.5 m/s. When the wave front arrives at the chamber, it impacts the opposite chamber wall and curves back ($t = 2.2$ s). With the continuous incoming flow, the water level in the chamber increases, and the pressure at PG1 also begins to increase at $t = 2$ s. In Figure 5-4a, the maximum pressure occurs at $t = 2.4$ s. After the air/water mixture is erupted out of the riser, pressure drops

and obtains its minimum around $t = 2.65$ s. It is believed that the air pocket in the system connects to the atmosphere after all water over the air pocket in the riser ejecting out of the riser. The upward motion of the air/water mixture induces a suction effect to the air pocket in the chamber and therefore the pressure decreases to a negative pressure. The air/water mixture then falls back to the riser and compress the air pocket and induces a second peak pressure.

Figure 5-5a is a plot of the variation of water flow rate with the pressure at PG1 and the area-averaged pressure at 0.01 m from the chamber across the upstream and downstream pipe. It can be seen that the change of water flow rate in the downstream pipe has a delay of about 1.2 s compared with the one in the upstream pipe. This delay is mainly due to the filling of the chamber and the eruption of air/water mixture via the riser. During this period, the pressure at PG1 increases and the geyser occurs at $t = 2.7$ s. At $t = 2.7$ s, and the water flow rate in the downstream pipe already reaches the final water flow rate at 85 L/s. A pressure peak appears at $t = 2.0$ s when the surge front reaches the downstream end of the chamber. The water flow rate in the downstream pipe increases temporarily mainly due to the arrival of the initial surge as can be seen from Figure 5-4b at $t = 2.0$ s. After $t = 2.5$ s, Figure 5-4b shows that the upstream pipe is almost full. Considering the invert elevation change of 0.18m (1.76 kPa), the head loss coefficient of the chamber after $t = 2.5$ s can be calculated as 0.958 calculated from the upstream velocity at 2.7 m/s.

At $t = 1.6$ s when the water flow rate into the chamber starts to increase rapidly, the water flow rate out of the chamber is 24.9 L/s. Considering a full pipe flow in the downstream pipe, the mass of water in the entire downstream pipe is 368.3 kg, and the velocity of water flow at 24.9 L/s is 0.40 m/s. The initial momentum of water at 24.9 L/s is 147.32 kg·m/s. The final momentum of full

pipe flow in the downstream pipe at 85 L/s is 508.94 kg·m/s. Based on the flow rate change at Figure 5-5a, assuming that it takes 1.2 s to reach the new steady state in the system with a flow rate of 85 L/s, the pressure needed to drive the water into the downstream pipe is 4894 Pa. Zhou et al. (2002) suggested that for the trapped air pocket, the maximum pressure inside the air pocket varies from 1.2 to 3 times of the driving pressure. The peak pressure estimated using this method is 5.9 to 14.7 kPa, which covers the simulated 8.5 kPa. Therefore, it can be concluded that the rapidly increased pressure in the chamber is mainly for driving the water flow into the downstream pipe.

For an entrapped air pocket, neglecting the friction and minor head loss, the governing equations for the pressure change in the air pocket are proposed by Zhou et al. (2002) and can be written as:

$$\frac{dV_a}{dt} = -AU \quad (5-5)$$

$$\frac{dU}{dt} = -g \frac{H-H_0}{x} - f \frac{U|U|}{2D} - \frac{U^2}{2x} \quad (5-6)$$

$$\frac{dH^*}{dt} = -k \frac{H^*}{V_a} \frac{dV_a}{dt} \quad (5-7)$$

where t is time, V_a is the volume of air, A is the cross-sectional area of the pipe, U is the velocity of the water front H is the pressure in the air pocket, H_0 is the initial pressure, and the asterisk indicates absolute pressure. Equations 5-5 to 5-7 can be solved by Matlab algorithms using a 4th order Runge-Kutta method. By substituting the aforementioned initial condition with the pressure (10.69 m), volume (10.7 L), and velocity (0.23 m/s) and solving the set of equations, the pressure head is oscillating at a period ranging from 0.49 s to 0.85 s given the initial x ranging from 0.01 m to 0.5 m, and it is in agreement with the simulated 0.6 s in Figure 5-4a, and therefore, it can state

that the simulated oscillation at PG 1 is induced by the compression and expansion of the air pocket trapped in the chamber and the upstream pipe.

Figure 5-5b shows the simulated air velocity and pressure averaged over the top of the riser. It can be seen that before geyser occurs, the air velocity at the top of the riser is around 15 m/s between $t = 0.5$ to 1.5 s, which is induced by the surge front in upstream pipe propagating towards chamber at a velocity of 2.6 m/s while the downstream is almost flowing full. The pressure averaged across the top of the riser shows a peak of 12.5 Pa at $t = 2.7$ s when the geyser happens which is believed as a result of the air/water mixture reaching the top of the riser.

The geyser height mainly depends on the peak pressure in the chamber top and the upward momentum of the air/water mixture induced by the pressure. For the sudden increase of the inflow rate from 20 to 85 L/s, Figure 5-4a shows that the peak pressure in the upstream pipe can reach up to 8 kPa which corresponds to a pure water column height of 0.8 m at the crown of the upstream pipe. Given that the height of the riser is 1.22 m and 0.05 m from the pipe crown to the chamber top, the pressure is not enough to push pure water column out of the riser. However, the geyser actually occurs, and the observed geyser height in the physical model is 0.15 m above the riser top opening which compares well with the simulated 0.2 m. This situation is consistent with the field result reported in Wright et al. (2011b), where the pressure head in the tunnel does not have to be as high as the ground level for a geyser to occur. For Run A1, the amount of water out of the riser is 0.21 L based on the simulation and the amount of air transported downstream is 13.6 L.

Scenario 2: Geyser triggered by an entrapped air pocket with water existing in the riser

For Run A2, physical experiment and numerical simulation were conducted with an initial water flow rate of 20 L/s and a final flow rate of 40 L/s. In the experiments, an air pocket was initially trapped in the upstream pipe by adjusting the tailgate while maintaining the water inflow rate at 20 L/s. The water inflow rate was then suddenly increased to 40 L/s and the increased water flow pushed the air pocket out of the upstream pipe through the riser and generate geyser. In the initial condition, the head of the air pocket in the upstream pipe were 0.5 m upstream of the chamber, the length and the total volume of the air pocket are 0.7 m and 0.071 m³, respectively. The initial pressure inside the air pocket was 2.7 kPa based on the physical measurement. The initial water slug height in the riser was 0.41 m from the top of the chamber. The measured and simulated pressure at PG1 is shown in Figure 5-6a. In the experiment, the measured pressure at PG1 increases rapidly from the initial 4.4 kPa to 13.3 kPa and causes the water slug to rise in the riser and jet out of riser. The pressure then decreases to a minimum at 1.7 kPa at 2s because of the mixture out of the riser and air cavity in the chamber. The pressure then increases back to about 11.6 kPa due to the continuously supplement of water from the upstream.

Figure 5-6a also shows that the simulated pressure at PG1 agrees well with the measured pressure especially before $t = 3$ s. The simulated maximum pressure is 13.8 kPa which is slightly higher than the measured 13.3 kPa. The minimum simulated pressure is 0.9 kPa and the minimum measured pressure is 1.7 kPa. The simulated maximum and minimum pressures are within 20% of the measured values. The onset of the maximum and minimum pressures for the numerical and the physical model is in accordance with each other. This study focuses only on the most severe geyser which happens before $t = 5$ s.

Figure 5-6b shows the water volume fraction of the simulation of Run A2. It can be seen that the water slug in the riser is pushed out of the riser by the air pocket from the upstream pipe starting after $t = 0.7$ s, and finishing at $t = 1.1$ s. Between $t = 1.1$ s to 3.0 s, no water flows out of the riser due to the lower pressure in the chamber after the shooting of the first geyser.

Figure 5-7a shows the water flow rates and the area-averaged pressures in the upstream and downstream pipes 0.01 m away from the chamber. It can be seen that the water flow rate in the downstream pipe initially increase rapidly. The maximum water flow rate occurs at $t = 0.51$ s and $t = 0.83$ s for upstream and downstream pipes respectively. The delay of 0.32 s is shorter than the one of Run A1. This is because between $t = 0.51$ and 0.83 s, the chamber is mostly filled with water with minor air intrusion as shown in Figure 5-6b. The area-averaged pressures in the upstream and downstream pipes show a similar pattern to the one at PG1. At $t = 0.7$ s, the head of air pocket reaches the riser and pushes the water slug in the riser upwards. From $t = 0.7$ s and onwards, due to the decrease of the pressure, the water flow rate decreases accordingly in the upstream and downstream pipes at $t = 1$ s.

The pressure oscillation at PG1 is mainly due to the compression and expansion of the entrapped air pocket. At $t = 0.3$ s, the simulated air pocket size and pressure is 65.50 L and 11424 Pa respectively. At $t + \Delta t = 0.31$ s, the air pocket size and pressure is 65.37 L, and 11600 Pa respectively. The water level increasing in the riser is 0.015 m which corresponding to a pressure change of 147 Pa. According to equation 5-4, the pressure increasing rate induced by the decreased volume of the air pocket can be predicted at 2182 Pa/s. For simulated pressure, considering the

pressure increased by the water level change in the riser, the actual simulated pressure increasing rate caused by the compression of the air pocket is 2885 Pa/s. Therefore, the increase of the pressure is provided by a combined effect of the compression of the air pocket and the increased water level in the riser.

Figure 5-7b shows the simulated air velocity and pressure at the top of the riser. The point velocity indicates the air velocity at the center of the riser. In generally, the air velocity and pressure increases before $t = 1.25$ s and then decreases. Both the air velocity and the pressure reach the maximum at $t = 1.25$ s which is slightly after the water slug in the riser is fully expelled. From the figure it can be seen that although the area-averaged air velocity only reaches slightly above 5 m/s, the air velocity at the center of the rise can reach up to 32 m/s at $t = 1.25$ s. The high air velocity is able to break the water slug that is already in the air (Muller et al., 2017). The water droplet can follow the air flow and reach an even higher elevation. The area-averaged pressure at the top of the riser shows two peaks. The first peak occurs slightly before $t = 1.06$ s where the water slug is just being pushed out of the riser. This pressure peak is mainly because of the compression of the air pocket. When the water slug is out of the riser, the air pocket is directly connected to open space with an atmospheric pressure, which induces a drop in pressure inside the air pocket as indicated by the area-averaged pressure at the top of the riser (Figure 5-7b).

From Figure 5-7b and 5-7a, it can be seen that the pressures at PG1 and in the upstream and downstream pipes increase before geyser happens due to the increased water inflow rate and the compression of air pocket. After air pocket reaches the riser and water slug initially in the riser starts to be pushed out, the pressure at PG1 decreases. During the geyser event, the water slug is

being pushed out of the riser between $t = 0.7$ to 1.1 s, the pressure at PG1 decreases. The water slug is fully expelled at $t = 1.06$ s where the pressure at the top of the riser reaches the maximum. The air pocket keeps expanding and the air velocity at the top of the riser increases until reaching its maximum value at 32.5 m/s at $t = 1.25$ s where the pressure at PG1 is the minimum. Afterwards, the entrapped air pocket keeps being expelled and the pressure at PG1 increases again to a steady state of slightly higher than 10 kPa. Using the energy equation and the simulated pressure in the upstream and downstream pipes, the minor loss coefficient of the chamber is estimated to be 0.961 based on the water velocity in the upstream pipe of 1.27 m/s, while it is 0.958 for scenario 1.

There are two major differences between the current and previous studies reported in the literature: (1) the existence of a chamber and the elevation change between the upstream and downstream pipes and (2) a sudden change in the inflow rate. In the studies of Muller et al. (2017), Biao et al. (2017) and Cong et al. (2017), there is no chamber connecting the riser and the horizontal pipe. The air pocket that pushes the water slug in the riser upwards can also directly travel downstream, which might reduce the strength of the geyser event. In the current study, the existence of a chamber and the elevation change of the invert of the upstream and downstream pipes make the riser the major exit for the air. The entrapped air pocket has less chance to be transported further downstream. For Vasconcelos and Wright (2011), Cong et al. (2017) and Chan et al. (2018), the air pocket was predefined with no change in the inflow rate. In reality, the hydrograph of a storm event tends to induce a rapid change in inflow rate, and it is the flow rate variation that drives the entrapped air pocket to a manhole where geyser happens. Therefore, the current study focuses more on prototype connection and can reflect the actual air/water interaction in prototype structures.

For Run A2, the simulation results suggest that the amount of water out of the riser before $t = 3\text{s}$ is 3.5L, which is much higher than that of the case with a surge front while the downstream pipe is almost full (Run A1). The air transported downstream is 0.32 L which is lower than that of Run A1. This is mainly because that the downstream pipe in Run A2 is initially full. With the existence of the chamber and the elevation change between the upstream and downstream pipes, little or no air tends to be transported downstream.

5.4. Geysers mitigation methods

Potential ways for mitigating geysers triggered by Scenario 1

Run B studies the effectiveness of three geysers mitigation methods: WRC, benching and orifice plate. Scenario 1 is selected for testing these mitigation methods due to its high pressure peak. Figure 5-8 shows the volume fractions of water when different mitigation methods apply to the case Run A1. For Run B1 with WRC (Figure 5-8a), the process of geysers event is similar to the one of Run A1. The surge wave front arrives at the chamber at $t = 2.0\text{ s}$ and curves backwards, which blocks the bottom of the riser. Once the air/water mixture is pushed into the riser and reaches its top, the air/water mixture flow is redirected by a 90° bends towards the chamber of WRC instead of directly shooting upwards at $t = 2.5\text{ s}$. Therefore, no visible geysers was observed. The air and water would be automatically separated in the WRC chamber due to their different densities. Air escapes from the WRC chamber via its top opening and water flows back to the sewer system via the riser as shown in Figure 5-8a at $t = 3.0\text{ s}$ and 4.0 s .

Figure 5-8b shows the geyser process when benching is installed (Run B2). It can be seen that no visible geyser happens. More specifically, at the beginning of the simulation, the upstream pipe is open channel flow. Air/water mixture can be seen at the connection of the chamber and the downstream pipe. When the wave front advances towards the chamber, the air pocket initially occupying the upper portion of the upstream pipe is compressed due to the small openings on the top of the benching. The water surface in the downstream pipe and benching is lowered from $t = 0.5$ to 2.0 s by this higher pressure caused by the compressed air pocket. At $t = 2.0$ s, the water front reaches the chamber. After $t = 2.5$ s, water inside the benching shoots out through the opening holes on the benching top and only a portion of the air/water mixture flows into the riser. The momentum of the air/water mixture is not enough to drive the mixture out of the riser. No geyser is observed in this case.

Figure 5-8c shows the geyser events when an orifice plate with an opening of $d_o = 0.5D_r$ is installed inside the riser and 0.76 m above the chamber top. Similar to the benching case, the water level in the chamber decreases at the beginning and then the downstream pipe gets choked at around $t = 2.5$ s. The upward motion of air/water mixture is blocked by the orifice plate and therefore, the geyser is mitigated by the orifice plate.

Figure 5-9 shows the simulated pressure variations at PG1 for the above cases compared with that of Run A1. It can be seen that the pressure pattern of the case with WRC (Run B1) at PG1 is similar to that of Run A1. The peak pressure for this run is 10 kPa, which is slightly higher than the one without WRC. The increased peak pressure is mainly due to the resistances caused by the

additional elbow and the related structures at the top of the riser. The water volume fraction (Figure 5-8a) shows that no water flows out of the riser and the geyser is mitigated.

For Runs B2 and B3, the installation of benching and the orifice plate increases the pressure at PG1 at early stage of the simulation ($t < 1$ s). This is due to the blockage of airways by the benching and the orifice plate. As the surge front propagates downstream to the chamber, the existence of the orifice plate or benching acts as obstruction and increases the head loss of air flow in the riser. Therefore, a higher pressure is needed to push the air out of the openings by the propagation of the surge wave front. The increased pressure is high enough to lower the water level in the benching and chamber as shown in Figure 5-8b and 5-8c respectively. The decreased water level in the benching and chamber connects the air pocket in the upstream and the downstream pipes. Air is likely to be transported downstream and might cause geyser events in other areas. During the period of geyser event between $t = 2$ s and 3.5s, the benching and the orifice plate can significantly reduce the peak pressure from the original 8 kPa to slightly less than 5 kPa and 0.8 kPa respectively. No visible geyser was observed during the simulation where the benching and the orifice plate were installed (Run B2, B3).

With regards to the air transported downstream in prototype sewer structures, the air itself does not cause issues so long as it can be safely discharged via a large vertical shaft. It is prudent to minimize the amount of air transported downstream to avoid potential geyser events in downstream areas. For the current numerical model, the air flow rate at 0.35 m downstream of the chamber was integrated with time to estimate total amount of air transported downstream. For Run A1, the total simulated amount of air transported downstream is 13.6 L. For the mitigation methods,

Run B1, B2, and B3 result in a total amount of air transported downstream of 14.1 L, 38.3 L, and 55.0 L, respectively. Comparing with the original geyser event without mitigation methods, mitigation methods of benching and orifice plate would potentially result in an increased amount of air transported downstream. The reason for this is that for a given flow condition, the air is either released via the riser or is transported downstream. By adding the benching or the orifice plate, the airway via the riser is restricted and therefore, more air tends to be transported downstream.

Table 5-2 is a summary of the performance of different geyser mitigation methods on the geyser triggered by a surge front while downstream pipe is almost full. It can be seen that the orifice plate is able to efficiently reduce the peak pressure during geyser event, and the amount of water flowing out of the riser. However, the air transported downstream due to the orifice plate is increased by 4 times. This may cause geyser issues at downstream locations.

Orifice plate for mitigating geyser triggered by Scenario 2

As discussed above, the orifice plate is able to decrease the pressure in the upstream pipe as well as mitigate the geyser event. The effectiveness of orifice plates is further examined in Run Cs with geyser triggered by scenario 2, including the riser fully sealed case and the orifices opening sizes of $d_o = 0.1D_r$, $0.2D_r$, $0.4D_r$, and $0.8D_r$. Figure 5-10a shows the simulated pressures at PG1. The pressure at PG1 increases slightly for Run C0, C1, C2, and C3 and the maximum pressures are 19.2, 16.6, 16.3 and 15.3 kPa respectively. Compared with the 13.9 kPa for Run A2, the pressure at PG1 is generally increased with the orifice plate. The smaller orifice corresponds a higher pressure. The pressure variation for Run C4 is similar to the one of Run A2. This is because the

orifice size for Run C4 is $0.8D_r$, which is close to the diameter of the riser and the effect of the orifice plate is minor in comparison with other orifice sizes.

Figure 5-10b shows the pressures in the middle of the riser and 0.76 m above the bottom of the riser. For C0, an oscillated pressure is observed. This is mainly due to the compression and expansion of the air pocket in the riser between the water surface in the riser and the sealed riser top. The length of the water slug decreases due to the film flow along the wall of the riser. After the length decreased to zero, the pressure then equals to the one at PG1. Figure 5-10b also shows a sharp peak for Run C1 to C3. This is primarily because of a sudden slamming of the water slug in the riser on the orifice plate. The figure suggests that the simulated peak pressures in the riser for Runs C1, C2, and C3 are 15.9 kPa, 105.8 kPa, and 36.6 kPa respectively and the peak pressure at PG1 after the transient flow happens is about 14 kPa. The ratios of peak pressure and driving pressure are 1.13, 7.55, and 2.61 respectively for Run C1 to C3. The pressure peak on the orifice plate is mainly induced by a sudden reduction of the rising velocity of the water slug suddenly impinging on it. The trend of the ratio of pressure agrees well with Zhou (2002) where the maximum peak pressure occurs at $d_0 = 0.2D_r$. However, this ratio is smaller than that reported by Li and Zhu (2018) mainly because the air pocket initially in the upstream pipe now below the water slug acts as a cushion and decreases the acoustic wave speed transferred to the water slug. Normalized by the peak pressure of C1, the ratios of the peak pressure are 6.65 and 2.30 respectively for Run C2 and C3.

Figure 5-11 shows the simulated movements of the free surface and the air/water interface during the geyser events. The origin of the coordinate Y is set at the top of the chamber. The figure shows

that except for Run C0 and C1, the simulated free surfaces overlap with each other and reach the top of the riser at around 0.7s where the sharp peaks of pressure are observed as shown in Figure 5-10b. For Run C0, the free surface in the riser oscillations corresponds well with the pressure shown in Figure 5-10b. It indicates that the oscillation of the free surface compresses and depresses the air pocket and therefore generates an oscillating pressure. The air/water interface for Run C0 rises and the velocity of the movement corresponds well with the Taylor Bubble velocity where the velocity can be written as $0.345\sqrt{gD_r} = 0.25 \text{ m/s}$. For Run C1, due to the limited capacity of air flowing out of the orifice, the free surface moves upward much slower than that of other cases and reaches the orifice plate at around 1.2s, which corresponds to the small pressure peak in Figure 5-10b. For air/water interface, Run A2 corresponds to the fastest moving air/water interface where the interface reaches the top of the riser at 1.04s. The Run C4 has minor differences compared with Run A2 mainly due to the limited effect of the orifice plate of $0.8D_r$. The air/water interface reaches the top of the riser at around 3.45s for Run C1, and C2, and 2.00s for Run C3.

Calculated from Figure 5-11, the velocities of the water slug when the free surface reaches the orifice plate are 0.4, 1.38, 1.4, and 1.68 m/s for Run C1 to C4 respectively. The model suggests that the velocities of the water slug after the impingement are 0.12, 0.18, 0.84 and 1.75 m/s respectively for Run C1 to C4, given the length of the water slug of 0.63, 1.073, 1.134, and 1.136 m respectively for Run C1 to C4 from Figure 5-11. The momentum changes for Run C1 to C4 are 0.42, 3.06, 1.79, and -0.22 kg·m/s respectively. The negative momentum change is mainly because that the effect of the orifice plate with $d_0 = 0.8D_r$ is small and the water slug is still accelerating due to the compressed air pocket. Normalized by the momentum change of Run C1, the ratios of momentum change for Run C2 to C3 are 7.28 and 4.26, respectively, which are generally in

agreement with the ratios of pressure discussed above. Therefore, it can be concluded that the peak pressure is mainly induced by the impingement of the water slug on the orifice plate.

Figure 5-12 shows the volume fraction of water at the vicinity of the orifice plate during the geyser event. The geyser height is defined as the maximum displacement of the water slug after it is ejected from the riser. Although the high velocity of air flow can blow the air/water mist up to 20 m/s, which corresponds to a height of 20 m, the change of morphology of water from continuous to dispersed droplets cannot be achieved by the current numerical model. Therefore, the maximum displacement of the water slug is used as a measure of the height of the geyser. In the numerical model, it is found that for Run C1 to C3, the water shoots out of the orifice plate continuously and maintains a geyser height similar to a circular jet. Therefore, the geyser height for Run C1, C2, and C3 can be treated as the height of the jet. Compared with the geyser height of 0.6 m for Run A2, the height of the geyser can be significantly reduced by the orifice plate. As can be seen from Figure 5-12, the maximum geyser height for Runs C1, C2, and C3 is 0.08 m, 0.11 m and 0.18 m respectively, while it can reach up to 0.6 m for Run C4 as the effect of the orifice plate is not significant.

For the amount of air transported downstream, geyser triggered by an entrapped air pocket with water existing in the riser tends to have a relatively small amount of air transported downstream compared with the one triggered by a surge front while downstream pipe is almost full. The numerical model suggests that in Run A2, the total amount of air transported downstream is 0.32 L, which is an order of magnitude smaller than that in Run A1. This is because in Run A2 the downstream pipe is initially pressurized and there is no air in the chamber. For Run C0, C1, C2,

C3, and C4, the total amount of air transported downstream before $t = 3$ s is 1.83 L, 1.63 L, 1.46 L, 1.13 L, and 0.36 L respectively. This is in agreement with the previous discussion where more restriction of air flow at the riser results in a higher amount of air transported downstream.

Table 5-3 is a summary of the performance of the orifice plates studied in this part. It can be seen that the installation of an orifice plate can significantly reduce the geyser height and the amount of water flowing out of the riser. Sealing the riser is able to mitigate the geyser event completely but generates the highest pressure in the upstream pipe. Compared with Run A2, using an orifice plate can reduce the geyser height by 87%, 82%, 70%, and 0% for Run C1 to C4 respectively. For the amount of water flowing out of the manhole, using orifice plate can reduce its value by 94%, 73%, 45%, and 5.4% for Run C1 to C4 respectively. For the air amount transported to the downstream, using an orifice plate can increase this value by 5.7, 5.1, 4.5 and 3.5 times of that of Run A2 for Run C0 to C3 respectively, while Run C4 slightly increases this air amount. The amount of air transported downstream is 1.83 L, 5.64 L, 4.42 L, 3.41 L, and 0.36 L for Run C0 to C4 respectively. Comparing with the initial air volume in the air pocket of 71 L, the air transported downstream is minor. The installation of an orifice plate increases the pressure in the upstream pipe slightly. However, for the pressure in the riser, the installation of an orifice plate induces water hammer-like pressure when the slug of water reaches the orifice plate.

5.5. Conclusions

A model scaled and simplified from the prototype storm sewer system was built and the rapid changed water inflow rate with two initial conditions. Different geyser mitigation methods were proposed and assessed numerically. A 3D transient numerical model was implemented to simulate

the geyser event triggered by a surge front while downstream pipe is almost full, and an entrapped air pocket with water existing in the riser. The current setup has a unique connection where the upstream and downstream pipes have an invert elevation drop of 0.18m and they are connected with the riser using a chamber. Possible ways to mitigate the geyser event were assessed. The following conclusions can be drawn:

1. The geyser can be generated by a surge front in the upstream pipe with an almost full downstream pipe. The chamber can be filled rapidly and the continuous compression of the air trapped in the chamber would induce pressure oscillation. The amount of air transported downstream in this scenario is relatively high but the water flowing out of the riser is relatively low.
2. The geyser generated by an entrapped air pocket with water existing in the riser can also generate Geysers. Compared with the geyser triggered by a surge front while the downstream pipe is almost full, the amount of air transported downstream is small.
3. There is no visible geyser observed in cases with the water recirculation chamber, benching and orifice plate for the geyser triggered by a surge front while the downstream pipe is almost full. The water recirculation chamber can induce a slight increase of pressure in the system and minor effect on the air amount transported to the downstream. Benching and orifice plate would decrease the pressure in the system and increase the amount of air transported downstream by 2 to 3 times compared to the system without retrofitting.
4. The installation of an orifice plate at the top of the riser can significantly reduce the geyser height and the amount of water out of the riser, but dramatically increase the dynamic pressure on the orifice plate up to 8 times of the regular one when the orifice size is $0.2D_r$. For the current setup, the installation of an orifice plate can also increase the air amount

transported to the downstream pipe by over 5 times of the regular one if the orifice diameter is smaller than 0.4 times the riser diameter, which may lead to geyser concerns in downstream areas.

The current CFD model simulated the air/water interaction during geyser events, but limitations still exist. The current model is unable to model the morphology change of water (i.e. from continuous phase to dispersed phase). Therefore, the actual height of the water droplets during geyser events can only be estimated using the air velocity. Discrepancies are also expected due to the limitation of geometry and the simplified boundary conditions compared to the prototype structure. The impact of the air transported downstream on the system is still to be further studied. Therefore, field monitoring is suggested for a better understanding of the mechanism of geyser happening in a storm water system.

Acknowledgement

The writers gratefully acknowledge the technical support professionally provided by Perry Fedun, the assistance in the laboratory experiments by Lucy (Lujia) Liu, and Jiachun Liu. The writers would also appreciate the financial support from Natural Sciences and Engineering Research Council (NSERC) of Canada, and Epcor.

List of symbols

D : pipe diameter.

D_r : riser diameter.

Q_w : water inflow rate from inlet.

\forall : is the volume of the air pocket.

d_o : diameter of the orifice plate.

p : pressure.

t : time.

\bar{u}_i : mean velocity components.

u'_i : fluctuating velocity component.

x_i ($i = 1, 2, 3$): Cartesian coordinate.

α : volume fraction of fluid.

δ : thickness of film flow around the riser.

μ_w : dynamic viscosity of water.

ρ : density of fluid.

$\bar{\tau}_{ij}$: mean viscous stress tensor component.

References

- Chan, S. N., Cong, J., and Lee, J. H. W. (2018). "3D numerical modeling of geyser formation by release of entrapped air from horizontal pipe into vertical shaft." *Journal of Hydraulic Engineering, ASCE*: 10.1061/(ASCE)HY.1943-7900.0001416.
- Choi, Y. J., Leon, A. S., and Apte, S. V. (2014). "Three-dimensional numerical modeling of air-water geyser flows." *World Environmental and Water Resources Congress*, June 1-5, Portland, Oregon.
- Choi, Y. J., Leon, A. S., and Apte, S. V. (2016). "A one-dimensional numerical model to predict pressure and velocity oscillations of a compressed air pocket in a vertical shaft filled with water." *World Environmental and Water Resources Congress*, May 22-26, West Palm Beach, Florida.
- Cong, J., Chan, S. N., and Lee, J. H. W. (2017). "Geyser formation by release of entrapped air from horizontal pipe into vertical shaft." *Journal of Hydraulic Engineering, ASCE*: 10.1061/(ASCE)HY.1943-7900.0001332.
- Ferziger, J. H., and Peric, M. (2002). "*Computational Methods for Fluid Dynamics*." 3rd edition, Springer, Berlin.
- Hirt, C. W. and Nichols, B. D. (1981) Volume of fluid (VOF) method for the dynamics of free boundaries. *Journal of Computational Physics*, 39: 201-225
- Huang, B. (2017) "Study on Geysers in Urban Drainage Systems". *PhD Thesis*, Nanjing Hydraulic Research Institute, Nanjing, China.
- Lewis, J. M. (2011). "A physical investigation of air/water interactions leading to geyser events in rapid filling pipelines." *PhD thesis*, University of Michigan, Ann Arbor, Michigan.
- Li, J., and McCorquodale, J. A. (1999). "Modelling mixed flow in storm sewers." *Journal of Hydraulic Engineering*, 125(11): 1170-1180.

Li, L., and Zhu, D. (2018). "Modulation of the transient pressure by air pocket in a horizontal pipe with an end orifice." *Water Science and Technology*, accepted.

Muller, K. Z., Wang, J., and Vasconcelos, J. G. (2017). "Water displacement in shafts and geysering created by uncontrolled air pocket release." *Journal of Hydraulic Engineering, ASCE*, 143(10): 04017043.

Shao (2013). "Two-dimensional hydrodynamic modelling of two-phase flow for understanding geyser phenomena in urban storm water system." *PhD thesis*, University of Kentucky, Lexington, Kentucky.

Youtube (2018). "Edmonton's Old Faithful." online: <https://www.youtube.com/watch?v=pvGfmwYvXtg> accessed 25 Feb. 2018

Vasconcelos, J. G., and Wright, S. J. (2009). "Investigation of rapid filling of poorly ventilated stormwater storage tunnels." *Journal of Hydraulic Research*, 47(5): 547-558.

Vasconcelos, J. G., and Wright, S. J. (2011). "Geysering generated by large air pockets released through water-filled ventilation shafts." *Journal of Hydraulic Engineering*, 137(5): 543-555.

Wright, S. J., Lewis, J. W., and Vasconcelos, J. G. (2011a). "Geysering in rapidly filling storm-water tunnels." *Journal of Hydraulic Engineering*, 137(1): 112-115.

Wright, S. J., Lewis, J. W., and Vasconcelos, J. G. (2011b). "Physical processes resulting in geysers in rapidly filling storm-water tunnels." *Journal of Irrigation and Drainage Engineering*, 137(3): 192-202.

Wright, S. J., Vasconcelos, J. G., Creech, C. T., and Lewis, J. W. (2008). "Flow regime transition mechanisms in rapidly filling stormwater storage tunnels." *Environmental Fluid Mechanics*, 8(5): 605-616.

Wright, S. J., Vasconcelos, J. G., Lewis, J. W., and Creech, C. T. (2009). "Flow regime transition and air entrapment in combined sewer storage tunnels." *Journal of Water Management Modeling*, R235-15: 237-256.

Zhou, F., Hicks, F. E., and Steffler, P. M. (2002). "Transient flow in a rapidly filling horizontal pipe containing trapped air". *Journal of Hydraulic Engineering, ASCE*, 128(6): 625-634.

Zhou, F., Hicks, F. E., and Steffler, P. (2004). "Analysis of effects of air pocket on hydraulic failure of urban drainage infrastructure." *Canadian Journal of Civil Engineering*, 31: 86-94.

Zhou, L., Liu, D., and Ou, C. (2011). "Simulation of flow transients in a water filling pipe containing entrapped air pocket with VOF model." *Engineering Applications of Computational Fluid Mechanics*, 5(1): 127-140.

Table 5-1 List of experiments

Run series	Initial inlet Q_w	Final inlet Q_w	Outlet BC	Initial water level in riser ³	Tailgate opening	Mitigation methods
A1 ¹	20 L/s	85 L/s	0.2 kPa	No water in riser	Fully open	No mitigation
A2 ¹		40 L/s		0.41 m	0.055 m	No mitigation
B1	20 L/s	85 L/s	0.2 kPa	No water in riser	Fully open	WRC
B2						Benching with openings
B3 ²						OP: $d_o = 0.5D_r$
C0 ⁴	20 L/s	40 L/s	0.2 kPa	0.41 m	0.055 m	OP: $d_o = 0D_r$
C1						OP: $d_o = 0.1D_r$
C2						OP: $d_o = 0.2D_r$
C3						OP: $d_o = 0.4D_r$
C4						OP: $d_o = 0.8D_r$

1: Cases validated by physical experiments; 2: Orifice plate in the riser and 0.76m above the bottom of riser; 3: Measured from the bottom of riser; WRC: Water recirculation chamber; OP: Orifice plate; d_o : the diameter of orifice drilled in the center of orifice plate; 4: Riser completely sealed at the top.

Table 5-2 Summary of different geyser mitigation methods based on CFD model.

Run	Mitigation methods	Maximum pressure at PG1 (kPa) ¹	Amount of water flowing out of riser (L)	Amount of air transported downstream (L)
A1	No mitigation	8.0	0.21	13.6
B1	WRC	10.0	No geyser	14.1
B2	Benching	5.0	No geyser	38.3
B3	OP: $d = 0.5D_r$	0.8	No geyser	55.0

1: during geyser events.

Table 5-3 Summary of the performance of orifice plates based on CFD model.

Run Series	Orifice size	Maximum geyser height (m) ¹	Maximum pressure at PG1 (kPa)	Maximum pressure in riser (kPa) ²	Amount of water flowing out of riser (L)	Amount of air transported downstream (L)
A2	D_r	0.60	13.9	12.2	3.50	0.32
C0	$0D_r$	0	19.2	19.2	0	1.83
C1	$0.1D_r$	0.08	16.6	15.9	0.19	5.64
C2	$0.2D_r$	0.11	16.3	105.8	0.94	4.42
C3	$0.4D_r$	0.18	15.3	36.6	1.94	3.41
C4	$0.8D_r$	0.60	13.9	12.5	3.31	0.36

1: measured from the top of the riser; 2: measured in the riser at 0.76m above the top of the chamber.



Figure 5-1 Geyser event on 27th July 2016 at intersection of 30 Ave. and Gateway Blvd., Edmonton, AB, Canada. (Youtube, 2018)

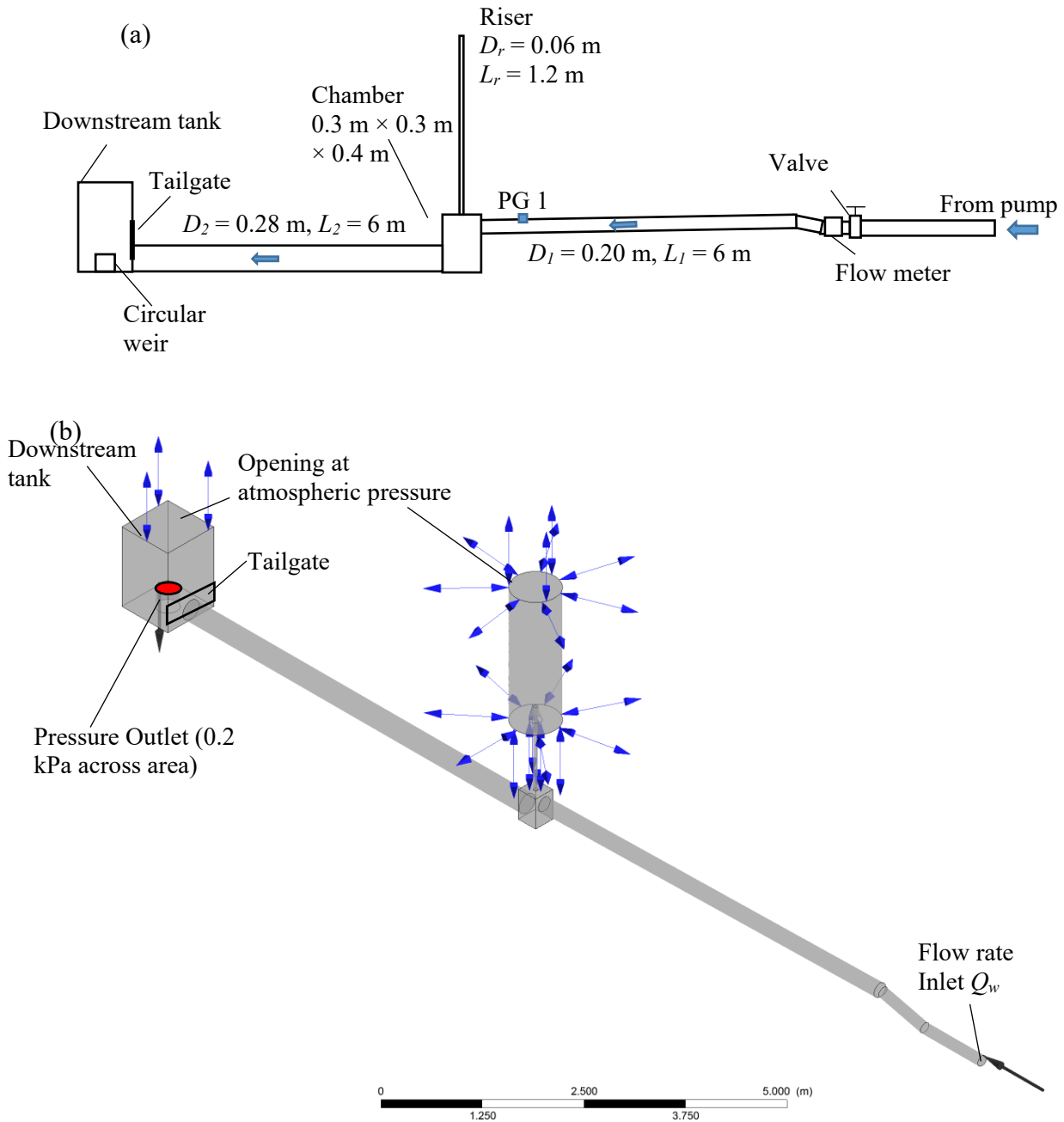


Figure 5-2 Geometry of the numerical model. (a) Schematic of the physical model (Drawing not to scale); (b) Schematic of the geometry and boundary conditions of the numerical model.

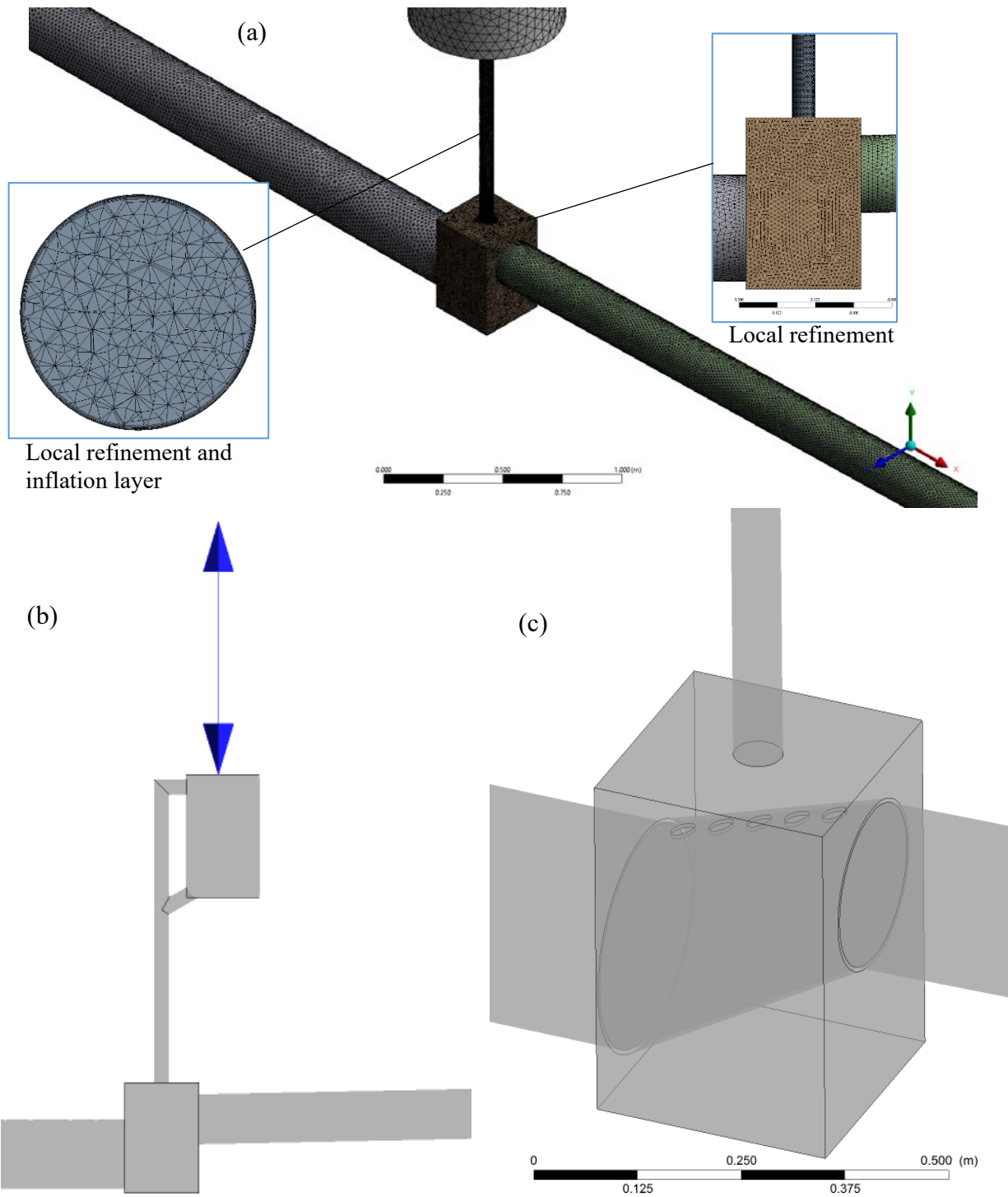
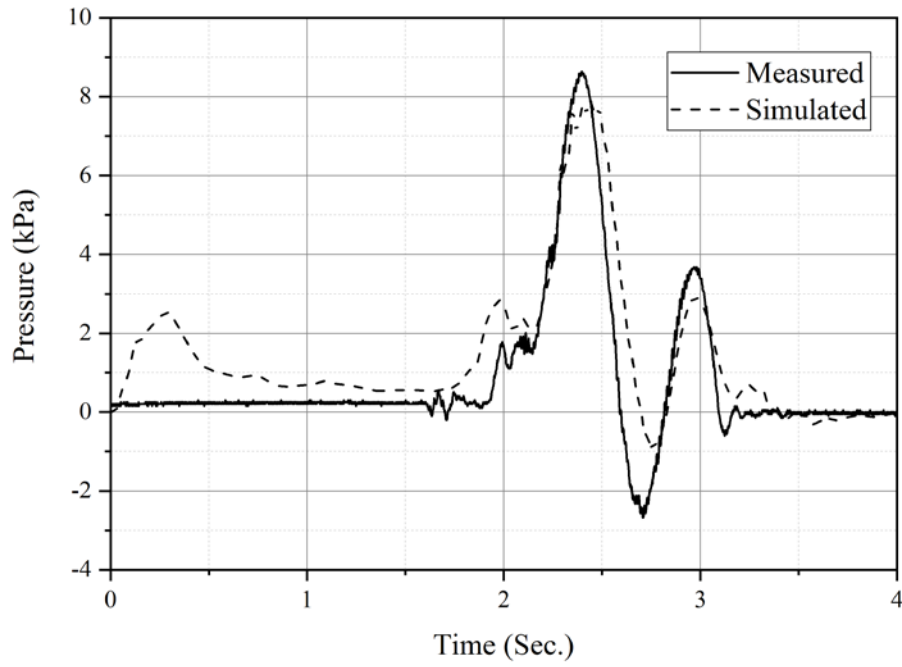
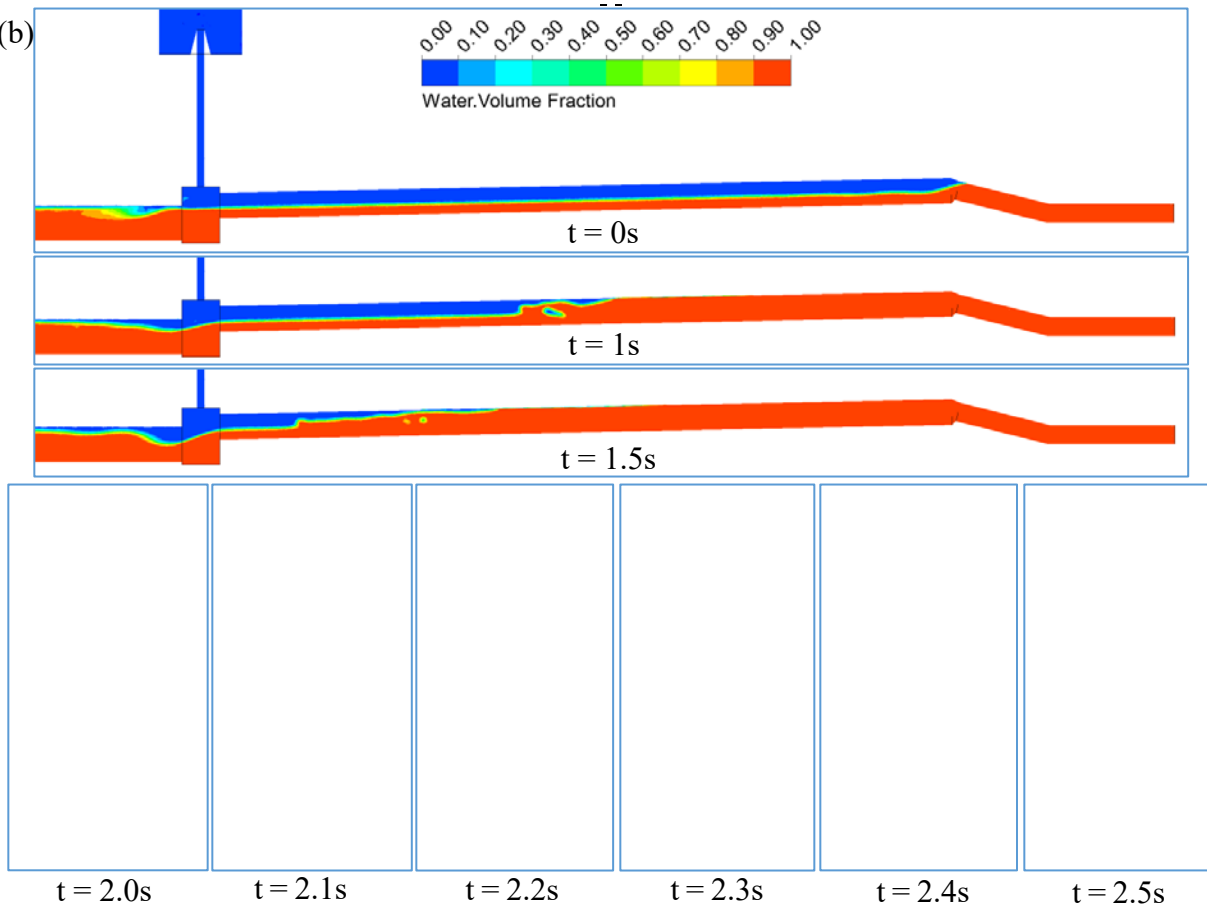


Figure 5-3 Additional information of the numerical model. (a) Mesh refinement and inflation layer; (b) Model with water recirculation chamber (WRC) connected to the riser; (c) Model with benching (with five openings on its top wall) in the chamber.

(a)



(b)



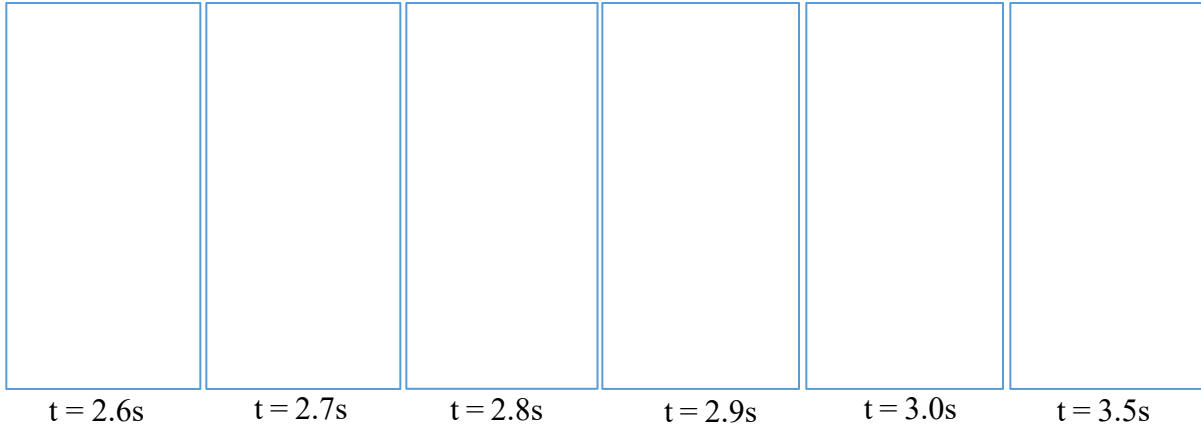


Figure 5-4 Simulated geyser event triggered by a surge front while downstream pipe is almost full pipe flow. (a) simulated and measured pressure at PG1; (b) simulated volume fraction of water.

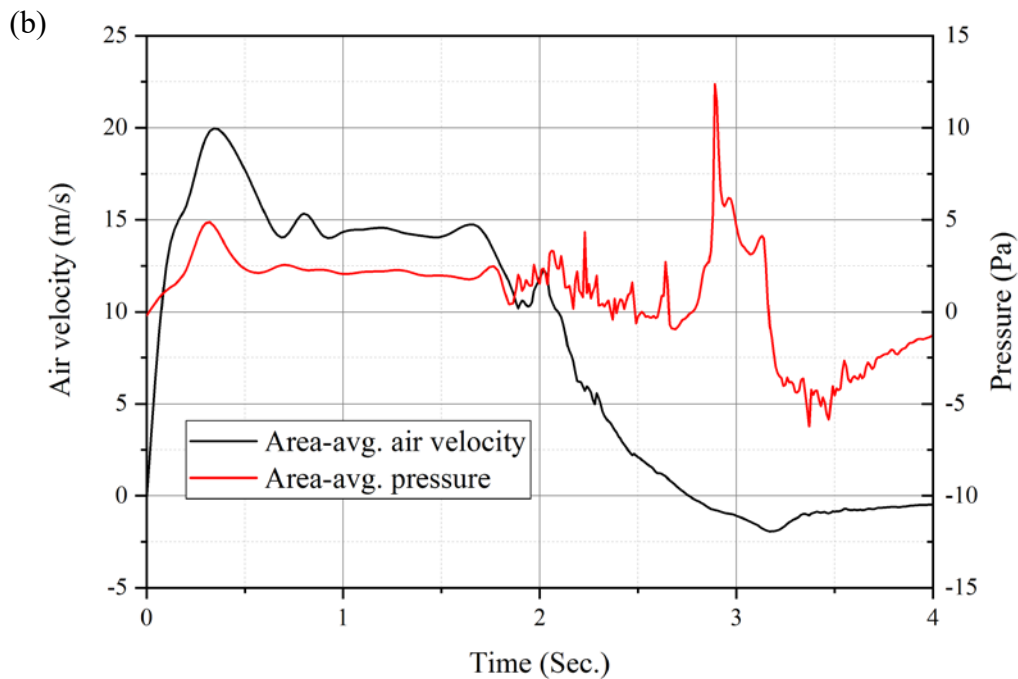
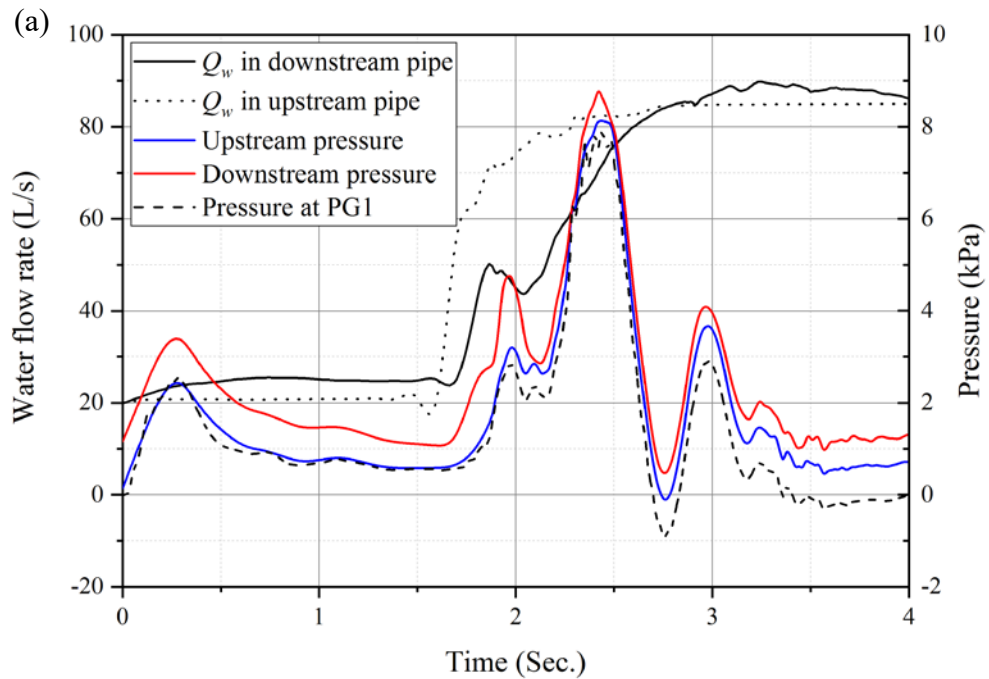
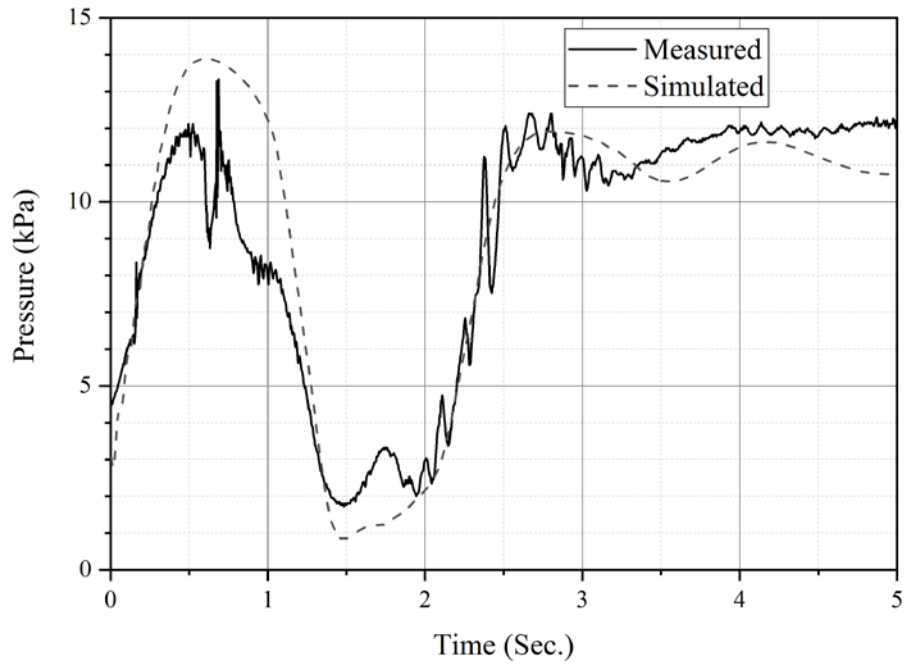
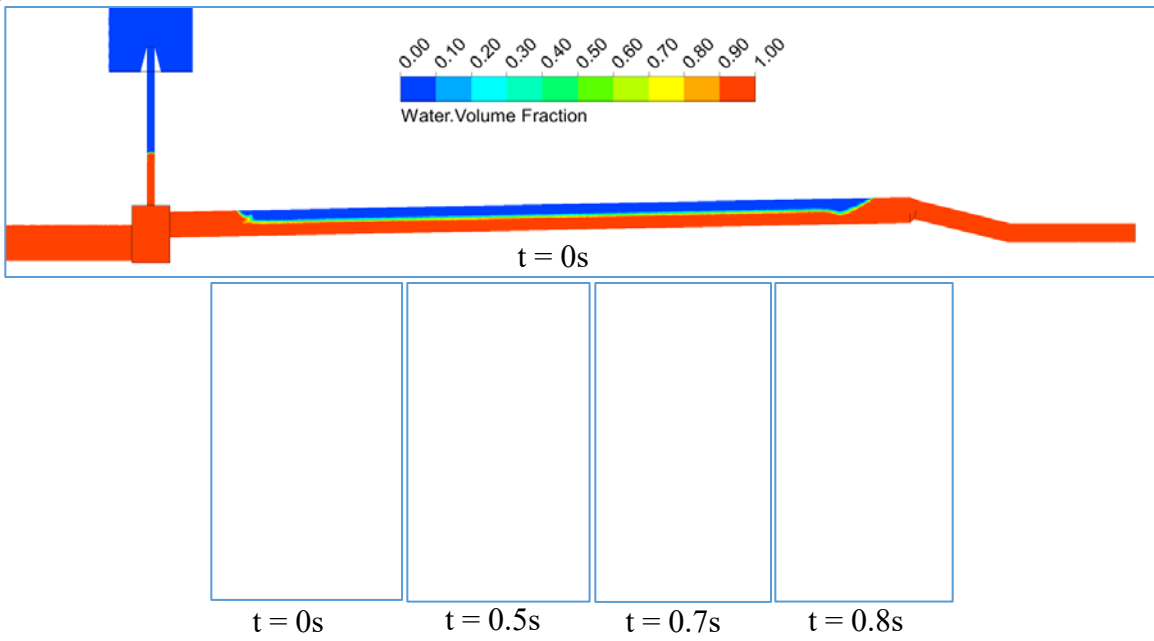


Figure 5-5 Plot of detailed flow conditions for geyser triggered by a surge front while downstream pipe is almost full pipe flow. (a) Simulated water flow rate and area-averaged pressure at 0.01 m upstream and downstream of the chamber; (b) Simulated air velocity and pressure area-averaged across the top of the riser.

(a)



(b)



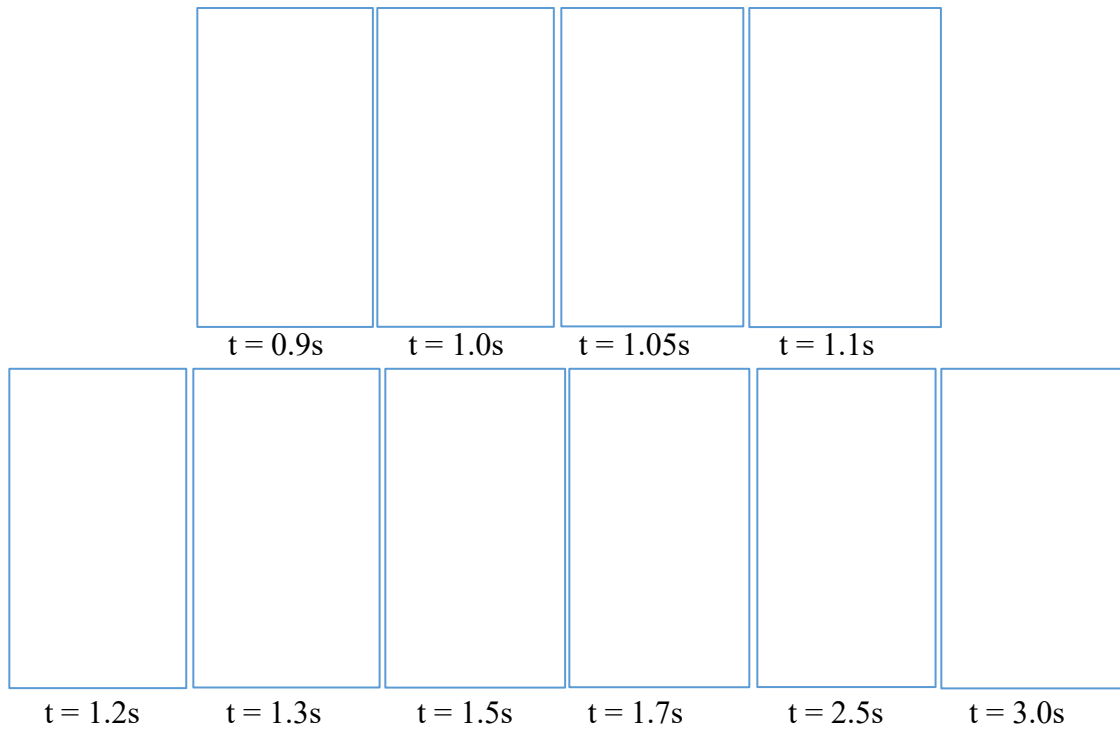


Figure 5-6 Simulated geyser event triggered by an entrapped air pocket with water existing in the riser. (a) simulated and measured pressure at PG1; (b) simulated volume fraction of water.

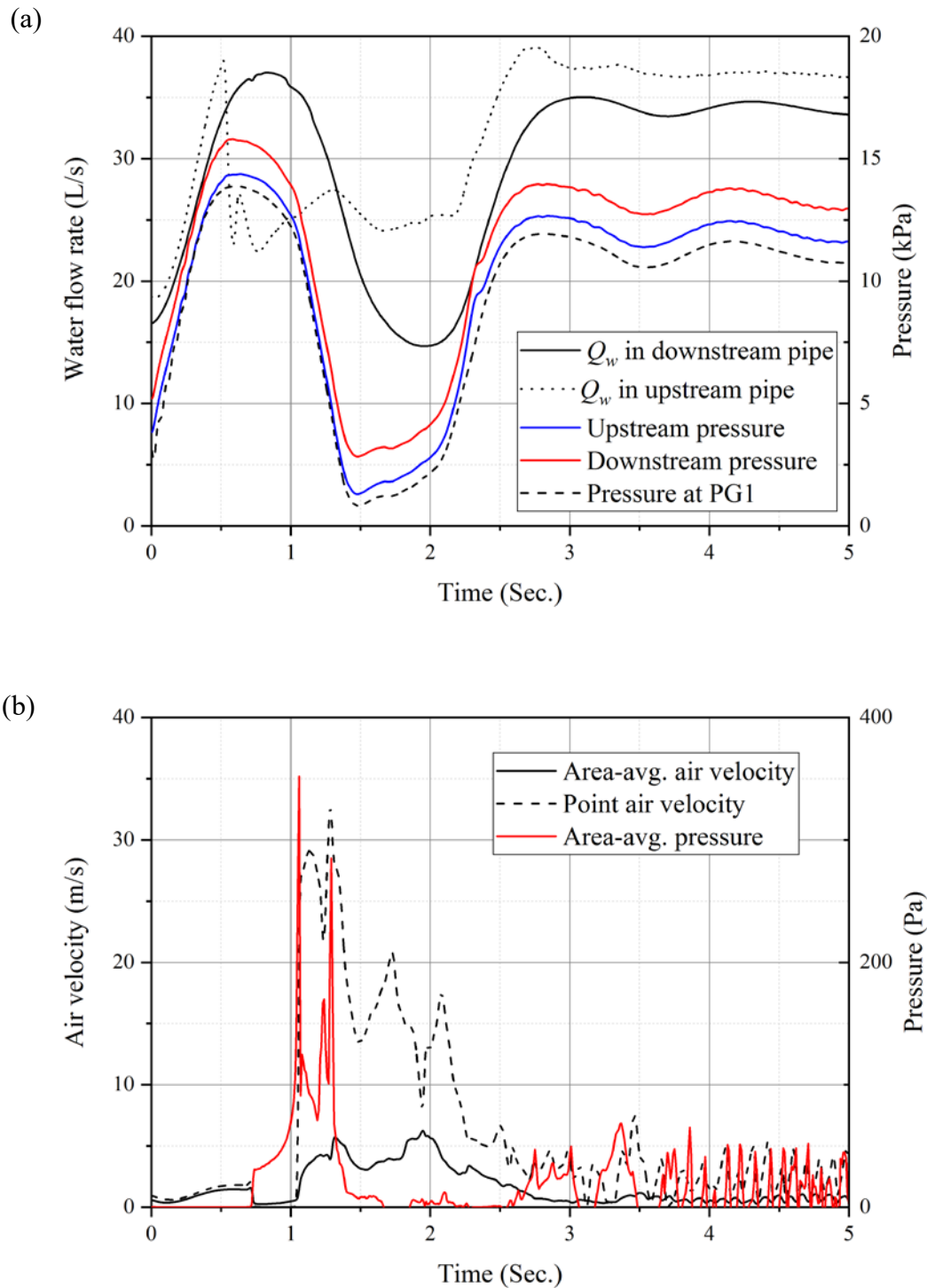
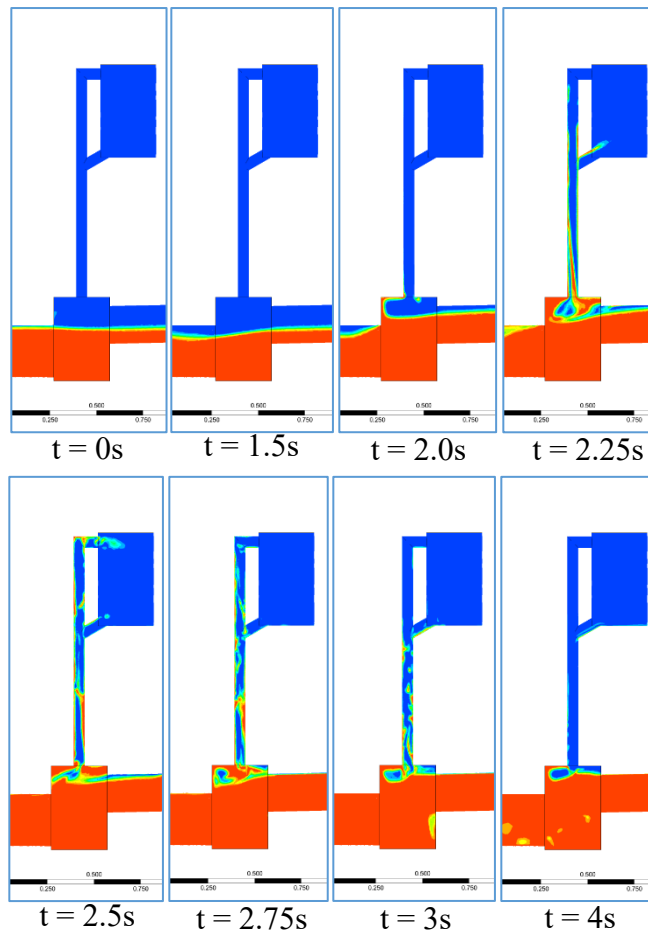
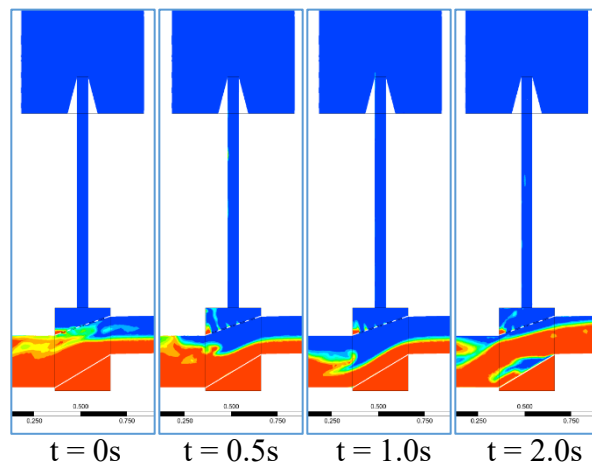


Figure 5-7 Plot of detailed flow conditions for geyser triggered by an entrapped air pocket with water existing in the riser. (a) Simulated water flow rate and area-averaged pressure at 0.01 m upstream and downstream of the chamber; (b) Simulated air velocity and pressure area-averaged across the top of the riser.

(a)



(b)



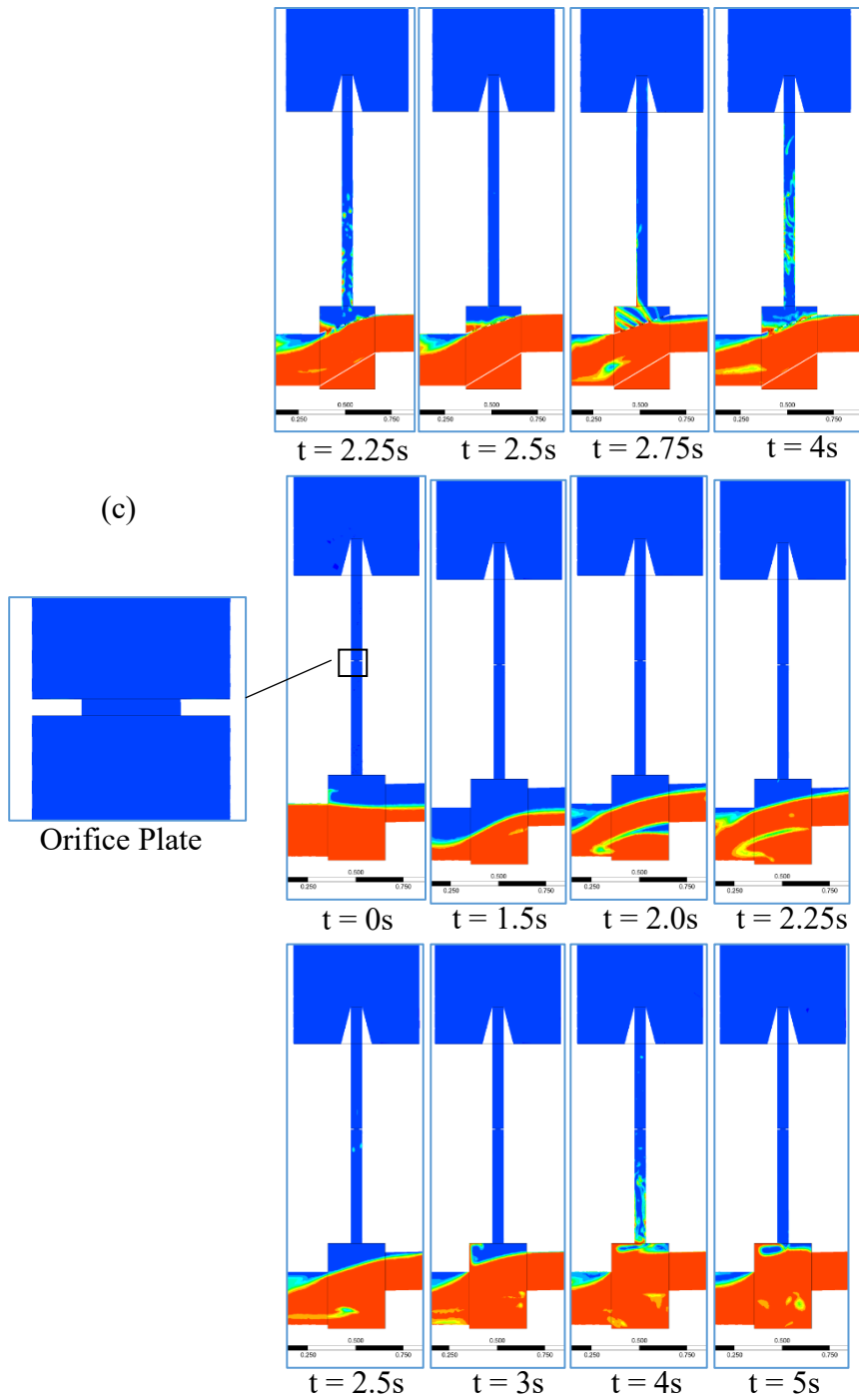


Figure 5-8 Simulated volume fractions of water for different mitigation methods on geyser triggered by a surge front while the downstream pipe is almost full pipe flow. (a) Water recirculation chamber; (b) Benching with openings; (c) Orifice plate ($d_o/D_r=0.5$).

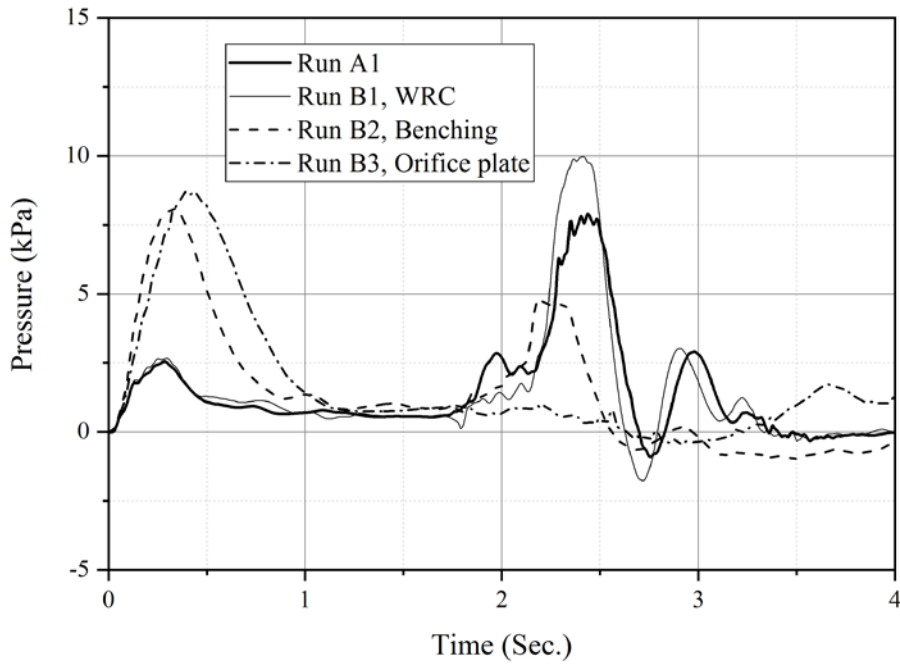
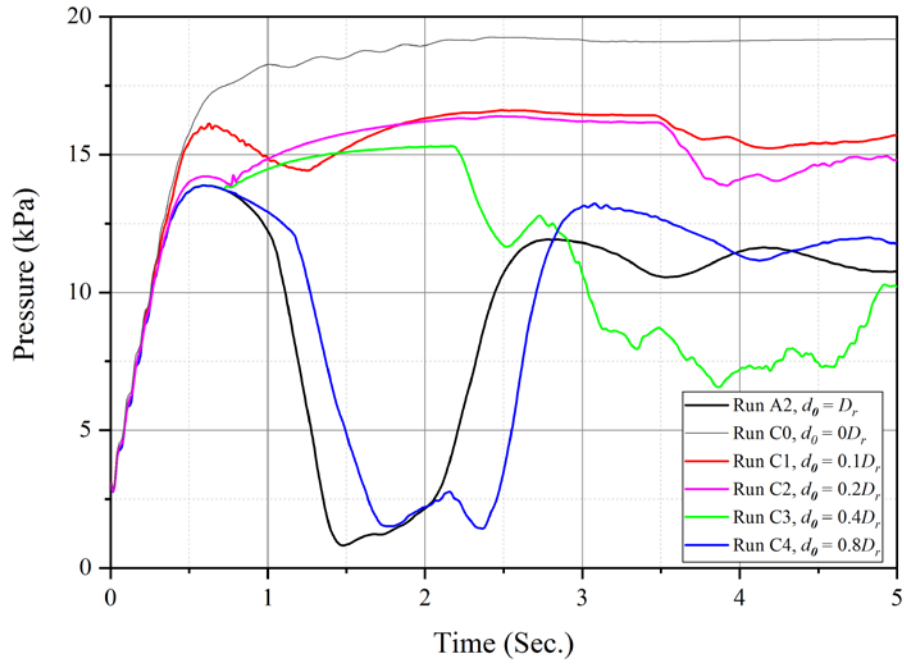


Figure 5-9 Simulated pressures at PG1 for geyser mitigating methods with geyser triggered by a surge front while downstream pipe is almost full pipe flow.

(a)



(b)

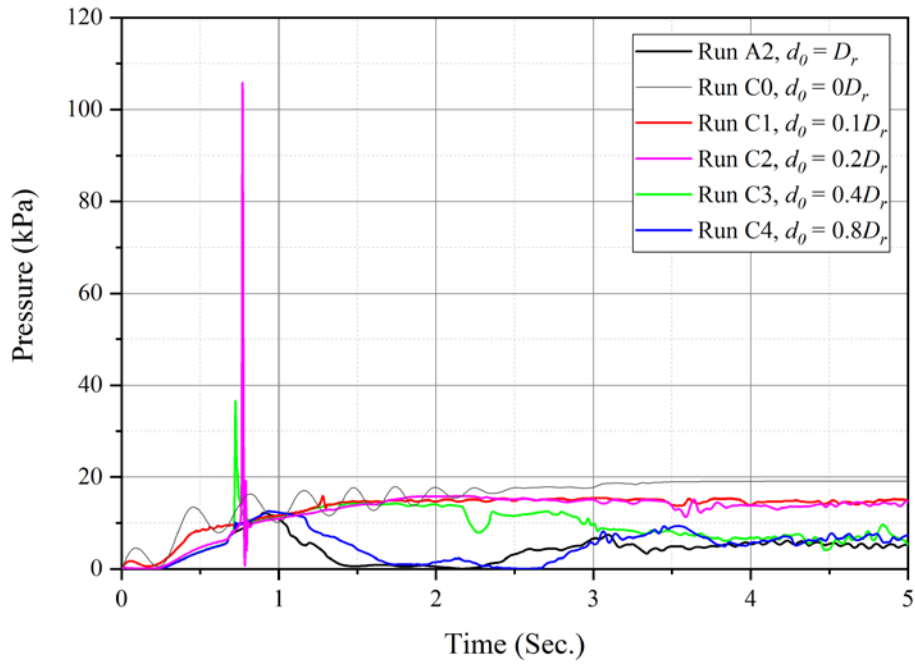


Figure 5-10 Simulated pressure variations for Run C1 to C4. (a) Simulated pressures at PG1; (b) Simulated pressures on the orifice plate installed inside the riser and 0.76 m above the top of the chamber.

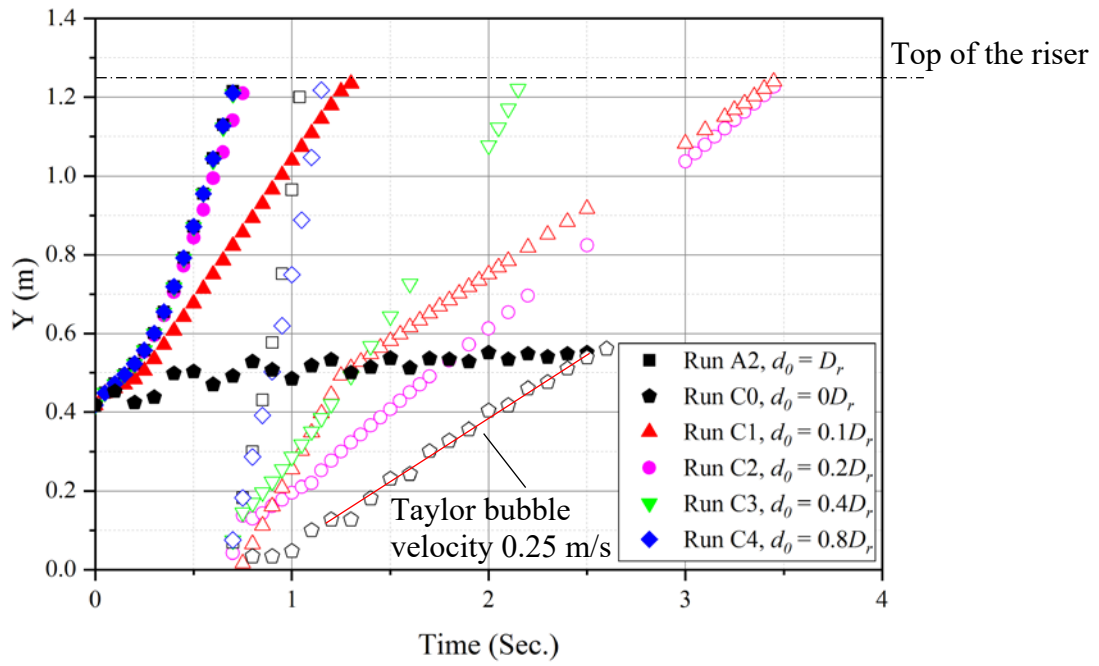


Figure 5-11 Simulated water surfaces (solid symbols) and air/water interfaces (void symbols).

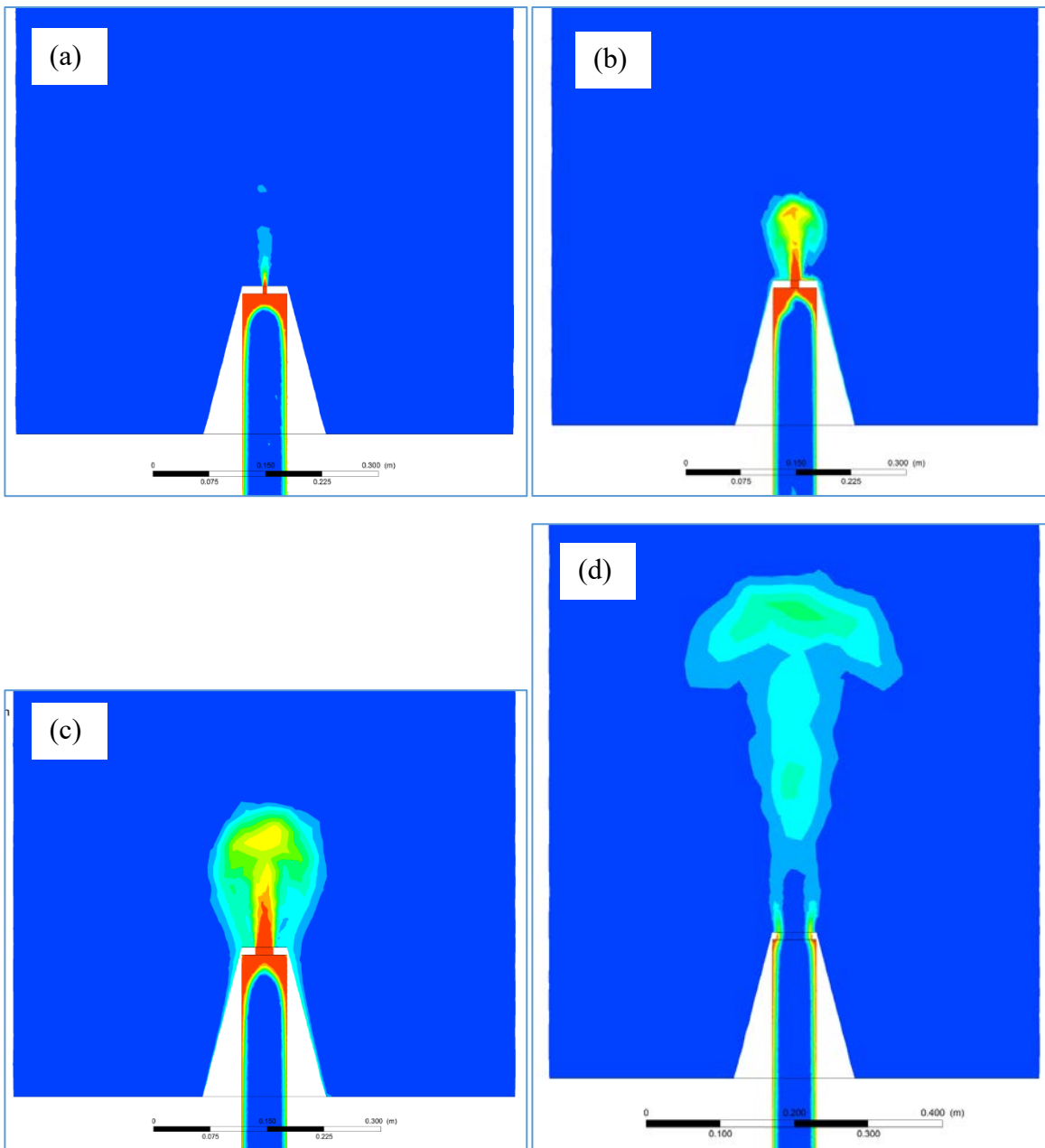


Figure 5-12 Simulated volume fractions of water for geyser heights. (a) Run C1, at $t = 3.4\text{s}$, ruler length = 0.3 m; (b) Run C2, at $t = 3.45\text{s}$, ruler length = 0.3 m; (c) Run C3, at $t = 2.15\text{s}$, ruler length = 0.3 m; (d) Run C4, at $t = 1.15\text{s}$, ruler length = 0.4 m.

6. Analytical Model on Geyser Mitigation Using Orifice Plates on Riser Top*

6.1. Introduction

Geyser events in storm sewer systems are explosive air/water mixture shooting out of manhole when the storm sewer system is subject to heavy storm events. The occurrence of geyser events in storm sewer systems attracts the attention of researchers in recent decades due to public safety issues such as blown off of manhole cover, flooding, damages to sewer structures, etc. (Li and McCorquodale, 1999; Shao, 2013; Huang et al., 2017). It is believed that the release of air pocket in storm tunnels can trigger geyser events (Hamam and McCorquodale, 1982; Zhou et al., 2002). In Edmonton, AB, Canada, one piece of the storm sewer system was upgraded with a new tunnel connecting to the current system. Several geyser events were observed after the retrofitting. In July 2016, a 1:10 year storm was experienced in the retrofitted area and geyser was observed as shown in Figure 6-1. To mitigate the geyser, the use of orifice plates showed potentials on reducing the water flowing out of the manhole during geyser events (Huang, 2017). To address the geyser issue and test the function of the orifice plates, this study was conducted to develop an analytical model to assess the effect of orifice plate on mitigating the geyser event.

Researches have been conducted on the mechanisms of the geysers in sewer systems. The movement of air pocket in a vertical pipe with water was studied by Davies and Taylor (1950). Hamam and McCorquodale (1982) summarized the process of a rapid filling pipe and proposed a rigid water column method to model the mixed flow pressure transients. Li and McCorquodale

* The content of this chapter is being prepared as a journal manuscript for submission

(1999) studied the transient pressure change due to downstream gate sudden closure and pump failure. A series of studies on geysers in sewer systems were done by Vasconcelos and Wright (2009), Wright et al. (2008), Lewis (2011), Vasconcelos and Wright (2011) and Wright et al. (2011a, b). The mechanism of geyser events was proposed as the release of pressurized air pocket via a manhole with water initially remaining in it. Huang (2017) systematically studied the release of air pocket via a riser. It was found that the installation of an orifice plate can reduce the pressure in the tunnel and the amount of water flowing out of the manhole. Cong et al. (2017) studied the releasing of air pocket via a riser from a horizontal tunnel and concluded that the releasing of air pocket can potentially trigger geyser events.

For numerical models on geysers in storm sewer systems, a combined method of Rigid Column Method (RCM) and Method of Characteristic (MOC) for solving the pressure change was proposed by Zhou et al. (2002, 2004). Based on the study of Zhou et al. (2002), Li and Zhu (2018) simulated the pressure change in a horizontal pipe with an end orifice caused by a rapid filling. However, in prototype storm sewer systems, a sandwich pattern of air and water may exist (Huang, 2017) in the riser. The length of the water column decreases due to the film flow along the wall of the riser when the Taylor bubble rises and has been considered in the model of Vasconcelos and Wright (2011). Bouso et al. (2013) summarized the numerical models developed for air/water flow in storm sewer systems. For all above studies, the top of the shaft was fully open. In prototype sewer systems, the manhole openings are usually smaller than the shaft diameter and therefore, simulation with an orifice at top of the shaft is more similar to the prototype.

For computational fluid dynamic (CFD) models, Zhou et al. (2011) developed a 2D CFD model simulating the releasing of an air pocket in a hypothetical pipe. Using a CFD model, Chan et al. (2018) simulated the detailed flow pattern based on the physical model of Cong et al. (2017). Although the CFD model can provide more detailed flow regimes, the computational power required by the CFD model is generally high especially for transient CFD simulations. A typical simulation time for a transient CFD model can take up to weeks (Chan et al., 2018). Therefore, it would be better to develop an analytical model to study the geyser event where the driving pressure is provided by the air pocket and with an orifice plate on the riser top.

To address the issues above, an analytical model solving the process of the geyser and the pressure variation during a geyser event when it is mitigated using an orifice plate is developed. The model can be used to simulate the movement of free surface and the air/water interface at the bottom of the water slug. The model also predicts the pressure variation at the top of the riser induced by the water hammer effect.

6.2. Methodologies

Governing equations

The control volume for this analytical model is shown in Figure 6-2. By tracking the free surface (Y_1) of water slug and the bottom of the water slug (Y_0) in the riser with a height of L , an analytical model can be developed based on momentum equations. This model considers the movement of the water slug as well as the dynamic pressure when the water impinges on the orifice plate. It also simulates the film flow which induces the shortening of the water slug. The following assumptions are made when developing the model:

1: The model is assumed to be a one-dimensional model and all variables are assumed to change only with time. This assumption is reasonable because the ratio of the diameter and the length of the riser is small enough to ignore the asymmetry of the air pocket in the riser for the current cases.

2: The air pocket is moving upward as a Taylor bubble and the length of the water slug in the riser decreases due to the laminar film flow along the wall of the riser. The flow rate of the film flow (Q_f) and the thickness of the film flow (δ) can be written as (Vasconcelos and Wright, 2011):

$$Q_f = A' U_\infty \quad (6-1)$$

$$\frac{\pi}{4} U_\infty (D_r - 2\delta)^2 = \frac{\pi g D_r (\rho_w - \rho_a) \delta^3}{3 \mu_w} \quad (6-2)$$

where: U_∞ is the velocity of the Taylor bubble and it equals to the velocity of the bottom of the water slug at $t = 0$ and $U_\infty = 0.345 \sqrt{g D_r}$, Q_f is the flow rate of the film flow along the wall of the riser, A' is the cross-sectional area of the riser, D_r is the diameter of the riser, μ_w is the dynamic viscosity of water.

3: The air phase undergoes an isentropic expansion/compression process.

4: Both the interface at the bottom of the water slug and the free surface are horizontal, and the water slug remains a single water phase without air entrainment.

Before the free surface reaches the manhole opening, Vasconcelos and Wright (2011) studied the release of air pocket and the movement of free surface and the interface. The governing equations for the water phase and the air phase below the water phase can be written as:

$$\frac{dV_0}{dt} = \frac{g}{Y_1 - Y_0} \left[\frac{Q_f V_0}{gA} + (H_0 - H_1) - (Y_1 - Y_0) - f \frac{(Y_1 - Y_0) |V_0| V_0}{D_r 2g} \right] \quad (6-3)$$

$$\frac{dY_0}{dt} = V_0 \quad (6-4)$$

$$\frac{dV_0}{dt} = \frac{\pi}{4} (D_r - 2\delta)^2 V_0 - Q_f \quad (6-5)$$

$$\frac{dH_0}{dt} = -\frac{1}{\rho_w g} \left[\frac{k C_a}{V_0} \left(\frac{\rho_w g H_0^*}{C_a} \right)^{(k-1)/k} \times \left(\frac{\rho_w g H_0^*}{C_a} \right)^{1/k} \frac{dV_0}{dt} \right] \quad (6-6)$$

$$\frac{dY_1}{dt} = \frac{1}{A} \frac{dV_0}{dt} = V_1 \quad (6-7)$$

$$\frac{dV_1}{dt} = \frac{d\left(\frac{1}{A} \frac{dV_0}{dt}\right)}{dt} = \frac{(D_r - 2\delta)^2}{D_r^2} \frac{dV_0}{dt} \quad (6-8)$$

where: V_0 , V_1 are the velocity of the air/water interface and the free surface respectively, A is the cross-sectional area of the riser, H_0 is the air phase pressure head below the water slug, H_1 is the pressure head of the air phase between the free surface and the orifice plate, k is the polytropic exponent and $k = 1.4$, C_a is a constant equal to the initial absolute air pressure divided by the air density to the power of k , V_0 is the volume of air pocket below the slug of water, f is the head loss coefficient. The asterisk denotes the absolute pressure head. In this sets of equations, Equation 6-3 is the momentum equation considering the movement of the free surface. Equation 6-5 and 6-8 simulates the length of the water slug. Equation 6-6 is the expansion/compression of the air pocket below the water slug.

At this stage, the air phase between the free surface and the orifice plate is controlled by equations (Zhou et al., 2002):

$$\frac{dV_1}{dt} = -AV_1 \quad (6-9)$$

$$\frac{dH_1^*}{dt} = -k \frac{H_1^*}{V_1} \left(\frac{dV_1}{dt} + Q_a \right) \quad (6-10)$$

where: V_{au} is the volume of air between the free surface and the orifice plate, Q_a is the air flow rate through the orifice and can be written as:

$$Q_a = C_d A_o Y \sqrt{2g \frac{\rho_w}{\rho_a} H_1} \quad (6-11)$$

and

$$Y = \left[\frac{k}{k-1} \left(\frac{H_a}{H_1^*} \right)^{2/k} \frac{1 - (H_a/H_1^*)^{(k-1)/k}}{1 - H_a/H_1^*} \right]^{1/2} \quad (6-12)$$

where H_a is atmospheric pressure. Zhou et al. (2002) also suggested that if H_1^*/H_a is larger than 1.89, due to choke flow, the equation 6-12 is to be adjusted to:

$$Y = \sqrt{\frac{1}{2} \left(\frac{H_1^*}{H_1} \right)} \sqrt{k \left(\frac{2}{k+1} \right)^{(k+1)/(k-1)}} \quad (6-13)$$

where C_d is a constant of 0.65 (Zhou et al. 2002), A_0 is the area of the orifice, ρ_w is water density, and ρ_a is air density.

If the calculated $\frac{dV_1}{dt}$ is less than the Q_a , the air between the water slug and the orifice plate is not strongly pressurized. Therefore, the gradient of H_1 can be treated equal to the atmospheric pressure.

Once the free surface reaches the orifice, a water hammer type pressure occurs and the equation used for calculating the water hammer pressure can be written as:

$$\frac{dH_1}{dt} = \frac{1}{\rho_w g} \left(-\rho_m c \frac{dV_1}{dt} \right) \quad (6-14)$$

where c is the pressure wave speed and can be written as $c = \sqrt{\frac{B/\rho_w}{1 + (D_r/e)(B/E)}}$, B is the bulk elastic modulus of water, $B = 2.2$ GPa (Potter et al., 2012), E is the elastic modulus of pipe material, and e is the pipe wall thickness. The peak pressure generated due to the water hammer effect is denoted as H_{PK} . Equation 6-14 considers both the compressibility of water and the elasticity of pipe wall. For a rigid pipe, the pressure wave speed due to water hammer can reach up to 1485 m/s which is the speed of sound in an unbounded water medium. The elasticity of pipe would reduce the pressure wave speed and therefore reduce the pressure rise. In this study, three pipe materials are

tested. For PVC pipe, the elastic modulus is 4.7 GPa, and for steel pipe, the elastic modulus is 200 GPa.

After the free surface reaches the orifice plate, the water flow rate through the orifice can be written

as $A_0 \sqrt{\frac{2gH_1}{1+K}}$, and the velocity of the interface can be written as:

$$V_0 = \frac{A_0 \sqrt{\frac{2gH_1}{1+K} + Q_f}}{A} \quad (6-15)$$

where the K is the minor loss coefficient at the orifice plate. Equation 6-15 shows that the velocity of the bottom of the water slug is a function of the water flowing out of the orifice plate and the film flow along the wall of the riser.

The governing equations listed above can be solved numerically using a fourth-order Runge-Kutta algorithm using Matlab 9.0 (Mathwork, 2017). The time step used in the calculation is in order of 1.0×10^{-5} s to ensure the numerical stability. The calculation stops when one of the following condition is reached: the length of the water slug is zero, or the air/water interface at bottom of the water slug reaches the orifice. Table 6-1 is a summary of all numerical simulation conditions. A total number of 201 runs were conducted. Each run contains 96 calculations where the orifice size ranging from 0.05 to 0.99 D_r . Each run takes less than 1 minutes to complete on a Dell workstation with an Intel i7 3.60GHz CPU. Run A and B are model calibration and validation with experimental data and with Vasconcelos and Wright (2011). Run C is for testing the effect of the diameter of the riser on the geyser events and Run D is for testing the height of the riser L . Run E is for testing the geyser event with different pipe materials.

Model calibration and validation

Run A is a case containing the calibration and validation of the analytical model. The model was validated by the physical model with an orifice plate inserted in the riser just above the pressure transducer at a height of 0.78 m and with an orifice of $0.5D_r$ and $0.1D_r$, and the initial water level in the riser is 0.30 m. The measured air pocket size is 0.08 m^3 , and the water flow rate increases from 20 to 40 L/s. The initial condition of the calculation was from the physical measurement (Liu, 2018). When conducting the calculation, it was found that the right hand of equation 6-4 is to be multiplied by a factor of 1.15 to match the calculated and the measured air/water interface. The loss coefficient f follows the equation proposed by Arai and Yamamoto (2003):

$$f = \left[1.14 - 2 \log_{10} \left(\frac{\varepsilon}{D} + \frac{21.25}{Re^{0.9}} \right) \right]^{-2} \quad (6-16)$$

where $\frac{\varepsilon}{D}$ is the relative roughness of pipe materials, Re is the Reynold's number of the water flow.

The comparison of calculated and measured free surface and the bottom of the water slug as well as the pressure under the orifice plate is plotted in Figure 6-3. From the figure it can be seen that the theoretical calculation reflects well on the pressure peak and the movement of free surface. However, for the air/water interface modelling, the calculation showed discrepancy after the free surface reaching the orifice, especially for the $d = 0.1D_r$ case.

Run B is a simulation based on Vasconcelos and Wright (2011). The diameter of the riser is 0.016 m and the height of the riser is 0.61 m. The initial water level in the riser is 0.35 m and the head in the air pocket is 0.305 and 0.610 m. The calculated free surface and the bottom of the water slug is shown in Figure 6-3e with the measured data of Vasconcelos and Wright (2011). It can be seen that the predicted free surface and air/water interface compares generally well with the

measurement. For each flow condition, the peak pressure occurred due to the impingement of the water slug on the orifice plate is denoted as H_{PK} for further analysis.

6.3. Results and discussions

Effect of driving pressure and initial water slug length

Figure 6-4a shows the relationship between the peak pressure (H_{PK}) due to water hammer effect and the orifice size. The pressure firstly increases with the opening size and then decrease. This trend is in agreement with Zhou et al. (2002) and Li and Zhu (2018). It also shows that when the driving pressure increases, the calculated H_{PK} increases. For driving pressure of 10 m, the maximum peak pressure can reach up to 53 m. For driving pressure of 5 m, the maximum peak pressure is 36 m. Doubling the driving pressure from 5 to 10 m would generate an increase on the maximum peak pressure from 36 to 53 m which is an increase of 47%. The reason why this relationship was observed is that the movement of the water slug is a combined effect of the driving pressure and the orifice plate. The existence of the orifice plate impedes the upward motion of the water slug and therefore doubling the driving pressure cannot generate a doubled peak pressure.

Figure 6-4b shows the trend of the peak pressures induced by the water hammer effect with different initial water slug lengths. The figure suggests that with longer water slug length, a smaller peak pressure is generated. This is mainly because that for a longer water slug, the $(Y_1 - Y_0)$ term in equations 6-6 and 6-11 increases, and induces a lower V_1 and V_0 . A smaller water hammer pressure is therefore generated. This trend is in agreement with Zhou et al. (2002). The difference between Zhou et al. (2002) and the current model is that the driving pressure of Zhou et al. (2002) is fixed and the free surface is driving by the water column. In the current model, the free surface

is driving by the air pocket below the air/water interface. Comparing the results of $(Y_1 - Y_0) = 0.3$ and 0.77 m, an approximately 2 times of the increasing on initial water slug length would generate a decrease on the peak pressure from 15 to 10 m, which is a 30% reduction.

Effect of riser diameter and riser height

Run C and D are cases to test the effect of different diameters and the heights of the riser on the peak pressure. A variety of different initial conditions is simulated as listed in Table 6-1. A set of representative results for Run C and D are plotted in Figure 6-5 and the initial condition for the plot is $(Y_1 - Y_0)/L = 0.3$, and $H_0 = 1$ m. Figure 6-5a shows the pressure variations for different riser diameters of 0.055, 0.1, 0.2, and 0.3 m respectively. It indicates that for the same initial conditions, a larger riser diameter will induce a lower manhole pressure. This is mainly because that for a larger D_r , the increased riser area results in a decrease in the momentum term in equation 6-8. Although the head loss term in equation 6-8 increases, the change of the area is in a higher order, and the peak pressure induced by the water hammer effect mainly depends on the free surface velocity. Therefore, a riser with larger diameter would results in a lower peak pressure for a given orifice size.

From Figure 6-5a it can also be seen that the peak pressure is sensitive to the riser diameter before the peak pressure reaches the maximum. After around $d/D_r = 0.2$, the difference between pressures is smaller compared to the pressure when d/D_r is less than 0.2. The highest peak pressure varies from 15 to 17 m (13% increasing) for riser diameter decreasing from 0.3 to 0.055 m. However, the peak pressure is not always higher for smaller diameter. For the cases with $H_0 = 20$ m, $(Y_1 - Y_0)/L = 0.5, 0.6, 0.8$, the maximum peak pressure increases when the riser diameter increases. The

highest standard deviation of the maximum peak pressure is 15% of the mean for $H_0 = 5$ m, $(Y_1 - Y_0)/L = 0.8$. Considering the riser diameter changing 5.43 times from 0.055 to 0.3 m, the 15% of variation of maximum peak pressure can be considered as not sensitive to the change of riser diameter.

Figure 6-5b shows the simulated peak pressures for different riser heights of 0.78, 1, 1.22, 1.5, 1.7, and 2.0 m respectively. For the same initial conditions, a larger riser length L responses a lower peak pressure. This is mainly because that for a higher riser, the initial filling ratio of 0.3 results a longer slug of water. For a given driving pressure, the longer slug of water accelerates slower and therefore results in a lower free surface velocity when the slug of water reaches the orifice plate. A lower free surface velocity induces a lower water hammer pressure. It also can be seen that when the orifice size is larger than the one where the highest peak pressure occurs, the peak pressure is sensitive to the riser height. The change of the maximum peak pressure decreases from 19 to 15m (21% decreasing) for riser height increasing from 0.78 to 2 m.

Considering the peak pressure variation of 47% and 30% for doubling driving pressure and initial water slug length, the maximum peak pressure is in general less sensitive to the riser height and riser diameter. Figure 6-6 is a plot of all maximum peak pressures generated from Run A, C and D. The fitting equation can be written as:

$$H_{max} = 6.10[(Y_1 - Y_0)/H_0]^{-0.7} \quad (6-17)$$

with $R^2 = 0.94$, the coefficients of 6.10 and -0.7 mainly depend on the pipe material. The figure suggests that a lower $(Y_1 - Y_0)/H_0$ corresponds a higher H_{max} . It is either due to a lower initial water slug length or a higher driving pressure.

Effect of pipe materials

Run E is for testing the maximum peak pressure induced by the water hammer effect in steel pipes. Because the elastic modulus of steel pipe is higher than the PVC pipe, the predicted maximum peak pressure is expected to be higher than the previous runs. Figure 6-7 shows the calculated maximum peak pressure for steel pipes. The maximum pressure can be fitted into:

$$H_{max} = 16.61[(Y_1 - Y_0)/H_0]^{-0.6} \quad (6-18)$$

with $R^2 = 0.88$. A higher coefficient at the right hand side suggests a higher H_{max} value for a given initial conditions comparing with the one of PVC pipe. For the same initial condition, the maximum peak pressure is high for a larger riser diameter, and the pressure increases for a higher riser. The trend is in agreement with the one of PVC pipe.

The acoustic wave speed of water in PVC pipe is calculated as 562 m/s and the one for steel pipe is 1333 m/s. Equation 6-14 suggests that for the same boundary conditions, the flow in steel pipe would generate a water hammer pressure 2.37 times of the one in PVC pipe.

Orifice size when maximum peak pressure occurs

Figure 6-8 shows the orifice size when maximum peak pressure occurs. The figure suggests that the peak pressure reaches its maximum when the orifice opening size ranges from 0.13 to 0.3 times of the riser diameter. Among the simulated 193 cases, no obvious trend was observed. The averaged orifice size d/D_r for the highest peak pressure is 0.201 with standard deviation of 0.038. The standard deviation is 19% of the average value. Considering the variation of pipe material, riser height, and riser diameter is 42, 2.5, 5.45 times. The change of orifice size for each condition

is small. Therefore, when designing orifice plates to mitigate geyser event, the orifice plate size between 0.13 to 0.3 times of the riser diameter should be avoided.

6.4. Conclusion

An analytical model simulating the dynamics of the geyser event is developed when the orifice plates are installed on the top of the riser for geyser mitigation. The model is able to estimate the pressures in the manhole induced by the impingement of the water slug which is driven by the pressure in the chamber. The water hammer effect and the decreasing of the water slug length due to the film flow are considered. The following conclusions can be drawn based on the analysis:

1. The sensitive analysis suggests that the diameter and the height of the riser have minor effect on the peak pressure. The initial water slug length and the driving pressure determine the peak pressure.
2. Pipe with higher elastic modulus corresponds a higher peak pressure given the same initial conditions. The higher peak pressure is mainly induced by the increased acoustic speed of water in pipes with different materials.
3. The orifice opening size when the peak pressure reaches maximum is between 0.13 to 0.3 times of the riser diameter. When designing the orifice plate, this size should be avoided to prevent the structure from damage due to the water hammer effect.

In prototype storm sewer system, the actual size and hydrograph may change and the scale effect of air/water mixture flow is still unclear. In actual storm sewer systems, the large scale air/water flow may entrain air into the water slug and may differ in the results. Therefore, measurement on the geyser event in a prototype storm sewer system is needed to understand the geyser events and the effectiveness of different mitigation methods.

Acknowledgement

The writers gratefully acknowledge the financial support from the Natural Sciences and Engineering Research Council (NSERC) of Canada, and the Epcor.

List of symbols

A : cross-sectional area of the riser;

A_0 : area of the orifice;

B : bulk elastic modulus of water;

c : pressure pulse wave speed;

C_a : constant and $Ca = P_{a0}/\rho_a^k$;

C_d : constant and $Cd = 0.65$;

D_r : diameter of the riser;

E : elastic modulus of pipe material;

e : pipe wall thickness;

f : head loss coefficient;

H_a : atmospheric pressure;

H_0 : air phase pressure below the water slug;

H_{max} : maximum peak pressure;

H_l : air phase pressure head between the water slug and the orifice plate;

H_{PK} : peak pressure generated due to the water hammer effect;

k : the polotropic exponent and $k = 1.4$;

L : height of the riser;

Q_a : air flow rate via orifice plate;

Q_f : flow rate of the film flow along the wall of the riser;

U_∞ : velocity of Taylor bubble;

V_l : velocity of the free surface;

V_0 : velocity of the air/water interface;

\forall_0 : volume of air pocket below the slug of water;

\forall_1 : volume of air between the free surface and the orifice plate;

Y_l : location of the free surface;

Y_0 : location of the air/water interface;

μ_w : dynamic viscosity of water;

ρ_w : water density;

ρ_a : air density.

References

- Arai, K., and Yamamoto, K. (2003). "Transient analysis of mixed free-surface pressurized flows with modified slow model. Part1: Computational model and experiment." *4th ASME_JSME Joint Fluids Engineering Conference*, Hololulu, Hawaii, USA, July 6-10, 2003
- Bouso, S., Daynou, M., and Fuamba, M. (2013). "Numerical modeling of mixed flow in stormwater systems: critical review of literature." *Journal of Hydraulic Engineering*, 139(4): 385-396.
- Chan, S. N., Cong, J., and Lee, J. H. W. (2018). "3D numerical modeling of geyser formation by release of entrapped air from horizontal pipe into vertical shaft." *Journal of Hydraulic Engineering, ASCE*: 10.1061/(ASCE)HY.1943-7900.0001416.
- Cong, J., Chan, S. N., and Lee, J. H. W. (2017). "Geyser formation by release of entrapped air from horizontal pipe into vertical shaft." *Journal of Hydraulic Engineering, ASCE*: 10.1061/(ASCE)HY.1943-7900.0001332.
- Davies, R. M., and Taylor, F. R. S. (1950). "The mechanics of large bubbles rising through extended liquids and through liquids in tubes." *Proceedings of the Royal Society A*, 200(1062): 375- 390.
- Hamam, M. A., and McCorquodale, J. A. (1982). "Transient conditions in the transition from gravity to surcharged sewer flow." *Canadian Journal of Civil Engineering*, 9: 189-196.
- Huang, B. (2017) "Study on Geysers in Urban Drainage Systems". *PhD Thesis*, Nanjing Hydraulic Research Institute, Nanjing, China.
- Lewis, J. M. (2011). "A physical investigation of air/water interactions leading to geyser events in rapid filling pipelines." *PhD thesis*, University of Michigan, Ann Arbor, Michigan.

Li, J., and McCorquodale, J. A. (1999). "Modelling mixed flow in storm sewers." *Journal of Hydraulic Engineering*, 125(11): 1170-1180.

Li, L., and Zhu, D. (2018). "Modulation of the Transient Pressure by Air Pocket in a Horizontal Pipe with an End Orifice." *Water Science and Technology*, accepted.

Liu, L. (2018). "Experimental Study on Edmonton's Storm Geyser Formation Mechanism and Mitigation Measures." MSc thesis, University of Alberta, Edmonton, Alberta.

Potter, M. C., Wiggert, D. C., and Ramadan, B. H. (2012). "*Mechanics of Fluids.*" 4th Edition, Cengage Learning: Stamford.

Shao, Z. S. (2013). "Two-dimensional hydrodynamic modelling of two-phase flow for understanding geyser phenomena in urban storm water system." *PhD thesis*, University of Kentucky, Lexington, Kentucky.

Vasconcelos, J. G., and Wright, S. J. (2009). "Investigation of rapid filling of poorly ventilated stormwater storage tunnels." *Journal of Hydraulic Research*, 47(5): 547-558.

Vasconcelos, J. G., and Wright, S. J. (2011). "Geysering generated by large air pockets released through water-filled ventilation shafts." *Journal of Hydraulic Engineering*, 137(5): 543-555.

Wright, S. J., Lewis, J. W., and Vasconcelos, J. G. (2011a). "Geysering in rapidly filling storm-water tunnels." *Journal of Hydraulic Engineering*, 137(1): 112-115.

Wright, S. J., Lewis, J. W., and Vasconcelos, J. G. (2011b). "Physical processes resulting in geysers in rapidly filling storm-water tunnels." *Journal of Irrigation and Drainage Engineering*, 137(3): 192-202.

Wright, S. J., Vasconcelos, J. G., Creech, C. T., and Lewis, J. W. (2008). "Flow regime transition mechanisms in rapidly filling stormwater storage tunnels." *Environmental Fluid Mechanics*, 8(5): 605-616.

Youtube (2018). "Edmonton's Old Faithful." online: <https://www.youtube.com/watch?v=pvGfmwYvXtg> accessed 25 Feb. 2018

Zhou, F., Hicks, F. E., and Steffler, P. M. (2002). "Transient flow in a rapidly filling horizontal pipe containing trapped air". *Journal of Hydraulic Engineering*, 128(6): 625-634.

Zhou, F., Hicks, F. E., and Steffler, P. (2004). "Analysis of effects of air pocket on hydraulic failure of urban drainage infrastructure." *Canadian Journal of Civil Engineering*, 31: 86-94.

Zhou, L., Liu, D., and Ou, C. (2011). "Simulation of flow transients in a water filling pipe containing entrapped air pocket with VOF model." *Engineering Applications of Computational Fluid Mechanics*, 5(1): 127-140.

Table 6-1 List of numerical simulation arrangement.

Run	D_r (m)	L (m)	$(Y_l - Y_0)/L$	d/D_r	H_0 (m)	Pipe material
A ¹	0.055	0.78	0.3, 0.39 ¹ , 0.6, 0.8	0.05 to 0.99	1 ¹ , 5, 10	PVC
B ^{1,2}	0.013	0.61	0.583	0.99	0.305, 0.610	
C1	0.055	1.22	0.3, 0.5, 0.6, 0.8	0.05 to 0.99	1, 5, 10, 20	
C2	0.1					
C3	0.2					
C4	0.3					
D1	0.055	0.78				
D2		1.0				
D3		1.5				
D4		1.7				
D5		2.0				
E1	0.055	0.78				Steel
E2		1.5				
E3	0.1	1.5				
E4	0.3					

1: Model calibration and validation at $d/D_r = 0.1$ and 0.5 ; 2: Model based on Vasconcelos and Wright (2011).



Figure 6-1 Geysers events in Edmonton at different locations. Youtube (2018).

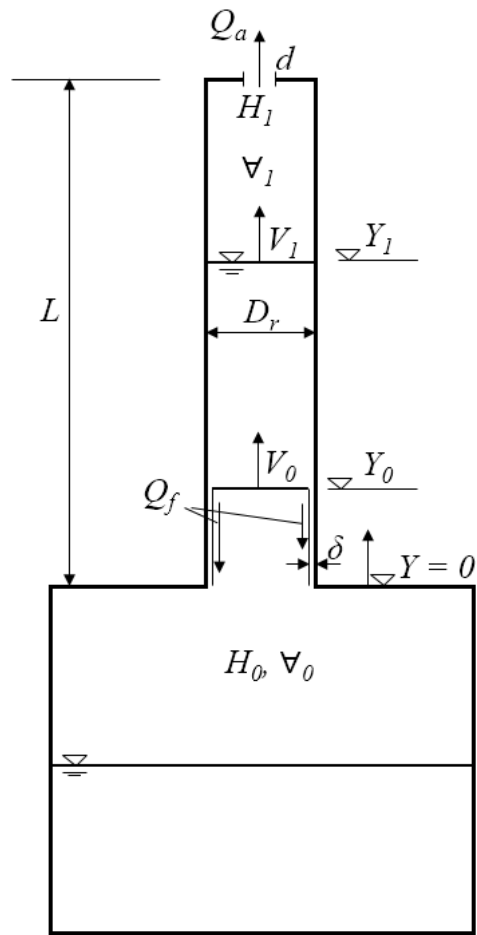
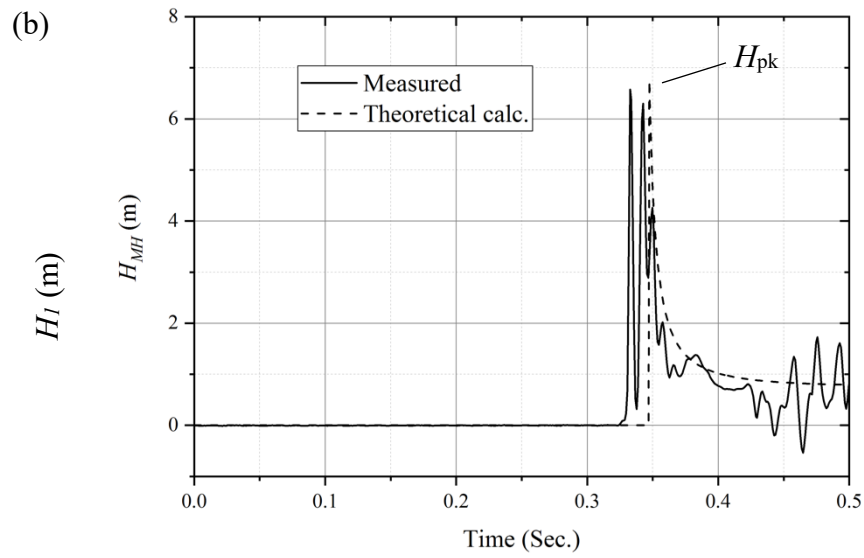
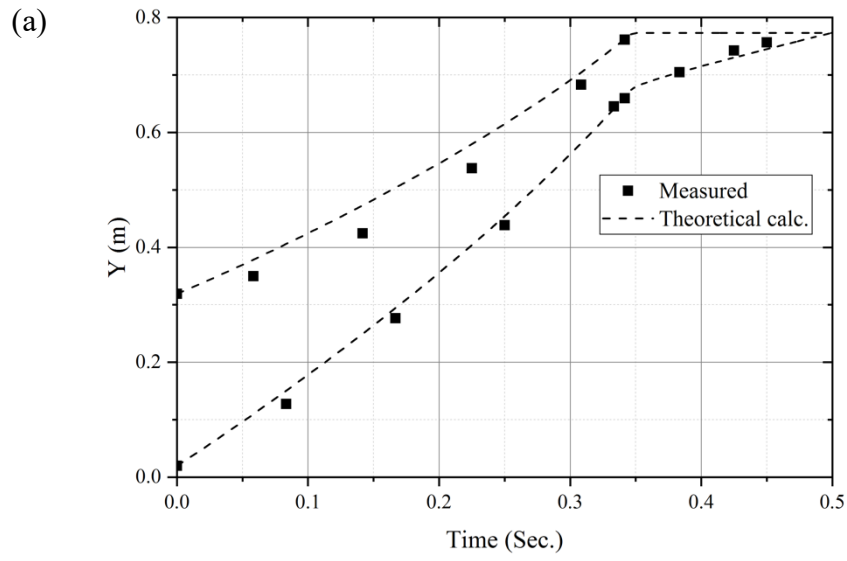
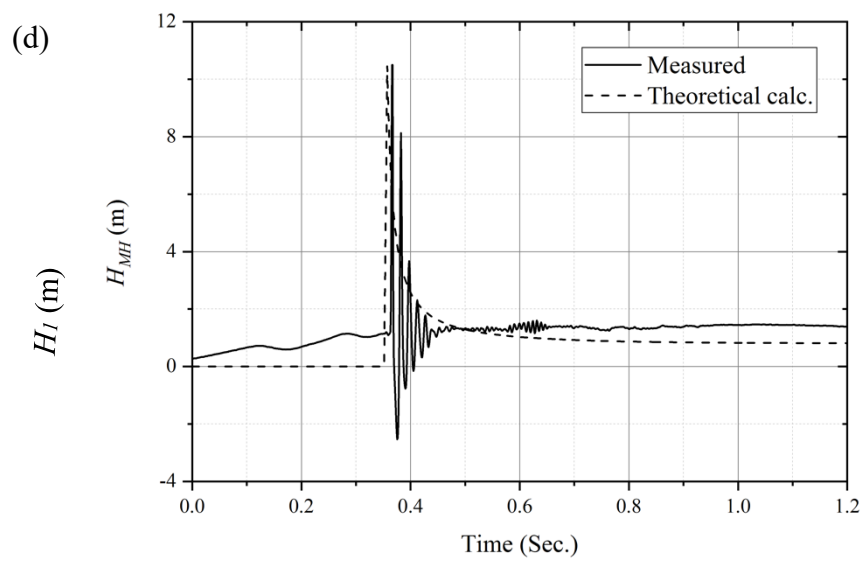
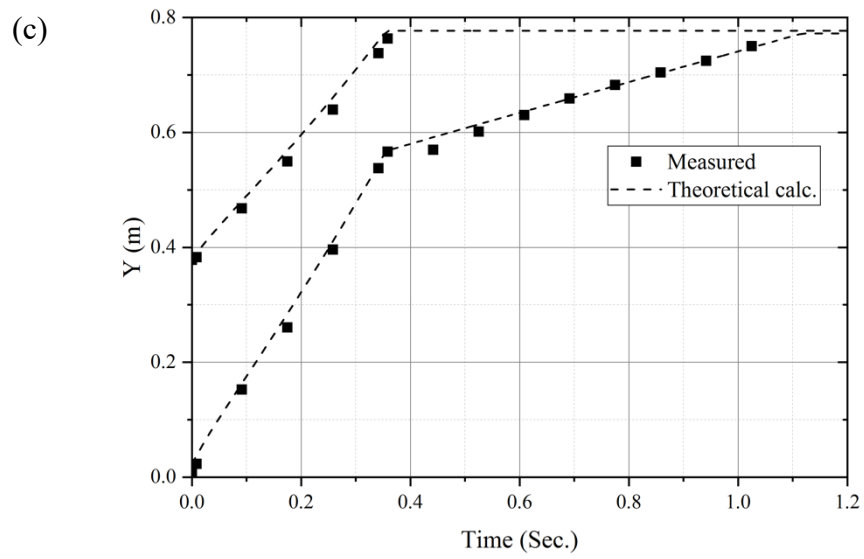


Figure 6-2 Schematic of the control volumes for theoretical calculation.





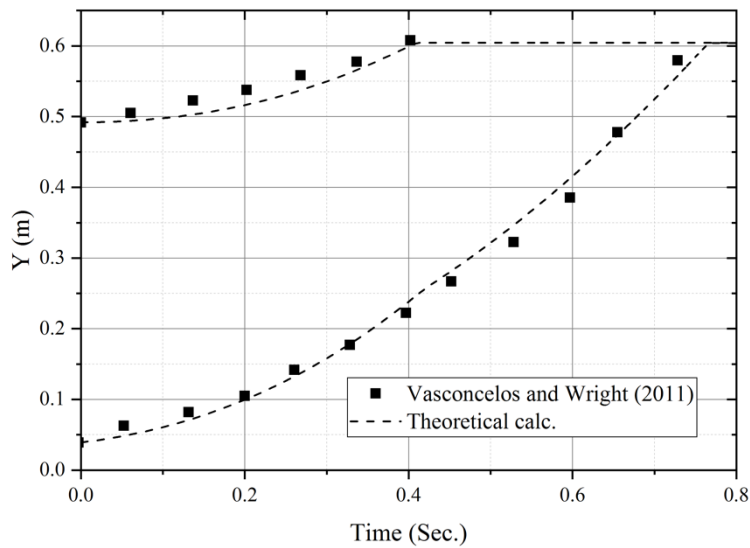
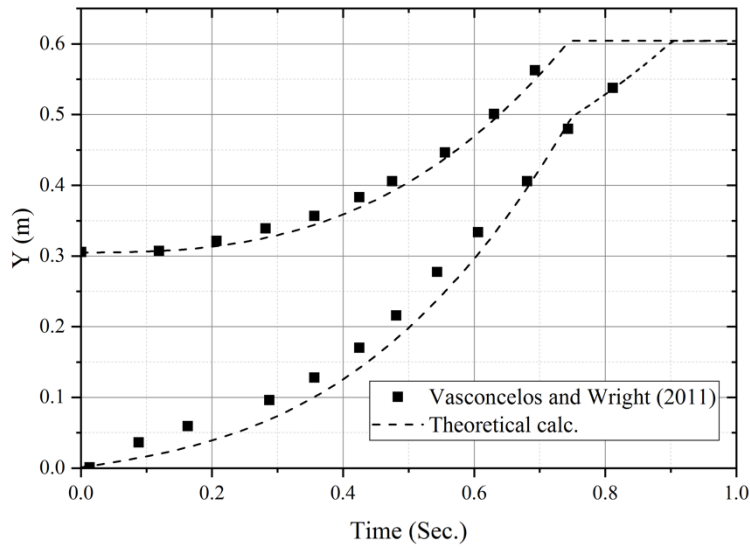


Figure 6-3 Comparison between theoretical calculated and physical measurement. (a) Measured and calculated free surface and interface for Run A, OP: $d = 0.5D_r$; (b) Measured and calculated pressure for Run A, OP: $d = 0.1D_r$; (c) Measured and calculated free surface and interface for Run A, OP: $d = 0.1D_r$; (d) Measured and calculated pressure for Run A, OP: $d = 0.1D_r$; (e) Model validation with Vasconcelos and Wright (2011) for Run B, $H_0 = 0.305$ m; (f) Model validation with Vasconcelos and Wright (2011) for Run B, $H_0 = 0.610$ m.

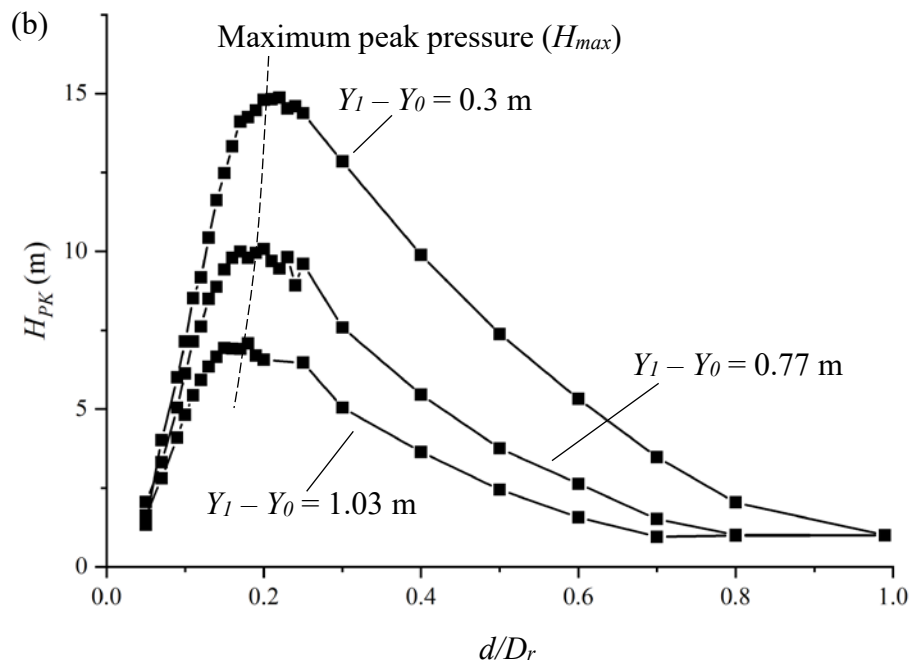
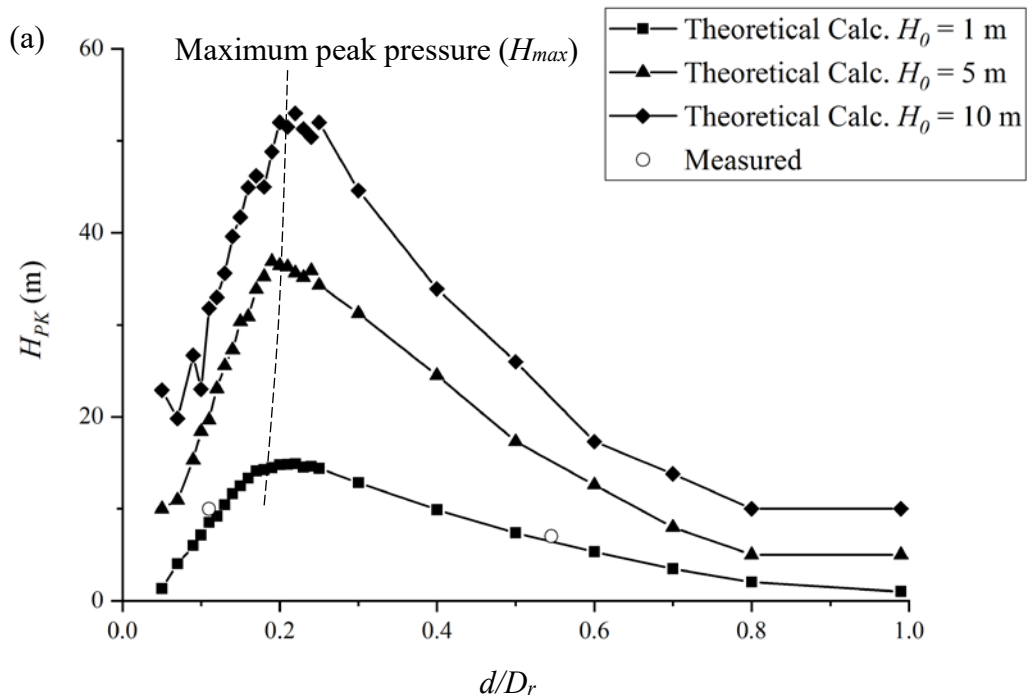


Figure 6-4 Theoretical calculated peak pressure and the orifice size for PVC pipes Run A, (a) With different driving pressure at $(Y_1 - Y_0)/L = 0.39$. (b) With different initial water slug length at $H_0 = 1$ m.

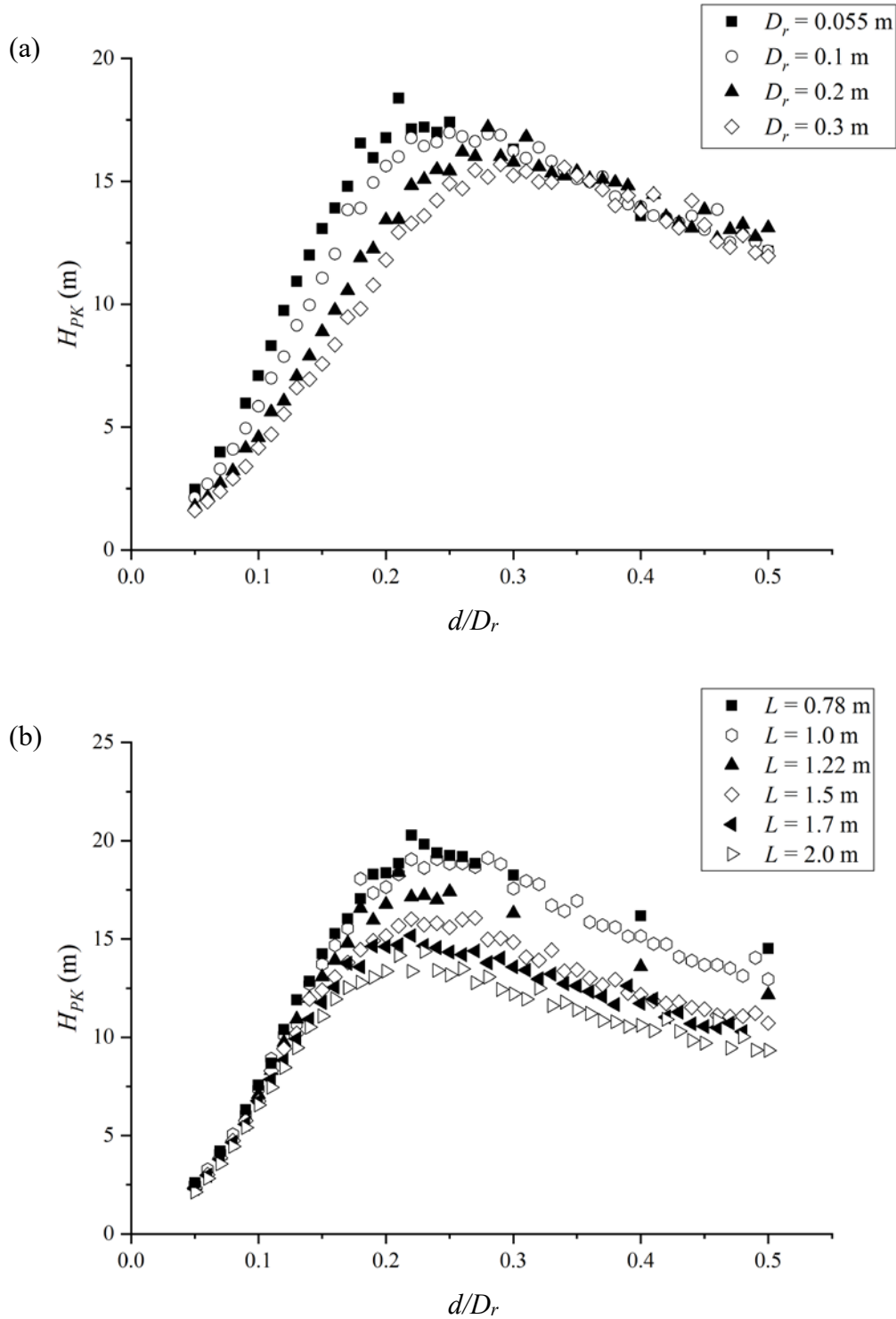


Figure 6-5 Theoretical calculated peak pressure and the orifice size for PVC pipes Run C and D, $H_0 = 1$ m, $(Y_1 - Y_0)/L = 0.3$. (a) With different riser diameter, $L = 1.22$ m; (b) With different riser height, $D_r = 0.055$ m.

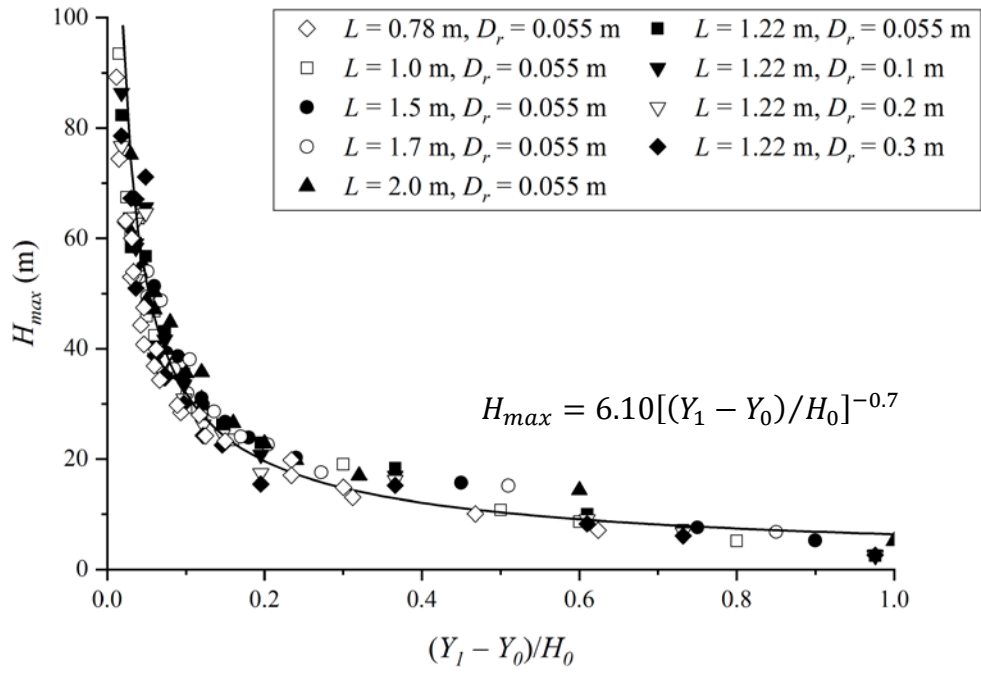


Figure 6-6 Theoretical calculated maximum peak pressure for Run A, C, and D.

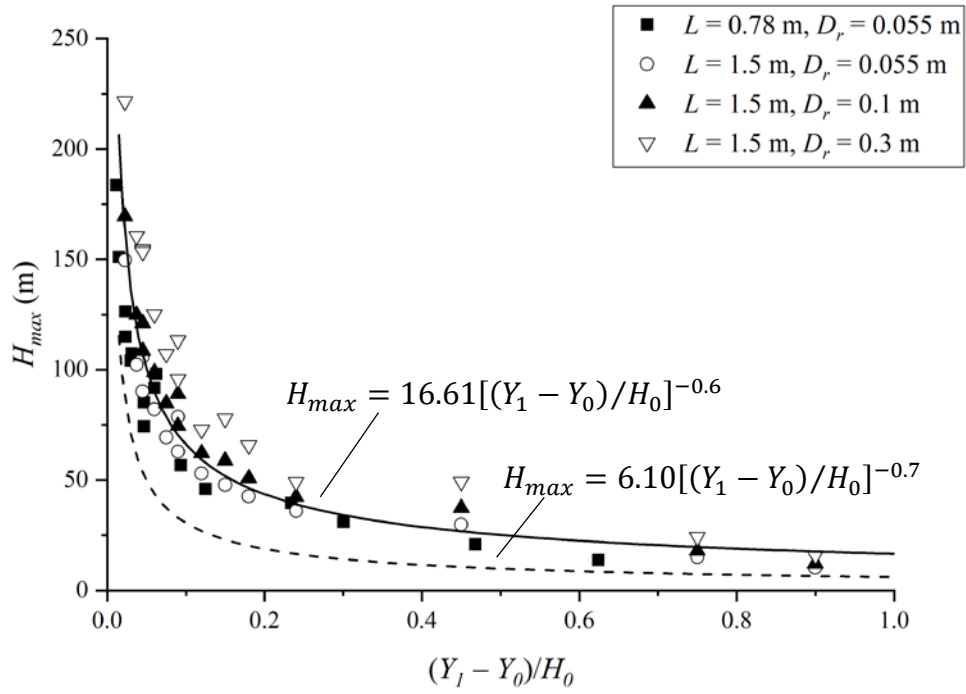


Figure 6-7 Theoretical calculated maximum peak pressure for Run E.

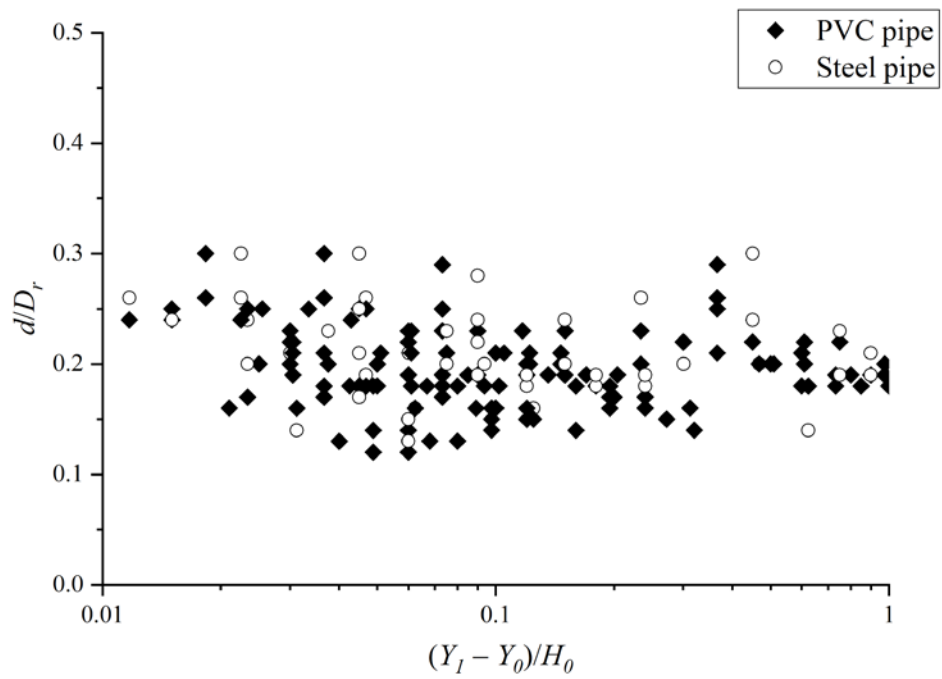


Figure 6-8 Theoretical calculated orifice size when the maximum peak pressure occurs.

7. General Conclusions and Recommendations

The air movement in sewer systems is studied in this thesis on two major aspects: (1) the transportation of air in a single sewer pipe and sanitary sewer networks and (2) the mechanism and the mitigation methods of geyser events in storm sewer systems. Following is the general conclusions for the study:

1. In the chapter 3, the air movement in a single sewer pipe could be successfully modelled using the CFD model. A drag coefficient between the free surface and the air was proposed to predict the air flow induced by the combined effect of the wastewater drag and the pressure gradient. The air transported via a hydraulic jump when headspace exists downstream of the jump was substantially higher than the air transported in form of bubble. The hydraulic jump could provide a source of momentum for air flow in the headspace due to its rough surface on the roller.
2. In the chapter 4, the air transportation in a sewer network could be successfully modeled by incorporating the previous studies on the air movement in a single pipe and the proposed air leakage model. The air leakage via the manhole pickholes along the lateral connections decreased with the increasing pipe number. It was defined as the zone of influence where the pipe number reached a certain value and the additional pipes did not significantly affect the air flow. The zone of influence depended on the property of the lateral pipes such as diameter, friction coefficient, length, etc.
3. In the chapter 5, the geyser events were triggered when the trapped air pocket was released via the riser. Two different types of geyser events were observed. One was the geyser induced by a fast propagating wave front while the downstream was almost full. Another one was the geyser induced by the releasing of the entrapped air pocket with water existing

in the riser. The water recirculation chamber, benching, and orifice plate were able to reduce the water flowing out of the riser during the geyser events. However, the installation of orifice plate would generate a water-hammer like pressure in the riser due to the impingement of the water slug on the orifice plate.

4. In the chapter 6, the water-hammer like pressure observed in the previous study was studied. It was found that the pressure peak was sensitive to driving pressure and the initial water slug length, and not sensitive to the riser diameter and riser height. The pipe material with a higher elastic modulus would generate a higher peak pressure. The pressure reached the maximum when the opening size of the orifice plate is around 0.2 times of the diameter of the riser.

This thesis will extend the knowledge in three aspects: (1) the air movement in a single sewer pipe with high water velocity, and with the existence of a hydraulic jump; (2) the air movement in sewer networks with dropshafts and a pump station; (3) the mechanism, and ways of mitigating geyser event in a storm sewer system. This thesis provides detailed field, numerical and laboratory data for the development and calibration of the models on the air movement in sewer systems. In particular, this thesis is useful in guiding municipalities with activities such as sewer odor mitigation, reducing pressure in sewer systems, flood prevention, geyser mitigation, etc.

In general, this research covers the air movement in sewer systems. However, there are still aspects left for further studies. The following is a list of recommendations on further studies:

1. Further study on the air movement in the prototype dropshafts because the assumptions made in this study was developed based on the laboratory studies. The drop height, shaft

diameter, and water flow rate are the important factors to the air movement because the scale effect of air flow is still unclear.

2. Further study on the reasonable simplification of the prototype system for more complex pipe connections, because in the current study, the pipe connection is relatively simple with one single trunk. For more complex trunk connections such as loops, crossings, more consideration should be paid on the simplification methods.
3. Experimental studies on the geyser events in storm sewer systems to understand better on the mechanism of the geyser event, especially on the interaction of air flow in manhole shaft and the water film flow along the wall of the manhole shaft.
4. Prototype measurement on the pressure change during a geyser event in the real storm sewer systems because the scale effect of air flow between laboratory models and prototype structures is still unclear.

Bibliography

Anderson, A. G., and Dahlin, W. (1975). “Model Studies of Dropshafts for the Tunnel and Reservoir Plan.” *Report*. St. Anthony Falls Hydraulic Laboratory, University of Minnesota.

Ansys (2011). “ANSYS CFX Guide.” Release 14.0.

Arai, K., and Yamamoto, K. (2003). “Transient analysis of mixed free-surface pressurized flows with modified slow model. Part1: Computational model and experiment.” *4th ASME_JSME Joint Fluids Engineering Conference*, Hololulu, Hawaii, USA, July 6-10, 2003

Associate Engineering (AE) (2008). “Odor control program report.” for the City of Edmonton, Alberta, Canada.

Bouso, S., and Fuamba, M. (2014). “Numerical and experimental analysis of the pressurized wave front in a circular pipe.” *Journal of Hydraulic Engineering*, 140(3): 300-312.

Bouso, S., Daynou, M., and Fuamba, M. (2013). “Numerical modeling of mixed flow in stormwater systems: critical review of literature.” *Journal of Hydraulic Engineering*, 139(4): 385-396.

Bouso, S., Daynou, M., and Fuamba, M. (2014). “Mixed flows with depressurizing wavefront in circular pipe.” *Journal of Irrigation and Drainage Engineering*, 140(1): 1-10.

Camino, G. A., Zhu, D. Z., and Rajaratnam, N. (2014). “Flow observations in tall plunging flow dropshafts.” *Journal of Hydraulic Engineering, ASCE*, 141(1): 06014020.

CBC NEWS (2018). “Pedestrian falls into manhole after downtown Edmonton explosion.” Online. [<http://www.cbc.ca/news/canada/edmonton/downtown-explosion-manhole-cover-1.4480694>, Accessed 30-Apr.-2018]

CBS NEWS (2016). “Boston driver killed by flying manhole cover identified.” Online. [<https://www.cbsnews.com/news/flying-manhole-cover-kills-driver-in-boston/>, Accessed 20-Apr.-2018]

Chan, S, N., Cong, J., and Lee, J. H. W. (2018). “3D numerical modeling of geyser formation by release of entrapped air from horizontal pipe into vertical shaft.” *Journal of Hydraulic Engineering, ASCE*: 10.1061/(ASCE)HY.1943-7900.0001416.

Chanson, H. (2006). “Air bubble entrainment in hydraulic jumps, similitude and scale effects.” *Research Report No. CE57/05*, Department of Civil Engineering, The University of Queensland.

Chanson, H. (2007). “Air entrainment processes in a full-scale rectangular dropshaft at large flows.” *Journal of Hydraulic Research*, 45(1): 43-53.

Chanson, H. (2009). “Turbulent air-water flows in hydraulic structures: dynamic similarity and scale effects.” *Environmental Fluid Mechanics*, 9(2): 125-142.

Chanson, H. and Brattberg, T. (2000). “Experimental study of the air-water shear flow in a hydraulic jump.” *International Journal of Multiphase Flow*, 26(4), 583-607.

Chanson, H. and Gualtieri, C. (2008). “Similitude and scale effects of air entrainment in hydraulic jumps.” *Journal of Hydraulic Research*, 46(1), 35-44.

Chanson, H. and Qiao, G. L. (1994). “Air bubble entrainment and gas transfer at hydraulic jumps.” *Research Report No. CE149*, Department of Civil Engineering, The University of Queensland.

Choi, Y. J., Leon, A. S., and Apte, S. V. (2014). “Three-dimensional numerical modeling of air-water geyser flows.” *World Environmental and Water Resources Congress*, June 1-5, Portland, Oregon.

Choi, Y. J., Leon, A. S., and Apte, S. V. (2016). “A one-dimensional numerical model to predict pressure and velocity oscillations of a compressed air pocket in a vertical shaft filled with water.” *World Environmental and Water Resources Congress*, May 22-26, West Palm Beach, Florida.

City of Edmonton (2018). “Sewer Facts and Statistics.” Online. [https://www.edmonton.ca/city_government/utilities/sewer-facts-and-statistics.aspx, Accessed 27-Mar.-2018].

Cong, J., Chan, S. N., and Lee, J. H. W. (2017). “Geyser formation by release of entrapped air from horizontal pipe into vertical shaft.” *Journal of Hydraulic Engineering*, 143(9): 04017039.

Cunge, J. A., and Wegner, M. (1964). “Numerical integration of Bane de Saint Venant’s flow equations by means of an implicit scheme of finite differences. Applications in the case of alternately free and pressurized flow in a tunnel.” *La Houille Blanche*, 1: 33-39.

Davies, R. M., and Taylor, F. R. S. (1950). “The mechanics of large bubbles rising through extended liquids and through liquids in tubes.” *Proceedings of the Royal Society A*, 200(1062): 375- 390.

Edmonton Journal (2017). “City plans sewer-odour strategy after thousands of complaints.” Online. [<http://edmontonjournal.com/news/local-news/city-plans-sewer-odour-strategy-after-thousands-of-complaints>, Accessed 01-May-2018]

Edwini-Bonsu, S. (2004). “Air flow in sanitary sewer systems: a physically-based approach.” PhD Thesis, University of Alberta, Canada.

Edwini-Bonsu, S., and Steffler, P. M. (2004). “Air flow in sanitary sewer conduits due to wastewater drag: a computational fluid dynamic approach.” *Journal of Environmental Engineering and Science*, 3(5): 331-342.

Edwini-Bonsu, S., and Steffler, P. M. (2006a). “Dynamics of air flow in sewer conduit headspace.” *Journal of Hydraulic Engineering*, 132(8): 791-799. 10.1061/(ASCE)0733-9429.

Edwini-Bonsu, S., and Steffler, P. M. (2006b). “Modeling Ventilation Phenomenon in Sanitary Sewer Systems: A System Theoretic Approach.” *Journal of Hydraulic Engineering*, 132(8): 778-790. 10.1061/(ASCE)0733-9429.

Egorov, Y. (2004). “Contact condensation in stratified stream-water flow.” *Technical Report*, EVOL-ECORA-D 07. <<https://domino.grs.de/ecora/ecora.nsf/>> (Apr. 09, 2016)

Escarameia, M. (2007). “Investigating hydraulic removal of air from water pipelines.” *Water Management*, 160(1): 25-34.

Ferziger, J. H. and Peric, M. (2002). “*Computational Methods for Fluid Dynamics.*” 3rd edition, Springer-Verlag, Berlin.

Fischer, H. B., List, E. J., Koh, R. C. Y., Imberger, J., and Brooks, N. H. (1979). “*Mixing in inland and coastal waters.*” Academic Press, San Diego.

Guo, Q. and Song, C. S. S., (1990). “Surging in urban storm drainage systems.” *Journal of Hydraulic Engineering*, 116 (12), 1523-1537.

Guo, Q. and Song, C. S. S., (1991). “Dropshaft hydrodynamics under transient conditions.” *Journal of Hydraulic Engineering*, 117 (8), 1042-1055.

Guo, S., Qian, Y., Zhu, D., and Edwini-Bonsu, S. (2018). “Effects of Drop Structures and Pump Station on Sewer Air Pressure and Hydrogen Sulfide: Field Investigation.” *Journal of Environmental Engineering*, 144(3): 10.1061/(ASCE)EE.1943-7870.0001336.

Hager, W. H. (1992). “*Energy dissipators and hydraulic jump.*” Kluwer Academic Publishers: Dordrecht.

Hamam, M. A., and McCorquodale, J. A. (1982). “Transient conditions in the transition from gravity to surcharged sewer flow.” *Canadian Journal of Civil Engineering*, 9: 189-196.

Hirt, C. W. and Nichols, B. D. (1981) Volume of fluid (VOF) method for the dynamics of free boundaries. *Journal of Computational Physics*, 39: 201-225

Huang, B. (2017) “Study on Geysers in Urban Drainage Systems.” *PhD Thesis*, Nanjing Hydraulic Research Institute, Nanjing, China.

Kalinske, A. A. and Robertson, J. M. (1943). “Closed conduit flow.” *Transactions, ASCE*, 108, 1435-1447.

LA report (2011). “Waste odor control master plan.” Wastewater Engineering Services Division, Bureau of Sanitation. <
http://www.lacitysan.org/lasewers/sewers/odors/pdf/Odor_Master_Plan_2011.pdf> (Jan. 11, 2016)

Larchar, J. A. (2011). “*Air demand in low-level outlet works.*” MSc Thesis, Utah State University.

Leon, A. S., Ghidaoui, M. S., Schmidt, A. R., and Garcia, M. H. (2006). “Godunov-type solutions for transient flows in sewers.” *Journal of Hydraulic Engineering*, 132(8), 800–813.

Leon, A. S., Ghidaoui, M. S., Schmidt, A. R., and Garcia, M. H. (2009). “Application of Godunov-type schemes to transient mixed flows.” *Journal of Hydraulic Research*, 47(2), 147–156.

Leon, A. S., Ghidaoui, M. S., Schmidt, A. R., and Garcia, M. H. (2010). “A robust two-equation model for transient-mixed flows.” *Journal of Hydraulic Research*, 48(1): 44-56.

Lewis, J. M. (2011). “A physical investigation of air/water interactions leading to geyser events in rapid filling pipelines.” *PhD thesis*, University of Michigan, Ann Arbor, Michigan.

Li, J., and McCorquodale, J. A. (1999). "Modelling mixed flow in storm sewers." *Journal of Hydraulic Engineering*, 125(11): 1170-1180.

Li, L., and Zhu, D. (2018). "Modulation of the transient pressure by air pocket in a horizontal pipe with an end orifice." *Water Science and Technology*, accepted.

Liu, L. (2018). "Experimental Study on Edmonton's Storm Geyser Formation Mechanism and Mitigation Measures." MSc thesis, University of Alberta, Edmonton, Alberta.

Lowe, N. J., Hotchkiss, R. H., and Nelson, E. J. (2011). "Theoretical determination of sequent depths in closed conduits." *Journal of Irrigation and Drainage Engineering*, 137(12): 801-810. 10.1061/(ASCE)IR.1943-4774.0000349.

Lowe, S. (2016). "Sewer ventilation: Factors affecting airflow and modeling approaches." *Journal of Water Management Modeling*, doi: 10.14796/JWMM.C395.

Ma, Y., Zhu, D. Z., and Rajaratnam, N. (2016). "Air entrainment in a tall plunging dropshaft." *Journal of Hydraulic Engineering*, 10.1061/(ASCE)HY.1943-7900.0001181, 04016038.

Malekpour, A., and Karney, B. W. (2016). "Spurious numerical oscillations in the Preissmann Slot Method: Origin and Suppression." *Journal of Hydraulic Engineering*, 142(3): 04015060.

Merzkirch, W. (1987). "*Flow visualization*." 2nd Edition. Academic Press, Orlando.

Mortensen, J. D., Barfuss, S. L., and Jhonson, M. C. (2011). "Scale effects of air entrainment by hydraulic jumps within closed conduits." *Journal of Hydraulic Research*, 49(1), 90-95.

Muller, K. Z., Wang, J., and Vasconcelos, J. G. (2017). "Water displacement in shafts and geysering created by uncontrolled air pocket release." *Journal of Hydraulic Engineering, ASCE*, 143(10): 04017043.

Olson, D., Rajagopalan, S., and Corsi, R. L. (1997). "Ventilation of industrial process drains: Mechanisms and effects on VOC emissions." *Journal of Environmental Engineering*, 123(9): 939-947.

Parker, W. J., and Ryan, H. (2001). "A tracer study of headspace ventilation in a collector sewer." *Journal of the Air & Waste Management Association*, 51(4): 582-592.

Pescod, M. B. and Price, A. C. (1982). "Major factors in sewer ventilation." *Journal of Water Pollution Control Federation*, 54(4), 385-397.

Potter, M. C., Wiggert, D. C., and Ramadan, B. H. (2012). "*Mechanics of Fluids*." 4th edition, Cengage Learning. Stamford, Connecticut.

Qian, Y., Zhu, D. Z., Zhang, W. M., Rajaratnam, N., Edwini-Bonsu, S., and Steffler, P. (2017). "Air movement induced by water flow with a hydraulic jump in changing slope pipes." *Journal of Hydraulic Engineering*, 143(4): 10.1061/(ASCE)HY.1943-7900.0001252, 04016092.

Rajaratnam, N. (1965). "Hydraulic jump in horizontal conduit." *Water Power*, 17: 80-83.

Rajaratnam, N., Mainali, A., and Hsung, C. Y. (1997). "Observations of flow in vertical dropshafts in urban drainage systems." *Journal of Environmental Engineering*, 123(5): 486-491. 10.1061/(ASCE)0733-9372.

Shao, Z. S. (2013). "Two-dimensional hydrodynamic modelling of two-phase flow for understanding geyser phenomena in urban storm water system." *PhD thesis*, University of Kentucky, Lexington, Kentucky.

Song, C. C. S., Cardle, J. A., and Kim Sau, L. (1983). "Transient mixed flow models for storm sewers." *Journal of Hydraulic Engineering*, 109(11), 1487–1504.

Speerli, J., and Hager, W. H. (2000). "Air-water flow in bottom outlets." *Canadian Journal of Civil Engineering*, 27(3): 454-462.

Tullis, B., and Larchar, J. (2011). "Determining air demand for small- to medium-sized embankment dam low-level outlet works." *Journal of Irrigation and Drainage Engineering*, 137(12): 793-800.

U.S. Army Corps of Engineers (US ACE) (1980). "Engineering and design: hydraulic design of reservoir outlet works." *Rep.* EM1110-2-1602. Washington, DC

U.S. Environmental Protection Agency (US EPA) (1985). "Design manual: odor and corrosion control in sanitary sewerage systems and treatment plants." *Rep.* epa/625/1-85/01, Washington, DC.

Vasconcelos, J. G. and Marwell, D. T. B. (2011). "Innovative simulation of unsteady low-pressure flows in water mains." *Journal of Hydraulic Engineering*, 137(11): 1490-1499.

Vasconcelos, J. G., and Wright, S. J. (2005). "Experimental investigation of surges in a stormwater storage tunnel." *Journal of Hydraulic Engineering*, 131(10): 853-861.

Vasconcelos, J. G., and Wright, S. J. (2007). "Comparison between the two-component pressure approach and current transient flow solvers." *Journal of Hydraulic Research*, 45(2): 178-187.

Vasconcelos, J. G., and Wright, S. J. (2009). "Investigation of rapid filling of poorly ventilated stormwater storage tunnels." *Journal of Hydraulic Research*, 47(5): 547-558.

Vasconcelos, J. G., and Wright, S. J. (2011). "Geysering generated by large air pockets released through water-filled ventilation shafts." *Journal of Hydraulic Engineering*, 137(5): 543-555.

Vasconcelos, J. G., Klaver, P. R., and Lautenbach, D. J. (2015), "Flow regime transition simulation incorporating entrapped air pocket effects." *Urban Water Journal*, 12(6): 488-501.

Vasconcelos, J. G., Wright, S. J., and Roe, P. L. (2006). "Improved simulation of flow regime transition in sewers: two-component pressure approach." *Journal of Hydraulic Engineering*, 132(6): 553-562.

Vasconcelos, J. G., Wright, S. J., and Roe, P. L. (2009). "Numerical oscillations in pipe-filling bore predictions by shock-capturing models." *Journal of Hydraulic Engineering*, 135(4): 296-305.

Volkart, P. U., and Speerli, J. (1994). "Prototype investigation of the high velocity flow in the high head tunnel outlet of the Panix Dam." Proc. 18th ICOLD Congress, Durban, South Africa, Q. 71, R. 6, 55-78.

Wang, Y. C., Nobi, N., Nguyen, T., and Vorreiter, L. (2012). "A dynamic ventilation model for gravity sewer networks." *Water Science and Technology*, 65(1): 60-68.

Ward, M., Corsi, R., Morton, R., Knapp, T., Apgar, D., Quigley, C., Easter, C., Witherspoon, J., Pramanic, A., and Parker, W. (2011). "Characterization of natural ventilation in wastewater collection systems." *Water Environment Research*, 83(3): 265-273.

Ward, M., Hamer, G., McDonald, A., Witherspoon, J., Loh, E., and Parker, W. (2011). "A sewer ventilation model applying conservation of momentum." *Water Science and Technology*, 64(6): 1374-1382.

Wiggert, D. C. (1972). "Transient flow in free-surface, pressurized systems." *Journal of the Hydraulics Division*, 98(1): 11-27.

Wright, N. W. (2013). "Air vent sizing in low-level outlet works for small to medium-sized dams." MSc Thesis, Utah State University. Logan, Utah.

Wright, N. W., and Tullis, B. P. (2014). "Prototype and laboratory low-level outlet air demand comparison for small to medium-sized embankment dams." *Journal of Irrigation and Drainage Engineering*, 140(6): 04014013.

Wright, S. J., Lewis, J. W., and Vasconcelos, J. G. (2011). "Physical processes resulting in geysers in rapidly filling storm-water tunnels." *Journal of Irrigation and Drainage Engineering*, 137(3): 192-202.

Wright, S. J., Lewis, J. W., and Vasconcelos, J. G. (2011a). "Geysering in rapidly filling storm-water tunnels." *Journal of Hydraulic Engineering*, 137(1): 112-115.

Wright, S. J., Lewis, J. W., and Vasconcelos, J. G. (2011b). "Physical processes resulting in geysers in rapidly filling storm-water tunnels." *Journal of Irrigation and Drainage Engineering*, 137(3): 192-202.

Wright, S. J., Vasconcelos, J. G., Creech, C. T., and Lewis, J. W. (2008). "Flow regime transition mechanisms in rapidly filling stormwater storage tunnels." *Environmental Fluid Mechanics*, 8(5): 605-616.

Wright, S. J., Vasconcelos, J. G., Lewis, J. W., and Creech, C. T. (2009). "Flow regime transition and air entrapment in combined sewer storage tunnels." *Journal of Water Management Modeling*, R235-15: 237-256.

Youtube (2013). "Exploding Storm Sewer Lifts Car in Montreal" Online. [https://www.youtube.com/watch?v=a1VulahjR68&t=8s, Accessed 20-Apr.-2018]

Youtube (2016). "Edmonton's Old Faithful." Online. [https://www.youtube.com/watch?v=pvGfmwYvXtg, Accessed 25-Feb.-2018]

Zhang, W. M., Liu, M. N., Zhu, D. Z., and Rajaratnam, N. (2014). "Mean and turbulent bubble velocities in free hydraulic jumps for small to intermediate Froude numbers." *Journal of Hydraulic Engineering*, 140(11): 04014055. 10.1061/(ASCE)HY.1943-7900.0000924.

Zhang, W. M., Zhu, D. Z., Rajaratnam, N., Edwini-Bonsu, S., Fiala, J., and Pelz, W. (2016). "Use of air circulation pipes in deep dropshafts for reducing air induction into sanitary sewers." *Journal of Environmental Engineering*, 142(4): 04015092. 10.1061/(ASCE)EE.1943-7870.0001046.

Zhou, F. (2000). "Effects of trapped air on flow transients in rapidly filling sewers." *PhD thesis*, University of Alberta, Edmonton, Alberta.

Zhou, F., Hicks, F. E., and Steffler, P. (2004). "Analysis of effects of air pocket on hydraulic failure of urban drainage infrastructure." *Canadian Journal of Civil Engineering*, 31: 86-94.

Zhou, F., Hicks, F. E., and Steffler, P. M. (2002). "Transient flow in a rapidly filling horizontal pipe containing trapped air." *Journal of Hydraulic Engineering*, 128(6): 625-634.

Zhou, L., Liu, D., and Ou, C. (2011). "Simulation of flow transients in a water filling pipe containing entrapped air pocket with VOF model." *Engineering Applications of Computational Fluid Mechanics*, 5(1): 127-140.